

AD No. ~~36477~~
ASTIA FILE COPY

NEVIS CYCLOTRON LABORATORIES



COLUMBIA UNIVERSITY
PHYSICS DEPARTMENT
Irvington-on-Hudson,
New York

Joint ONR - AEC Program
Office of Naval Research Contract
Contract NS-ori-110 Task No. 1

THIS REPORT HAS BEEN DELIMITED
AND CLEARED FOR PUBLIC RELEASE
UNDER DOD DIRECTIVE 5200.20 AND
NO RESTRICTIONS ARE IMPOSED UPON
ITS USE AND DISCLOSURE.

DISTRIBUTION STATEMENT A

APPROVED FOR PUBLIC RELEASE,
DISTRIBUTION UNLIMITED.

Nevis Cyclotron Laboratories
Columbia University
Physics Department
Irvington-on-Hudson,
New York

THE ELASTIC SCATTERING OF
PIONS ON ALUMINUM

Aihud Pevsner

CU-67-54-ONR-110-1-Physics

Submitted in partial fulfillment
of the requirements for the degree
of Doctor of Philosophy in the
Faculty of Pure Science, Columbia
University

June, 1954

Joint ONR-AEC Program
Office of Naval Research Contract
Contract N6-ori-110-Task No.1

TABLE OF CONTENTS

Part 1

	<u>Page</u>
I. Introduction	1
II. Plan of the Experiment	
A. General	4
B. Focussing Magnet	8
C. Scintillation Detectors	8
D. Scattering Stand	9
E. Electronics	10
III. Experimental Procedure	
A. Analysis of the Beam	16
B. Stability and Efficiency Check	22
C. Spurious Counts	27
D. Criterion for Elastic Scattering	29
E. Additional Checks	32
IV. Results	
A. Calculation of Cross-sections	34
B. Corrections	39
V. Discussion of Experimental Results	
A. Optical Model	46
B. Comparison Experimental and Calculated Curves	53
C. Calculation of Potential from Pion-nucleon Scattering	57
D. Mean Free Path in Nuclear Matter	61

Part 2

I. Introduction	66
II. Optical Model	
A. Definition	69
B. Phase Shift Analysis	71
C. Discussion	73
III. Born Approximation	107
Appendix	110
Footnotes	116
Acknowledgements	117

FIGURES

FIGURE	<u>Page</u>
1. Floor plan of cyclotron, shielding, focussing magnet, and counter telescope arrangement.	5
2. View of scattering apparatus stand.	7
3. Block diagram of circuits.	11
4. Fast 6BN6 coincidence circuit.	12
5. Bridge coincidence circuit.	13
6. Discriminator and pulse shaper.	15
7. π^- -beam range curve.	17
8. π^+ -beam range curve.	18
9. Positive beam differential range curve.	19
10. "Corrected" π^- integral and differential range curves, linear plot.	23
11. "Corrected" π^+ integral and differential range curve.	24
12. Integral and differential range curve scattered at 35° by $1/2$ inch aluminum.	25
13. Integral and differential range curve scattered at 160° by $1/2$ inch aluminum.	26
14. Negative meson beam spread curve with and without $1/4$ inch aluminum target. Taken with Counter 4, 30 inches from target.	33
15. Negative meson beam spread with $1/2$ inch target. Crystal 4 30 inches from target.	35
16. Experimental cross section for $1/2$ inch aluminum target.	37

FIGURES (Continued)

<u>Figure</u>		<u>Page</u>
17.	Experimental cross section curve for 1/4 inch aluminum target. The theoretical (phase shift analysis) curves for (V_1, V_2) Mev = $(-30, -22)$, $(-40, -15)$ for π^- , and $(-20, -10)$, $(-20, -25)$ and $(-30, -15)$ for π^+ are shown for comparison.	41
18.	Illustration of effect of resolution for hypothetical curve shape.	45
19.	Illustration of relations for Born Approximation discussion. (See text for details).	51
20.	Calculated V_1 from published phase shift analysis of $\pi + p$ interactions.	59
21.	Comparison of predicted values of absorption cross section vs. mean free path from phase shift calculations.	63
22.	Differential cross section for 79 Mev π^+ mesons on aluminum calculated using phase shift analysis on optical model for the nucleus, for $V_1 = -20$ Mev, $V_2 = -10, -25, -35$ Mev.	93
23.	Same as above. π^+ mesons $V_1 = -30$ Mev, $V_2 = -15, -22, -30$ Mev.	94
24.	Same as above. π^+ mesons $V_1 = -40$ Mev, $V_2 = -15, -30$ Mev.	95
25.	Differential cross sections for Born approximation #1 (described in text, p. 107). π^+ and π^- curves for $V_1 = -30$ Mev, $V_2 = -30$ Mev.	96

FIGURES (Continued)

Figure		Page
26.	Differential cross sections for Born approximations #2, 3, 4, and 5 (described in text, pp. 107-108). mesons. $V_1 = -30$, $V_2 = -30$ Mev.	97
27.	Same as Figure 21. π^- mesons. $V_1 = -20$ Mev. $V_2 = -10, -25, -35$ Mev.	98
28.	Same as Figure 22. π^- mesons. $V_1 = -30$ Mev. $V_2 = -22, -30$ Mev.	99
29.	Same as Figure 23. π^- mesons. $V_1 = -40$ Mev. $V_2 = -15, -30$ Mev.	100
30.	Same as Figure 25. π^- mesons. $V_1 = -30$ Mev. $V_2 = -30$ Mev.	101
31.	Plot of $p + iq$ from phase shift analysis where $\frac{dg}{d\Omega} = b^2$ $p + iq = 2ik_0 f$ π^- mesons: 10 degrees to 75 degrees. Plotted for $V_1 -20$ Mev, $V_2 -1, -5, -10, -25, -35$ Mev.	102
32.	Same for π^+ mesons.	103
33.	Same for π^- mesons, 60 degrees to 150 degrees.	104
34.	Same for π^+ mesons, 60 degrees to 150 degrees.	105
35.	Plot of $p + iq$, π^- mesons, $V_1 = +20, 0, -10, -20$ Mev. $V_2 = -10$ Mev and also $V_1 = -30$ Mev, $V_2 = -15$ Mev.	106

v TABLES

Table	Page
1. Quadruple coincidence counting rates, as function of angle, for 1/2 inch aluminum target with 3/4 inch and 1-1/2 inch copper absorber between X3 and X4. Also target out rate with 1 inch copper absorber.	30
2. Experimentally measured differential cross sections. π^- and π^+ mesons, 1/2 inch aluminum target.	38
3. Experimentally measured differential cross sections. π^- and π^+ mesons, 1/4 aluminum target. Theoretical curves from phase shift analysis plotted for comparison.	40
4. List of cases computed in phase shift analysis, V_1 , V_2 , k_1 , k_2 and λ , the mean free path, for each case.	48
5. Calculated absorption cross sections (total cross section minus coherent scattering cross section) for each l value. Also listed is the absorption cross section calculated using the method of Fernbach, Serber, and Taylor (F. S. T.) and the F. S. T. value modified by $(k_1/k_0)^{1.5}$ π^- mesons.	75
6. Same as Table 5, but for π^+ mesons.	76
7. List of Coulomb amplitude functions K and L for selected angles where	
$\begin{aligned} 2k_0 f_c &= K + iL \quad (\pi^-) \\ &\quad -K + iL \quad (\pi^+) \end{aligned}$	78
8. Tabulation of M and N for π^- case.	
$2k_0 f = K + iL + \sum_l (N - iM)(2l + 1) P_l(\cos \theta)$	79
9. Same as Table 8, but for π^+ mesons.	

TABLES (Continued)

Table	<u>Page</u>
10. Calculated differential scattering cross section from phase shift analysis for all 16 π^- cases.	81-82
11. Same as Table 10, but for π^+ cases.	83-84
12. List of p and q for π^- cases. $2ik_0 f(\theta) = p(\theta) + iq(\theta)$	85-88
13. Same as Table 12, but for π^+ cases.	89-92
14. Comparison of notation in references 22 and 23.	113
15. Comparison of coherent scattering amplitude for meson nucleon reaction as function of energy and angle against forward scattering amplitude at 80 Mev. (Elastic interaction only).	115

THE ELASTIC SCATTERING OF POSITIVE AND NEGATIVE PIONS BY NUCLEI

I: Introduction:

An investigation of the elastic scattering of positive and negative pions by various nuclei is now in progress. The elastic scattering of 60 Mev positive and negative pions has been previously investigated by Byfield et al.,¹ using carbon plates in an expansion cloud chamber placed in the Nevis 60 Mev meson beams. An analysis of the difference of the positive and negative pion elastic scattering using a modified optical model and taking into account the interference of the Coulomb potential with the nuclear potential in a Born approximation led to the conclusion that the nuclear potential experienced by the incident meson was most likely attractive.

An independent analysis by Peaslee² which essentially represented an addition of the individual nucleon scattering contributions came to the same conclusion and therefore implied that the sign of the p wave phase shift (which seems to be mostly responsible for the low energy meson scattering phenomena) was positive.

A later cloud chamber investigation of the elastic scattering of 125 Mev negative pions by carbon and lead performed by Kessler and Lederman³ was also consistent with an optical model analysis using an attractive nuclear potential. However, the lack of corresponding positive pion data did not

allow as sensitive a determination of the sign of the potential.

Similar cloud chamber experiments for negative mesons on carbon were carried out by Shapiro⁴ and analyzed by Bethe and Wilson.⁵ Tracy,⁶ with poor statistics has measured the elastic scattering of π^+ - mesons on aluminum by using a cloud chamber while Shutt et al,⁷ using a diffusion chamber, have measured the scattering of pions on helium.

Isaacs et al⁸ also investigated the elastic scattering of 60 Mev negative pions from carbon using scintillation counter techniques and obtained much better statistics. The data was also consistent with a negative well but here again due to the lack of positive data the determination of the sign of the potential was not very sensitive.

Following this early work a systematic survey of the elastic scattering of both positive and negative pions of various energies for various elements (both heavier and lighter than carbon) was undertaken at Nevis. Scintillation counter techniques were employed and make possible angular resolutions and statistical accuracies far superior to those obtained in the cloud chamber experiments. This paper reports on the initial result in this program for 80 Mev π^+ and π^- mesons on aluminum.

The purpose of these experiments was:

- (1) To investigate, with improved statistical accuracy and angular resolution, the angular distribution of π mesons

from nuclei as an important phenomenon in high energy physics. In particular, it is of interest to investigate as carefully as possible the differences between π^+ and π^- scattering in nuclei with roughly equal numbers of neutrons and protons to observe interference effects between "meson forces" and "electromagnetic forces" in the scattering.

(2) There is some interest in seeing how well the scattering can be matched by an "optical model", where the effect of nuclear interactions is represented by a complex potential inside the nucleus. Of most interest is the question of the possibility of using a constant complex potential inside the nucleus and a coulomb field outside. The imaginary part of the potential attenuates the wave to take into account absorption, inelastic, and other possible incoherent processes, and can be alternately expressed in terms of a mean free path in nuclear matter for such processes.

(3) To compare π meson angular scattering with that of other probe particles, such as electrons, neutrons, and protons, to give information on the distribution of nuclear matter as a function of distance from the center of the nucleus.

It is to be expected that such scattering will be of continuing interest to physics and that the accuracy of such measurements will be steadily improved to allow comparison with more refined theoretical analysis.

(4) It is of interest to see if the scattering can be explained in terms of the known results for the scattering by

single nucleons with the application of the charge independence hypothesis. This need not apply, since the properties of nuclear matter may not be able to be represented in terms of individual processes between pairs of particles alone.

PLAN OF THE EXPERIMENT

II.

A. General

The Nevis 385 Mev proton cyclotron produces a beam of circulating protons. When a beryllium target is inserted inside the cyclotron, protons striking the target induce nuclear reactions which emit, among other products of reaction, negative and positive mesons of varying momenta. These charged particles are analyzed and focussed by the fringing field of the cyclotron magnet into beams of equal momentum particles. Thus with the cyclotron magnetic field in a given direction, particles of one sign (say negative mesons) emerge in the direction of the experimental area. Channels are cut in the cyclotron shielding wall (8' of lead and iron) to allow the mesons to enter the experimental area (see Figure 1.) To obtain the opposite sign meson particle the magnetic field of the cyclotron is reversed. Then positive mesons of the same momenta as the negative ones will be focussed through the same channel in the identical manner. Mesons of 180 Mev/c mean momentum emerged from the channel chosen in this experiment. This channel was chosen as it corresponded to the highest energy channel from which both positive and negative

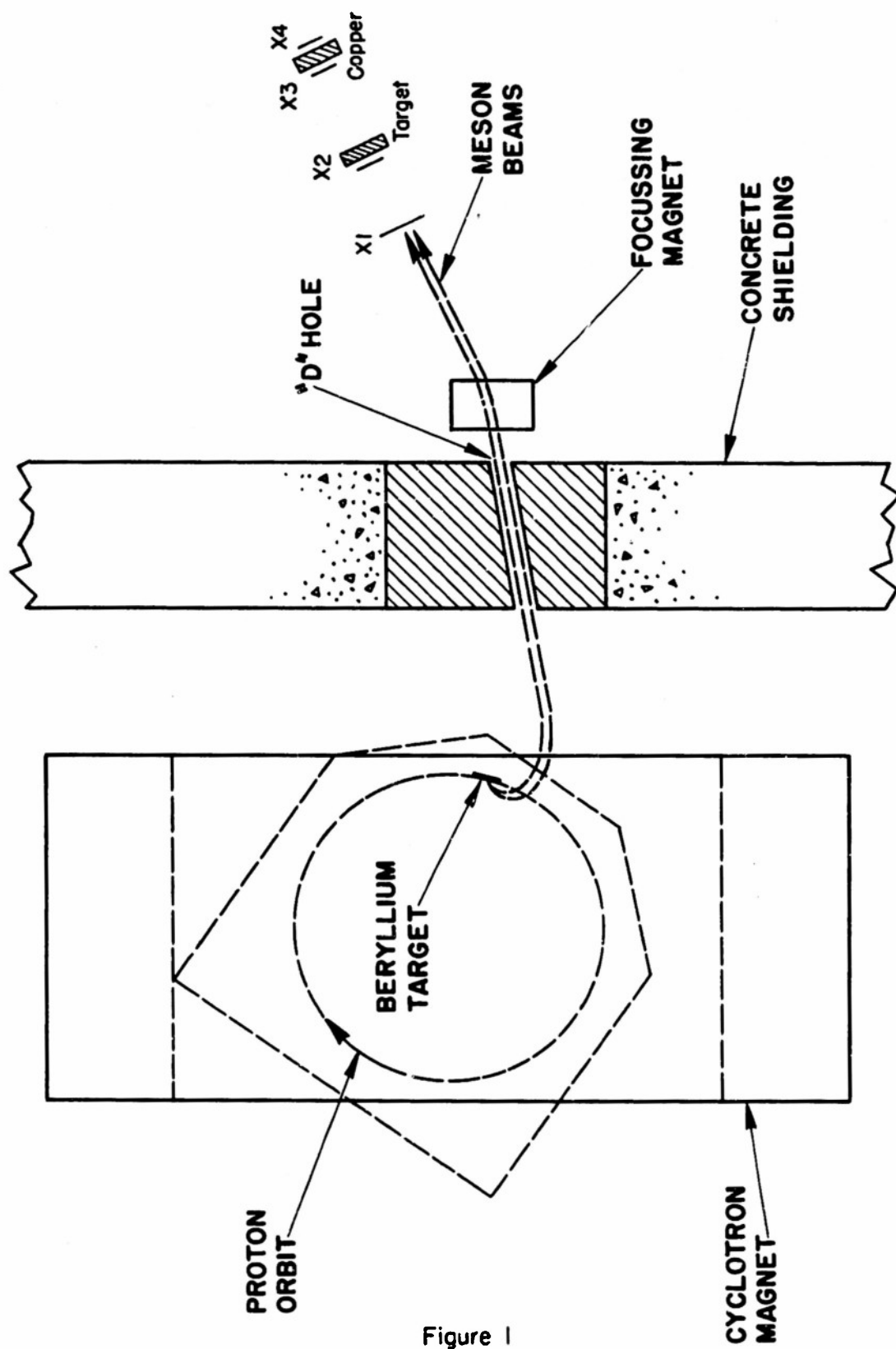


Figure 1

mesons were available with good intensities.

Upon emerging from the shielding wall the meson beam was deflected and focussed by an instrument magnet. The beam was then defined by a scintillation counter telescope consisting of two scintillation detectors, about three feet apart, connected to a coincidence circuit that effectively recorded the number of particles passing through both of the detectors. Following this telescope and in line with it, the target to be studied, $1/2$ " or $1/4$ " thick aluminum 5" by 3" in size, was mounted on a turret stand. Most of the incident beam striking the target passed through, but a small percentage interacted in the aluminum target. Part of the interaction was elastic and yielded elastically scattered particles into all angles from 0 to 180 degrees with the incident beam direction. To detect these elastically scattered particles two more scintillation detectors were mounted on the arms of a rotatable scattering turret (Figure 2) that allowed the detectors to be rotated in a vertical plane, to any angle with the incident beam. By placing the coincidence output of these last two detectors in coincidence with the output of the monitoring telescope it was possible to measure the number of beam particles scattered at a given angle. Sufficient absorber was placed between the last two detectors so as to allow the elastically scattered particles to be predominantly detected and to absorb any secondary protons or inelastically scattered mesons.

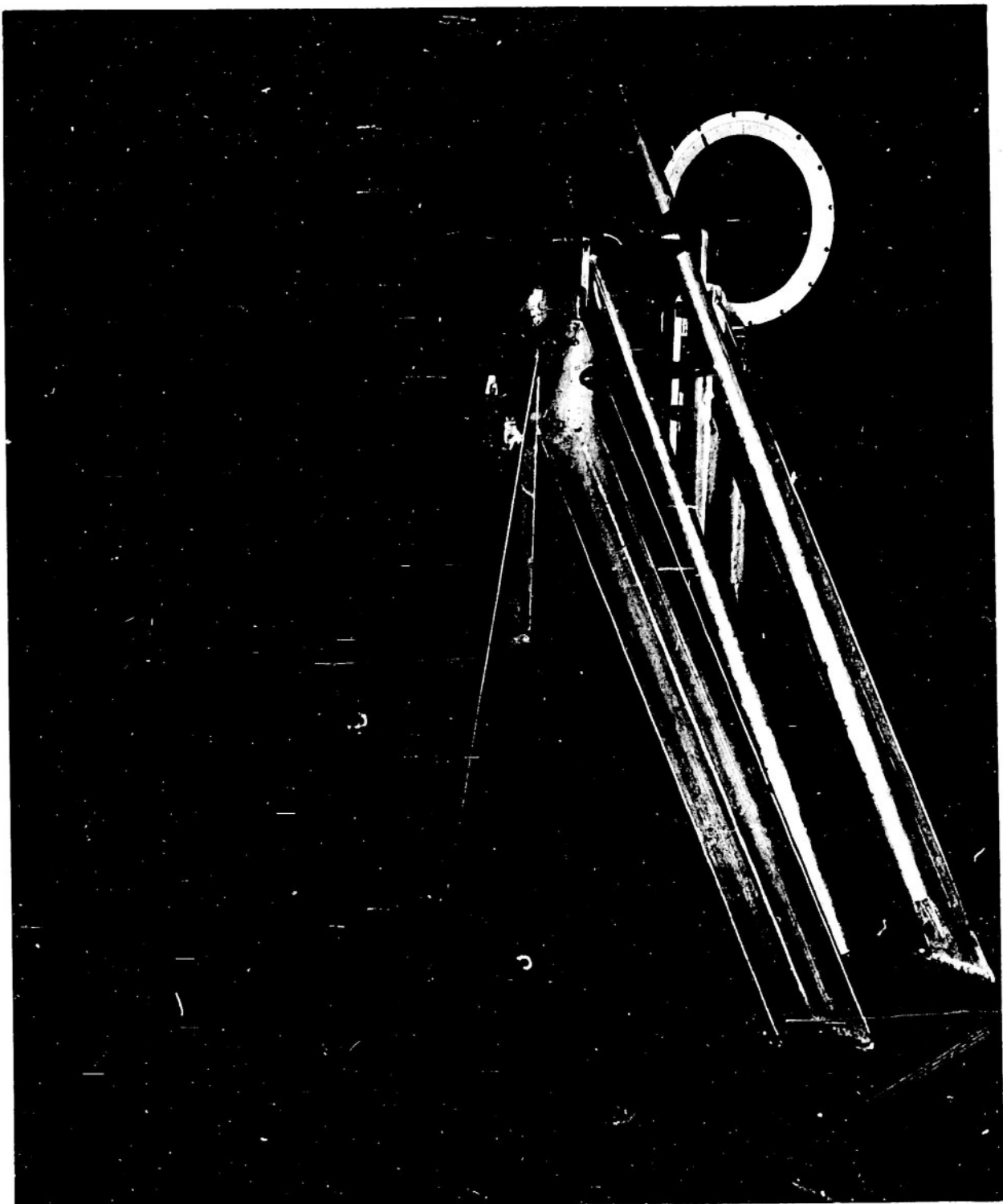


FIGURE 2.

B. Focussing Magnet

The focussing magnet served several purposes. As a bending magnet it supplemented the momentum selection of the cyclotron fringing field. It also deflected the beam out of line with the channel opening. The opening views the interior of the cyclotron enclosure, and a rather high background is present along the line of the main channel opening. This background consists of gamma rays, neutrons, and some charged secondary particles which are mainly not deflected the same as the meson beam. Triangular shaped pole pieces were chosen to obtain an increase in intensity through focussing. The magnet acted as a converging lens in the vertical direction, and as a defocussing lens in the horizontal direction. A net gain of intensity of a factor of three was obtained through the monitoring telescope. Raising or lowering a 1/2" crystal at the focal point by 7/8" reduced the intensity by nearly a factor of three. A further gain was then realized by using rectangularly shaped counters, similar to the shape of the source, with the smaller dimension vertical. The scattering was measured through angles in a vertical plane.

C. Scintillation Detectors

Stilbene crystals were used as the scintillators with a decay time of less than 8×10^{-9} seconds. The first crystal of the telescope, X1, was 4" x 2" x 1/8"; the second, X2, was 4" x 1/2" x 1/8" in the first runs and was later changed to 3" x 3/4" x 3/16". The crystals mounted on the rotating

arm were both $4'' \times 2''$; the nearer, X3, being $1/8''$ thick, and the last, X4, being $1/4''$ thick.

For maximum efficiency in counting particles scattered at a given angle, an annular counter, subtending an angle θ to $\theta + \Delta\theta$ with the incident beam, would be required. So as not to exceed a given angular resolution, the last counter must subtend an angle no larger than $\Delta\theta$. However, the angle θ may be as large as 2π , as is the case with an annular counter. Hence, we chose one dimension of the counter by requiring a certain $\Delta\theta$ and then made the other dimension as large as possible, consistent with an approximation to an annulus.

All the crystals were mounted in aluminum frames for support with aluminum foil, a few mils thick, being used as a reflector. Two RCA 1P21 photomultiplier tubes were mounted at each end of the holder looking in at the crystals. The outputs of the 1P21 phototubes were connected in parallel. The voltages supplied to the 1P21's were adjusted with a potentiometer so that pulses of equal height could be obtained from a particle at either end of the crystal. To insure detection of all minimum ionization particles, all counters were operated in the plateau region (1400-1700 volts on the photomultiplier).

D. Scattering Stand

A picture of the stand is shown in Figure 2. The target was mounted between two screws (fitting into recesses in the side of the target) in the center of the stand at beam height above the floor. On each side of the screws holding the

target was an aluminum holder rotatable through 360 degrees. Attached to one was a long pointer that swung about a large protractor one foot in diameter. Long rods fit into the aluminum holders. X3 and X4 were rigidly mounted and centered on these long rods. The rod could be pushed through the holders and then fixed in place with set screws. Thus X3 and X4 could very conveniently be moved to any desired distance from the target. The angle of the crystal with the beam direction could be conveniently changed by rotating the holders, rods, and crystals all together, and fixing the holders in place with lock nuts.

E. Electronic Arrangement

Figure 3 shows a block diagram of the electronic arrangement used. Each pulse from the scintillation counters was amplified and limited in a distributed amplifier of rise time .0026 micro-seconds, and a gain of 10. This was then fed to a fast double coincidence circuit. Both 6BN6 and bridge circuits (Figures 4 and 5) were used interchangeably. With the 6BN6 circuit resolutions better than four millimicroseconds were obtained and used in some runs. However, for most of the work resolutions about 1.5×10^{-8} seconds were found sufficient for the "fast" coincidence circuits.

Fast double coincidences between Crystals 1 and 2, 1 and 3, and 2 and 4 were made to give optimum overall time resolution of the selected total events. The outputs of the coincidence circuits were fed into cathode followers that drove 125 ohm

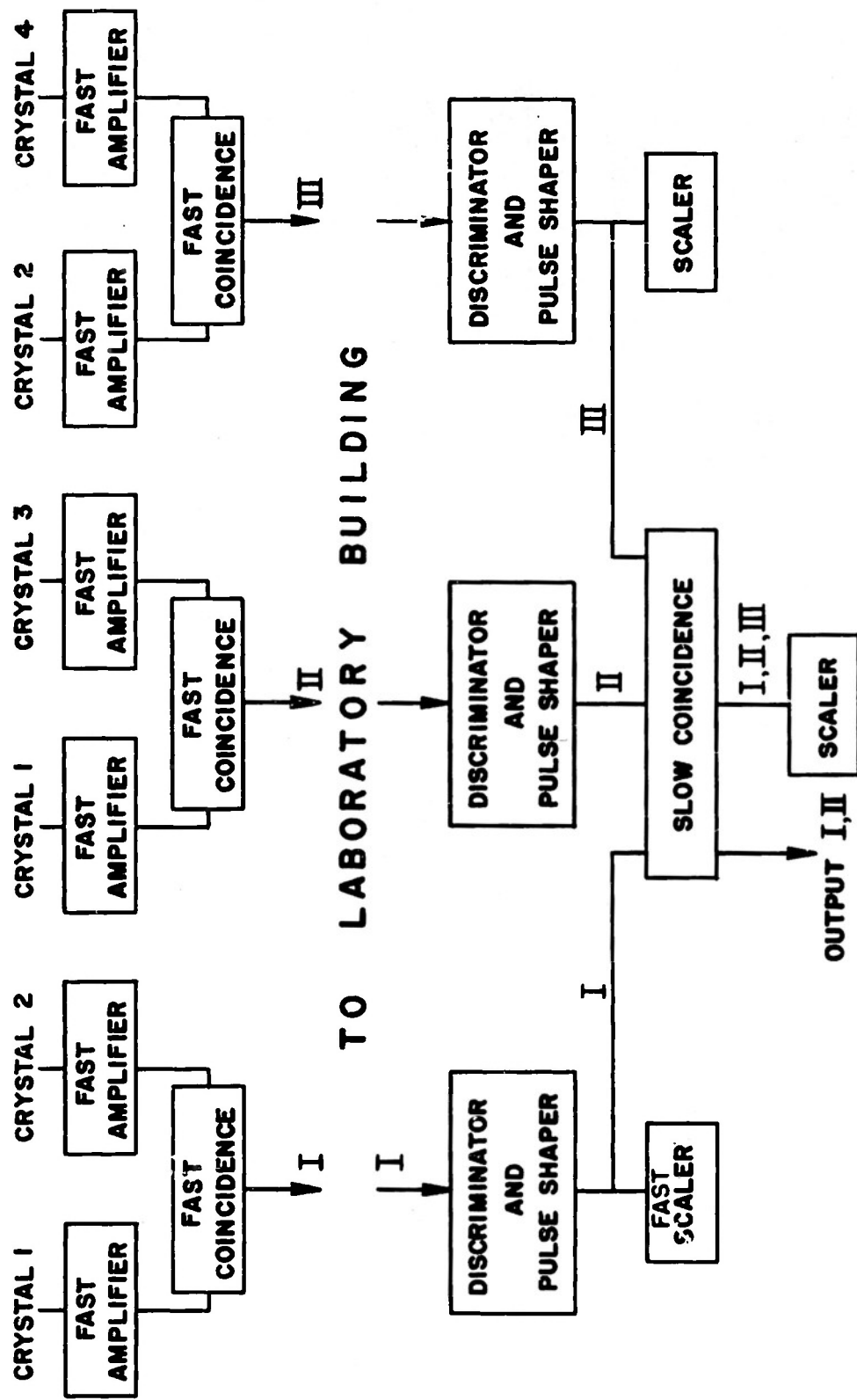
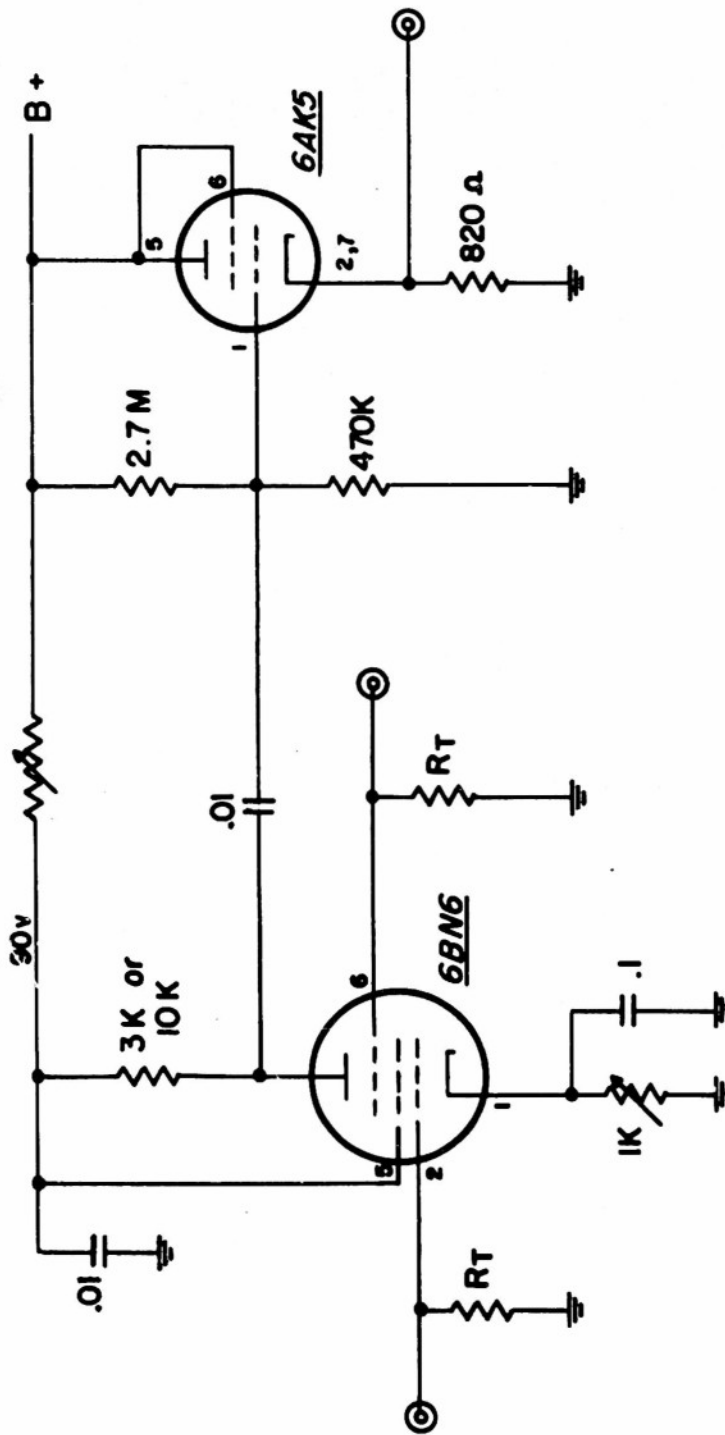
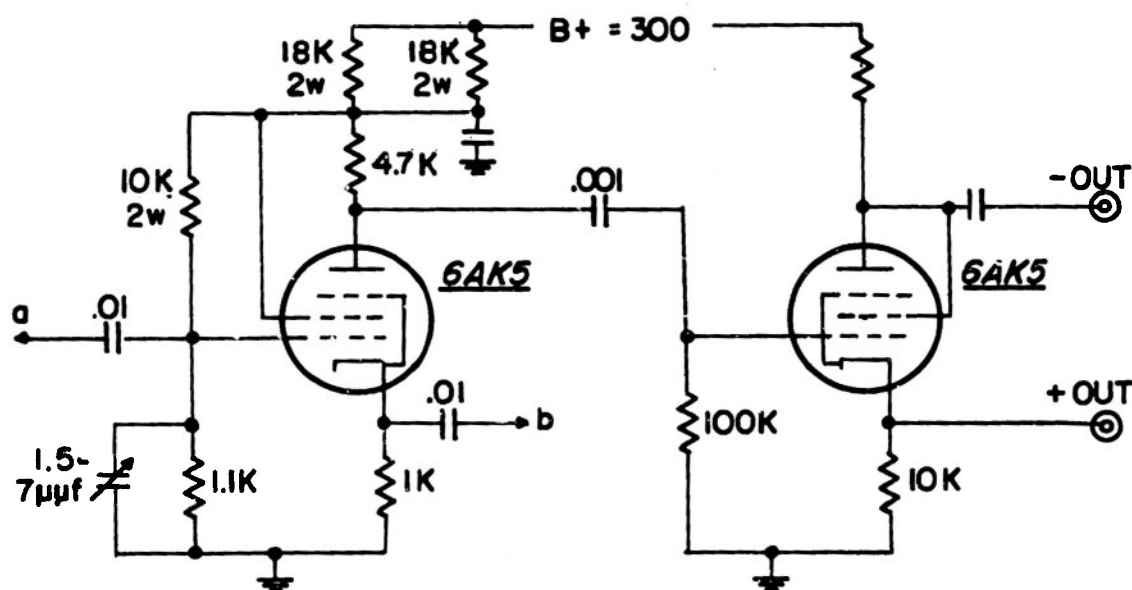
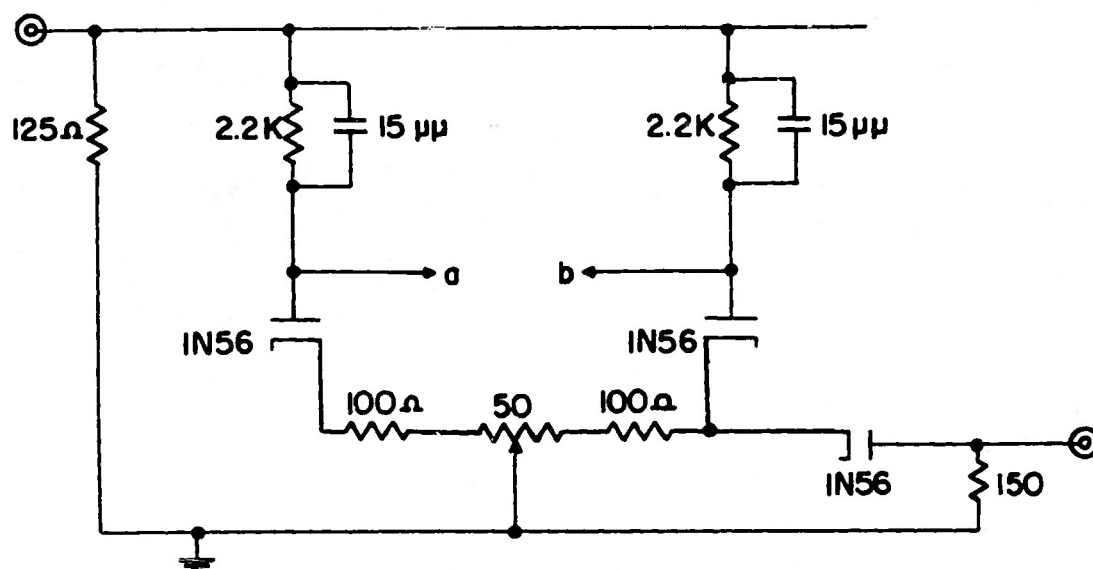


Figure 3



FAST COINCIDENCE CIRCUIT

Figure 4



BRIDGE COINCIDENCE CIRCUIT

Figure 5

RG63U cable that carried the double coincidence pulses up from the cyclotron building (300 feet) to the laboratory building. Here they were further amplified and fed to fast discriminator and pulse shaping circuits (Figure 6). The fast double coincidence circuits in the cyclotron building are subject to feed-through. That is, a single very large pulse, perhaps due to a nuclear explosion in the crystal, may give an output from the double coincidence circuit. It is possible, however, to differentiate this from a true double pulse since in our coincidence circuits the pulse height from double was three to ten times that of any single pulse input. The discriminator circuit (Figure 6) was easily capable of this discrimination. The LFP60 univibrator in the output of the discriminator supplied uniform output pulses 8 volts in height and 0.1μ sec. wide. The fast double coincident counts between X1 and X2 were used as a monitor for the experiment. This fast coincidence output, after passing through the discriminator and pulse shaper, was sent to a fast 0.1μ s decade scalar, and also to a slower coincidence circuit to be combined with the other fast double coincidences in a Rossi type (0.1μ sec.) "slow" triple coincidence circuit. The output of this circuit consisted of over-all quadruple coincidences in our four crystals. Switches in the Rossi circuit allowed us to look at the individual rates from any one, or the coincidence of any two of the individual double coincidence circuits so that we could check for internal consistency of our results and "trouble shoot" more easily.

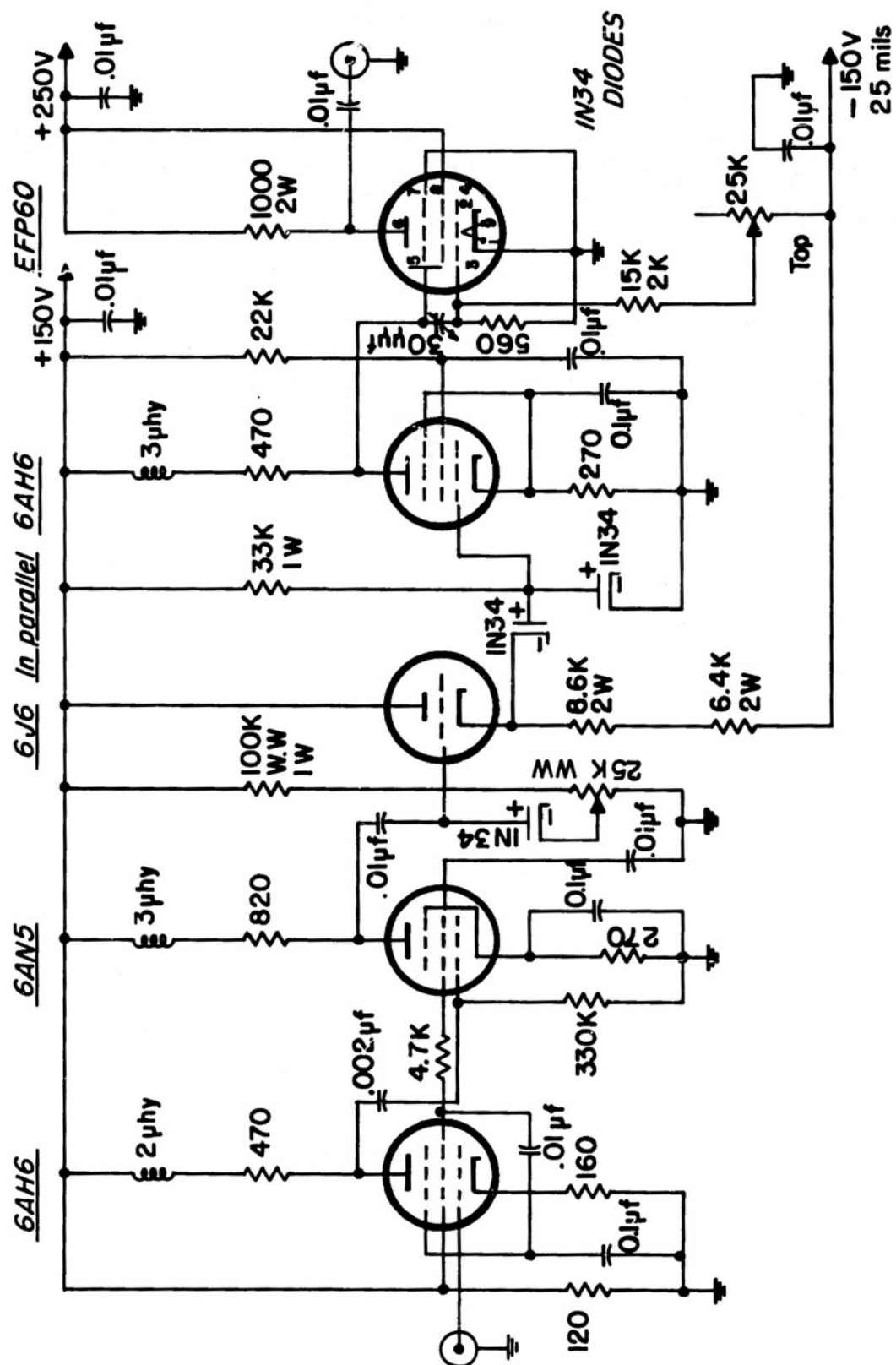


Figure 6

III. EXPERIMENTAL PROCEDURE

A. Analysis of the Beam

Range curves were taken to estimate the percentage of π mesons in the beam through the 1-2 telescope. These range curves were taken as integral curves, that is, the number of four-fold coincidences for a fixed number of 1-2 coincidences was recorded as a function of the total absorber thickness in front of crystal number 4. Typical range curves are shown in Figure 7 for π^- mesons, and in Figure 8 for π^+ mesons. All the points were taken for the same number of monitor counts. The statistical error in the point for 0" absorber is of the order of 1 percent.

For purposes of analysis, the results were plotted as a differential curve showing the relative number of mesons stopping in each interval of absorber. The differential curve corresponding to Figure 8 is shown in Figure 9. The roughly flat section of the differential curve from 0" copper absorber to 1" copper absorber corresponds mainly to the π mesons which were lost as a result of nuclear absorption of the mesons in the copper. The rise in Figure 9 after 1" thickness of copper corresponds to the loss of those mesons that were slowed down due to ionization loss, and came to the end of their range in the copper. Thus, most of the mesons have a range of about 1.25" equivalent of copper, after leaving counter 2, with a $KE = 80.4 \text{ Mev}^9$ and a momentum of 170 Mev/c. This range curve was taken for the run with a 1/4" aluminum target and positive mesons. The value of the

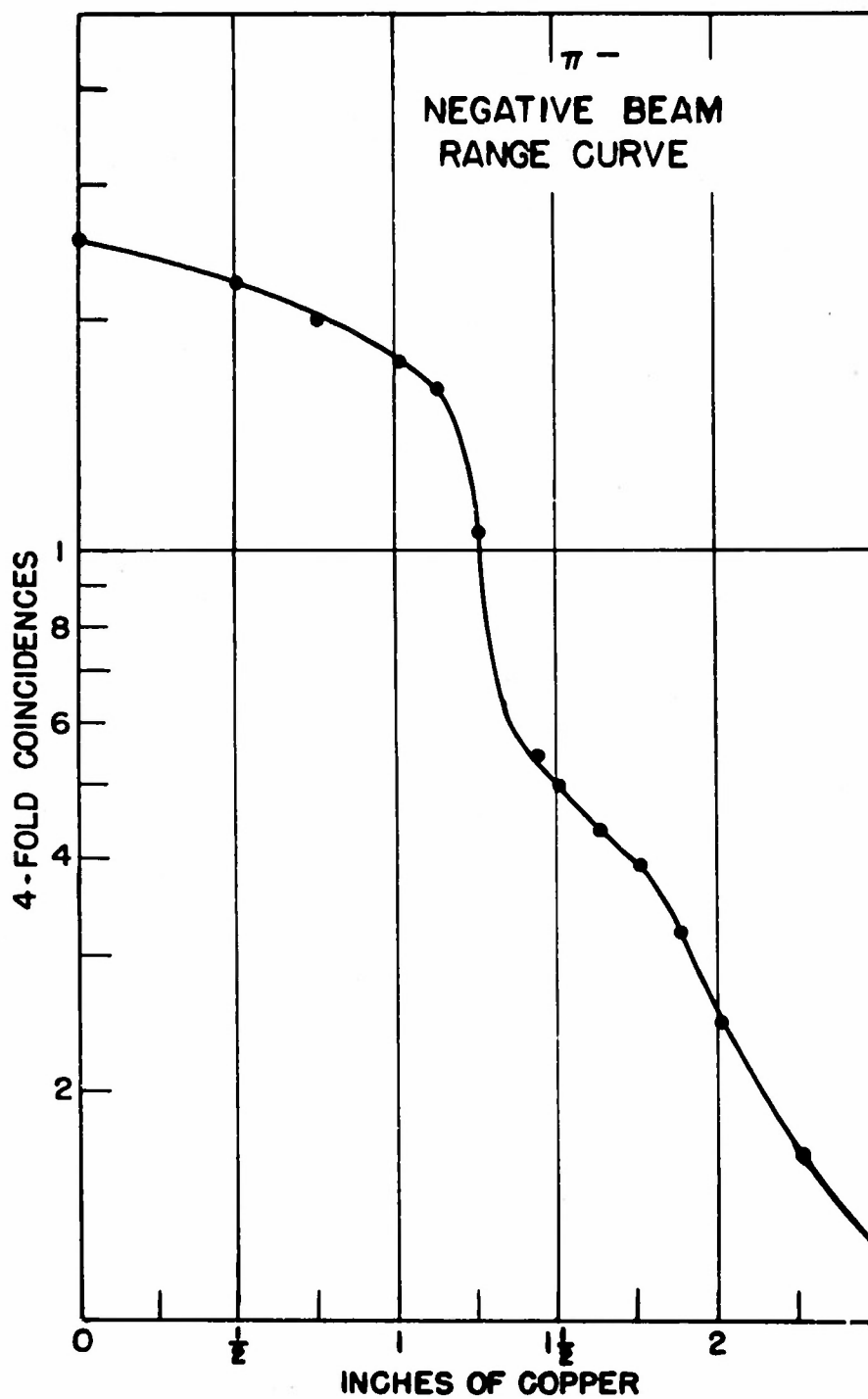


Figure 7

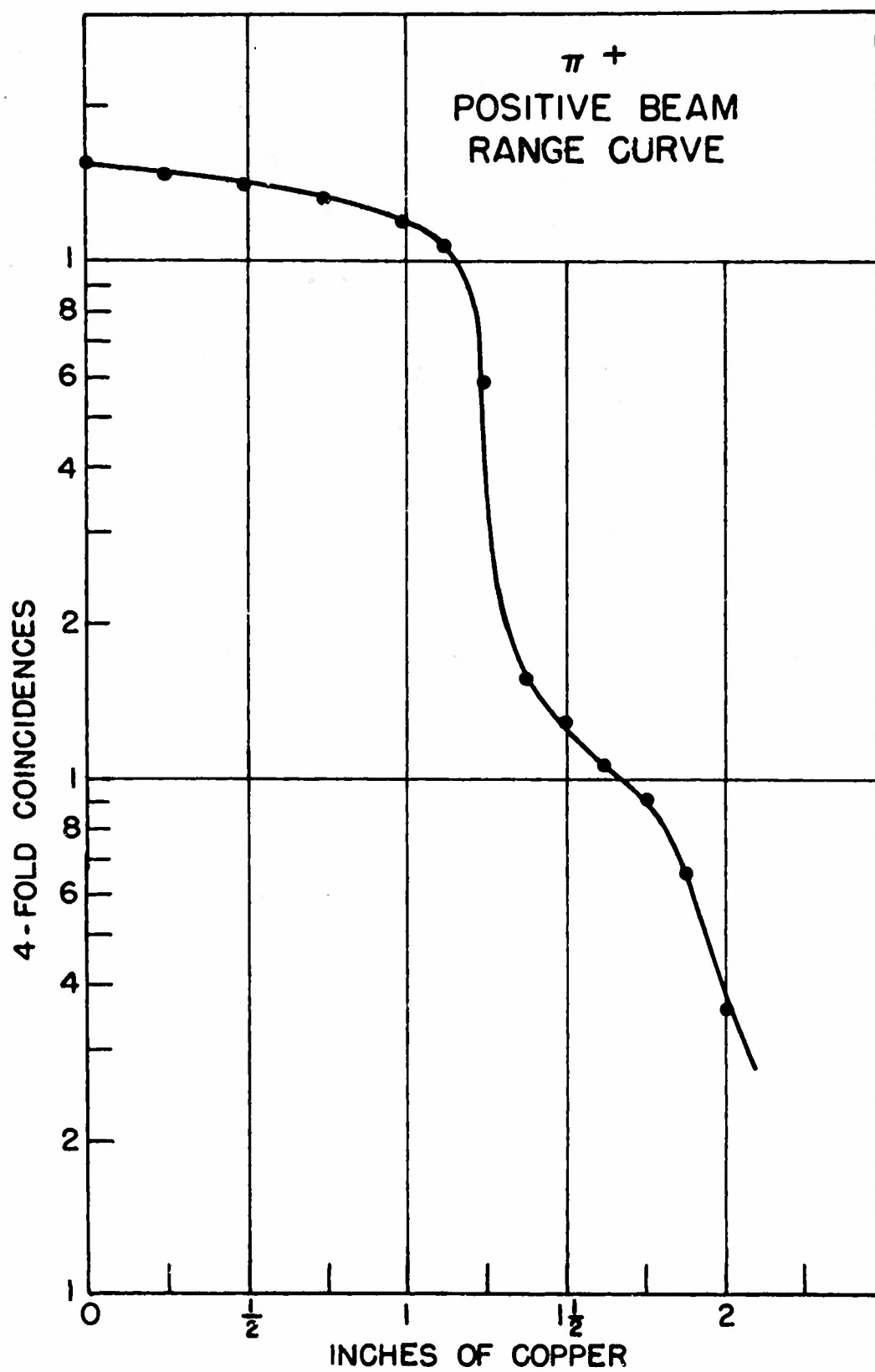


Figure 8

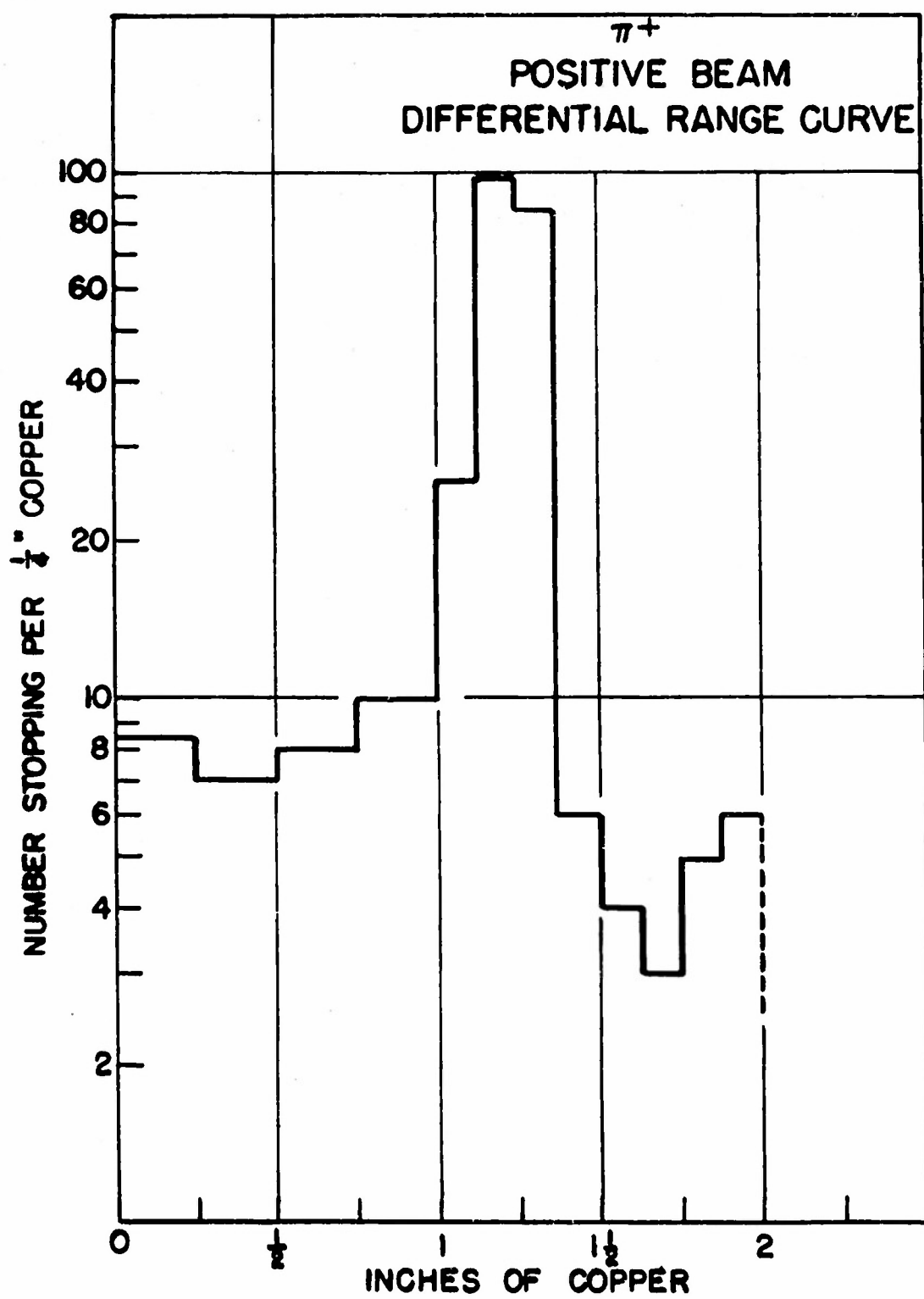


Figure 9

energy during the negative meson runs was similar, as the meson target position was unchanged. However, for positive mesons on a $1/2$ " aluminum target the value of the kinetic energy was 75 Mev after leaving counter 2. For the $1/4$ " and $1/2$ " thick targets the average distance before interaction, one half the sample thickness, would result in a loss of 1.2 Mev and 2.4 Mev respectively. In Figure 9 not many of the mesons had a range greater than $1\ 3/8$ " copper, hence the large drop in the graph at this point.

As mentioned above, both the hole in the shielding and the deflecting magnet were essentially momentum selectors. They provided a roughly monochromatic π meson beam. However, electrons and μ mesons formed near the Be target inside the cyclotron with the same momentum as the π mesons, also emerged from the channel. Since the μ meson is lighter than the π , a μ of the same momentum as the π has a greater range, equal to 1.73 inches of Cu. Thus the rise above $1\ 3/4$ " in Figure 9 corresponds to μ mesons, of the same momentum as the π 's, coming to the end of their range. These form about 4 percent of the main beam.

At 2" of absorber, about 2 percent of the original positive beam was still present, comprised most probably of positrons and a few μ 's produced from decay in flight of π 's. The positrons stopped very gradually, with increasing thickness of absorber, because of their multiplication via showers. The electrons formed a much larger proportion of the negative beam. At 2" absorber in the negative range curves, about

10 percent of the original beam remained. We assume that this was also the proportion of electrons in the incident beam. The possibility existed that the original number of electrons in the incident beam might be much higher, but that after penetrating 1.5" Cu (about 2.6 radiation lengths), only a fraction of the original number would be present. To check this, we examined Wilson's shower curves for 200 Mev/c electron in lead to obtain an idea of the order of magnitude of such a correction. Although we used copper rather than lead, a rough comparison of the two cases is possible, by measuring thicknesses in radiation lengths. It was found that, on the average, each electron in the primary beam produced several electrons of sufficient energy to trigger our last counter after traversing the absorber. Further, in one hundred cases examined, less than 10 percent resulted in no electrons (i.e., all the original energy being in γ -rays) passing through the absorber. Hence this error can result in only about a one percent error in our final beam composition, stated as approximately 10 percent electron contamination.

The range curves were also influenced by the geometric arrangement of the crystals and copper absorber. Crystal 3 and Crystal 4 were placed 4" apart with the absorber starting at a distance $3/4$ " in front of the last crystal. As copper absorber was added, some mesons near the upper and lower edges of Crystal 3 which would have passed through Crystal 4 in the absence of copper absorber, could now be multiply

scattered in the copper and thus miss the last crystal. As this effect was more important near the end of the range of the mesons, some of the slope of the range curve just before the break is attributed to this factor.

To better estimate the number of mesons stopping per unit thickness of copper, we can multiply the integral range curve by a term e^{ax} to correct for the nuclear interaction of the mesons in the copper. This, of course, overestimates the beam left after the π 's are stopped since the μ -mesons have no nuclear attenuation. Figures 10 and 11 show these plots. Also shown (Figure 12) is a range curve of the π^- mesons scattered by 1/2" aluminum at an angle of 35 degrees. One should note that in the 35 degree curve there is an additional energy loss of about 7.5 Mev in the sample. This explains the apparent different value of the range of the π 's. Also, since μ^- - mesons and electrons were absent from the scattered curve, the break in the integral curve was sharper. Figure 13 is a similar curve of π^- on aluminum at 160 degrees.

B. Stability and Efficiency Checks

During the data runs frequent checks were made to make sure that the electronics were stable and that the electronic efficiency had not varied. Thus, after a run at an angle ϕ , the turret was returned to the zero angle position in the main beam to see if the number of four-fold coincidences for a given number of 1-2 monitor counts had changed. This was generally reproducible within statistics and provided a check both on the electronics and on the turret mechanism.

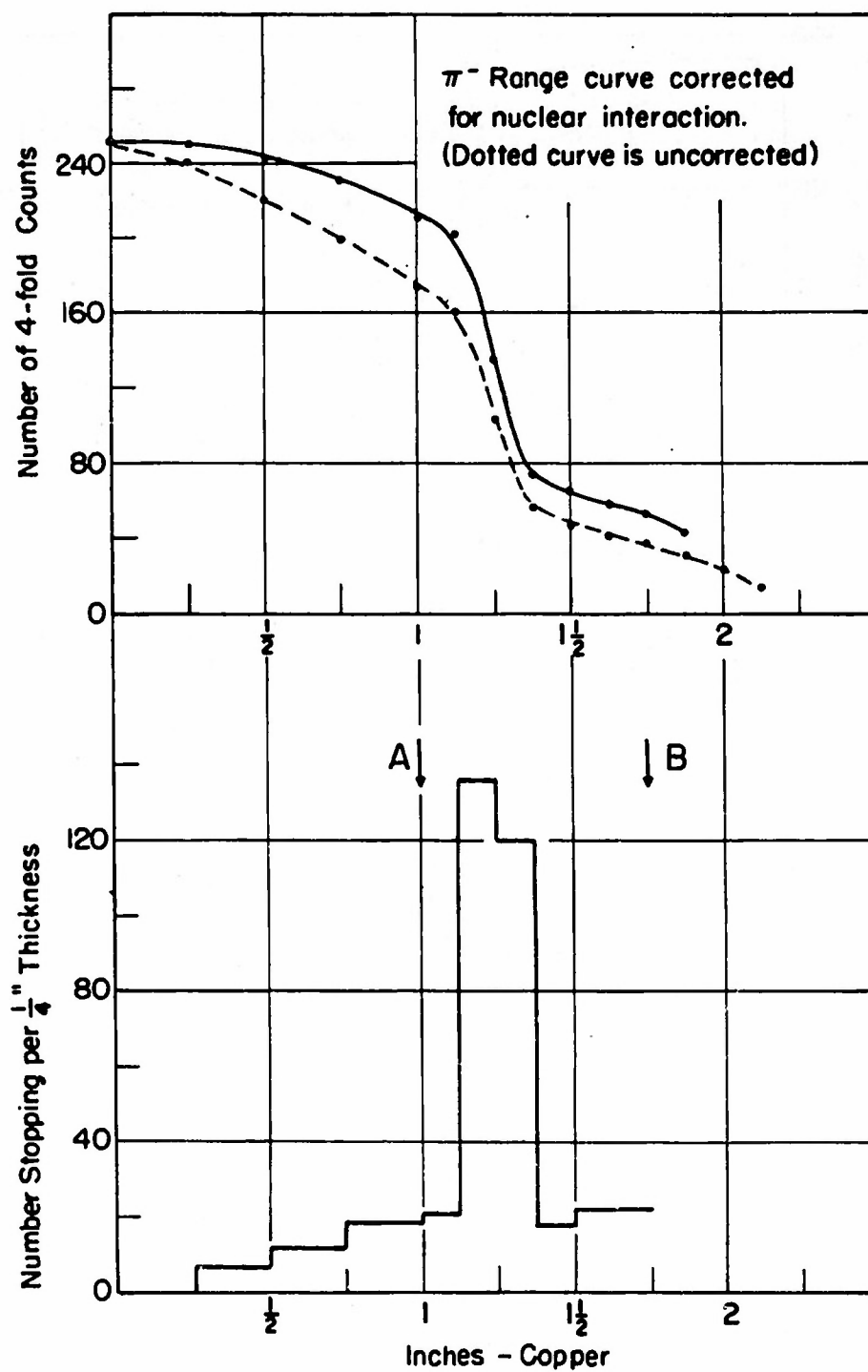


Figure 10

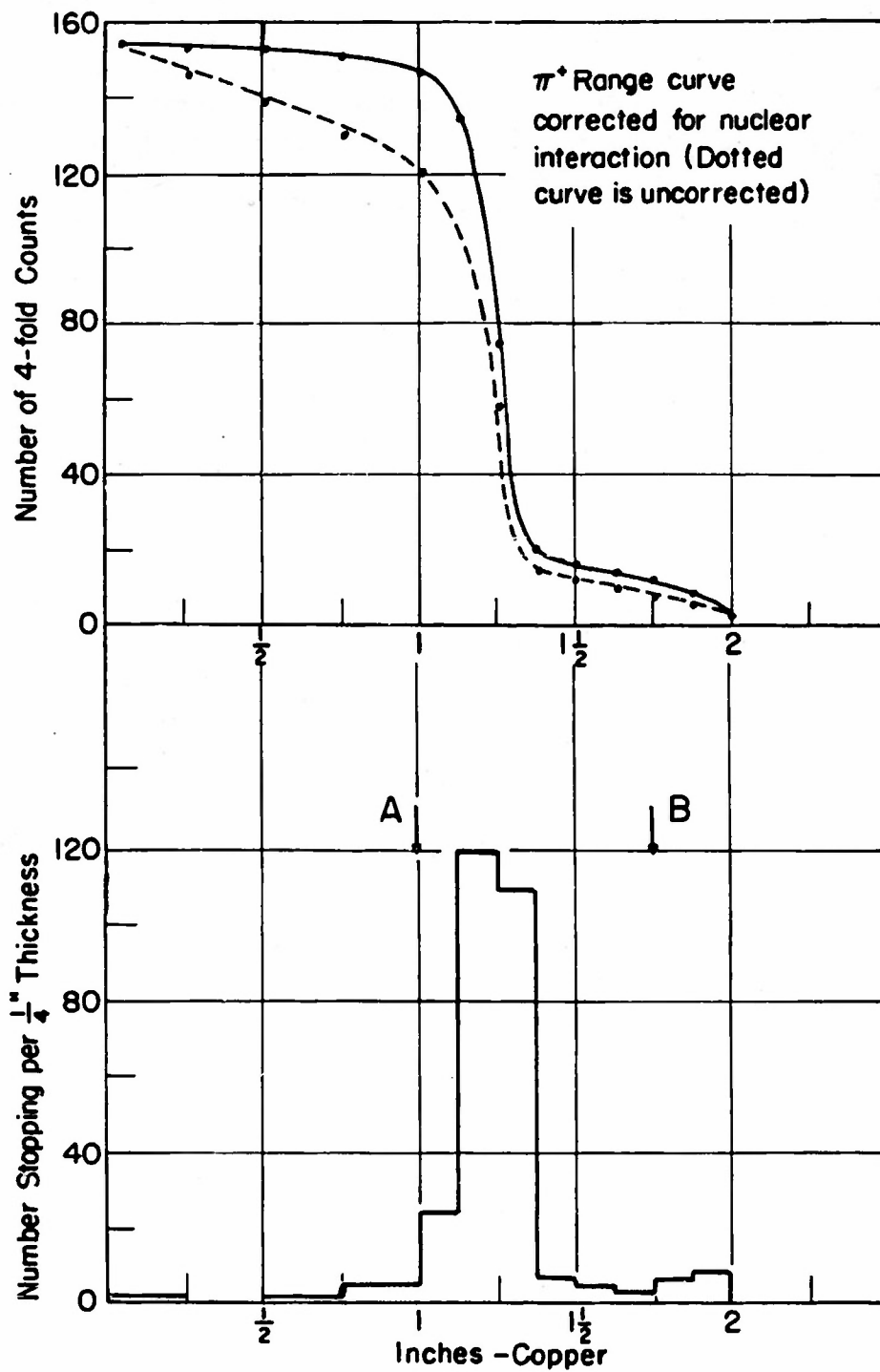


Figure 11

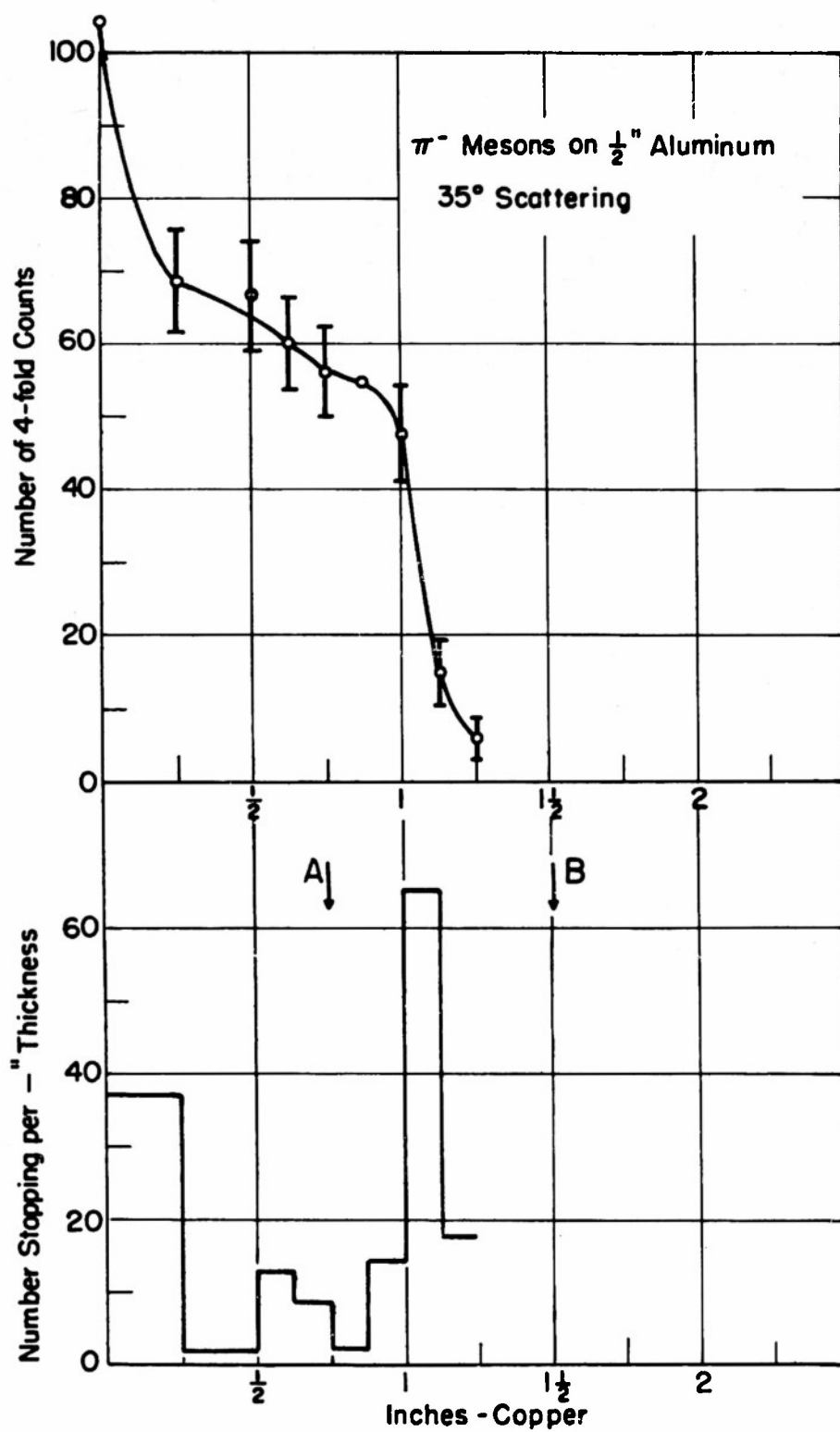


Figure 12

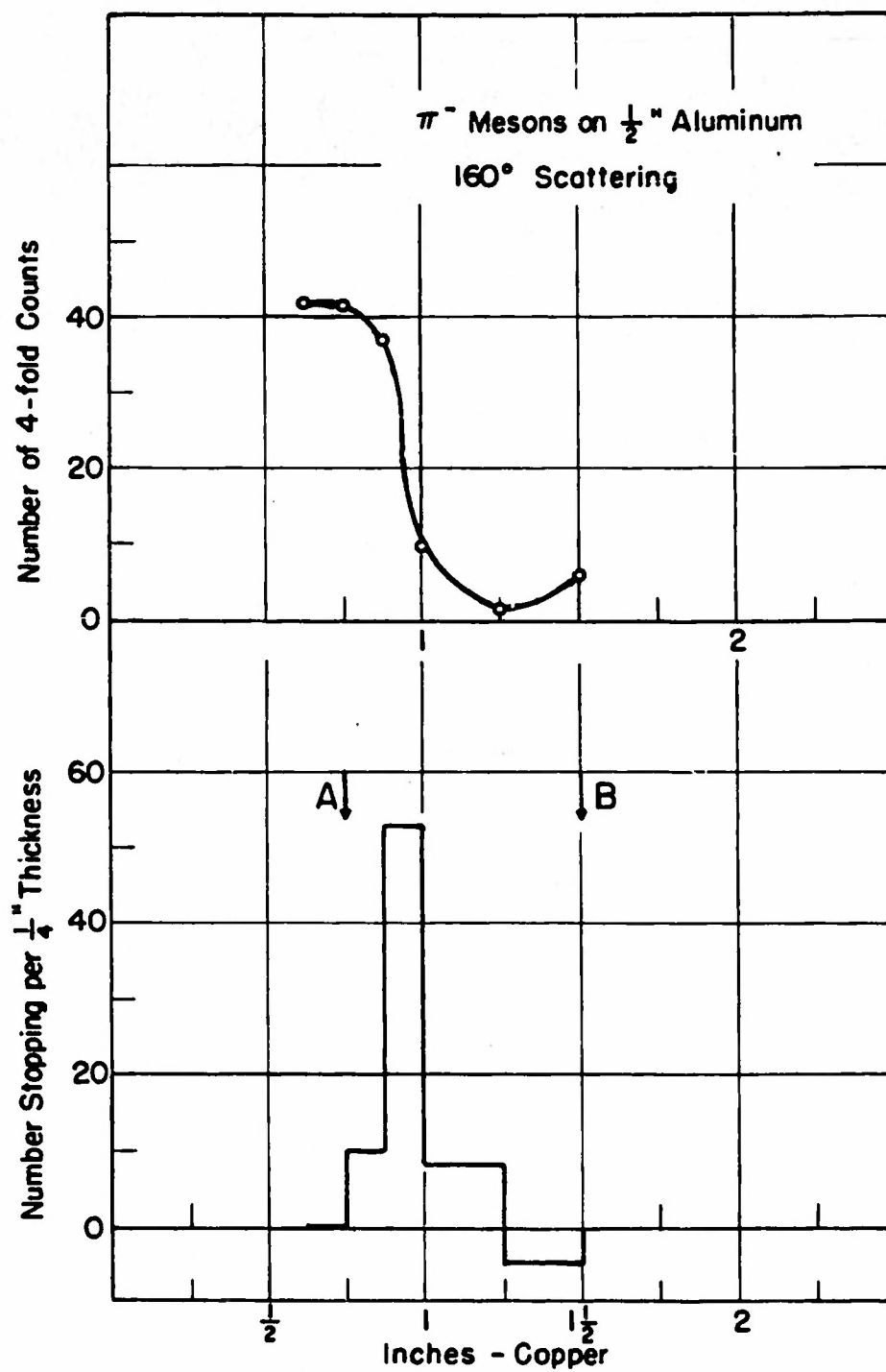


Figure 13

The electronic efficiency was measured by placing Crystals 3 and 4 in front of Crystal 2, which was smaller in size than 3 and 4. Crystal 2 was also sometimes placed between 3 and 4. The ratio of four-fold coincidences to two-fold coincidences gave the electronic efficiency for low beam intensities. At higher beam intensities the apparent efficiency decreased, since only the 1-2 circuit incorporated a fast scalar (.1 μ s resolution), while a slow scalar (4 μ s resolution) was used on the four-fold coincidences. However, after correcting for this resolution difference (and taking into account the cyclotron duty cycle), the results were consistent. At other angles to the beam direction the four-fold rate was low enough not to require correction. Efficiencies might vary on different runs due to cable length variations which were only "roughly" adjusted to peak the counting rates, but efficiencies were measured during each run, and were constant for a given set of cable lengths used during a run, which might last several weeks. In all cases, the efficiencies were of the order of 90 percent or greater.

C. Spurious Counts. Accidentals and Scattering In-Out Rate.

At all angles, runs were made for both target in and target out. The results were then subtracted to give the number of scatterings due to the target. With the target removed, a few four-fold coincidences appeared from several sources. First there was scattering (nuclear and Coulomb) from X2 which was placed close to the target. In addition, there was general background which very occasionally gave a

simultaneous pulse in each of the four crystals. However, a much more likely event was the occurrence of background pulses simultaneously in X3 and X4 in coincidence with a beam particle in crystals 1-2, since the 1-2 instantaneous rate was as high as 1,800,000 mesons per minute (90,000 per minute time averaged) during cyclotron bursts. Since the background intensity was higher near the median plane, the number of accidental coincidence counts was reduced as the turret holding X3 and X4 was rotated away from the median plane. This is also why the particular choice for fast double coincidence of X1-X2, X1-X3, and X2-X4 was made. X3 and X4 were close to each other (4"), so if a stray particle actually penetrated X3 and X4, it would have a high probability of an accidental coincidence with the high rate in X1 and X2. By pairing X1 and X3 and also pairing X2 and X4, this possibility was reduced. For now the stray particle through X1 and X2 had to coincide within the fast coincidence resolving time with the particle in X3 and X4 rather than within the slow resolving time of the Rossi circuit.

Near the median plane, the counters began to be in line with the direct beam. Thus, near 0 degrees angle, the four-fold rate actually decreased when the target was inserted. This resulted from the fact that the beam was very well collimated. When the target was inserted, multiple Coulomb scattering in the target spread the beam out so that it was not as intense in the forward direction. This sort of effect prevented us from measuring the scattering at angles below

about 10 degrees. Here the ratio of counts for "target in" over counts for "target out" was about 2:1. This was due to beam spread and also due to μ -mesons coming from the decay of π mesons in flight (the μ 's from our energy π meson had a cut-off angle of about $12\frac{1}{2}$ degrees in the laboratory system). At 15 degrees the ratio of counts for "target in" to "target out" was about 8:1. For this, and other reasons, we do not trust the results below 15 degrees. At the other angles the in-out ratio varies from as low as 3:1 up to 12:1. At 160 degrees we had a ratio of about 3.5:1. During the "target out" runs sufficient absorber was added between counters 3 and 4 to correct for the increase in energy of the measured particle with the target absent. Table 1 shows the counting rates with $\frac{3}{4}$ " copper and $\frac{1}{2}$ " copper absorber in place.

D. Criterion for Elastic Scattering

In order to measure the elastic scattering, a copper absorber was placed between X3 and X4. Low-energy protons and mesons scattered with loss of energy would not have had sufficient range to penetrate the absorber. The incident beam was only approximately monochromatic. The beam energy spread on leaving counter 2 was 80 ± 5 Mev (except for the π^+ meson case using $\frac{1}{2}$ " Al where it was 75 ± 5 Mev). Hence, to detect all the elastically scattered beam particles in Crystal 4, the absorber could not be too thick. The amount of absorber chosen was such as to stop mesons of less than 58 Mev energy after leaving the sample (the order of 7.5 Mev

Table 1. Typical quadruple counting rates as function of absorber thickness for π beam, $1/2''$ Al. target.

<u>Angle °'s</u>	<u>Inches Copper between X3 & X4</u>	<u>Target</u>	<u>Relative quadruple rates (Not to be compared at dif- ferent angles)</u>
10°	3/4	In	498
	1	Out	239
	1-3/4	Out	14
15°	3/4	In	241
	1	Out	50
	1-1/2	In	24
21-1/2°	3/4	In	193
	1	Out	35
	1-1/2	In	16
35°	3/4	In	87
	1	Out	16
	1-1/2	In	7-1/2
42-1/2°	3/4	In	36
	1	Out	5
	1-1/2	In	5
122°	3/4	In	35
	1	Out	4
	1-1/2	In	4-1/2
160°	3/4	In	49
	1	Out	16
	1-1/2	In	10

is lost traversing $1/2''$ of aluminum). This allowed, of course, inelastically scattered mesons with a $\Delta E = 45 \pm 5$ Mev to be detected and counted as elastically scattered particles. If this were an appreciably large part of the cross section it would obscure some of the results, particularly in the backward direction where the cross section for elastic scattering dropped to its lowest value, and would have to be considered in the interpretation of the results. Photographic emulsion experiments indicate that inelastic scattering with an energy loss of 20 Mev or less is quite small.¹⁰ But to check this result ourselves, rough range curves at a few angles were taken. The 35 degree curve is shown in Figure 12. At small absorber thickness, inelastically scattered mesons, plus reaction products such as protons, can penetrate the absorber to give four-fold coincidences. This number should decrease as the absorber is increased. At the scattering angle of 35 degrees the uncorrected range curve is fairly flat between $5/8''$ and $7/8''$ copper thickness, indicating that there is not much inelastic scattering of π -mesons in this region. The curve falls rapidly at a range corresponding to that of the primary beam. In fact, the fall-off is sharper and clearer than the range curve in the incident beam. This is to be expected as both electrons and μ -mesons in the main beam would not be expected to scatter into large angles. Thus the appearance of the plateau assures that at least within the spread of the beam energy we do not have appreciable contributions from inelastic scatterings of more than a few Mev.

E. Additional Checks

A further check on the nature of the scattered particles was frequently made by inserting 1 1/2" of copper between X3 and X4 with the target in, and 1 3/4" of copper with the target out. As can be seen from the incident beam range curve, this was enough copper to cut out most of the incident mesons. It was to be expected, therefore, that the ratio of scattered mesons at a given angle with 3/4" copper between X3 and X4 to the number with 1 1/2" copper, should be at least as good as this ratio in the incident beam. This was in fact the case, thus further assuring us that there was no large spurious background causing the counts measured.

The angle of scattering was measured by reading a protractor one foot in diameter mounted on our scattering stand. The zero angle was usually checked at the beginning and end of the runs to make sure it had not shifted due to slippage of the pointer arm or some other cause. Actually, the stand proved quite stable, the zero being reproducible to about an eighth of a degree. To measure the zero angle, the number of four-fold coincidences for a given number of 1-2's was measured for the different angles through which the turret was swung. A typical curve for π mesons is shown in Figure 14 from which it is seen that the zero corresponds to an angle of 1 3/4 degrees. This curve also gives an indication of the incident beam width which is seen to be about 3 1/2 degrees full width at half maximum, after which it falls sharply.

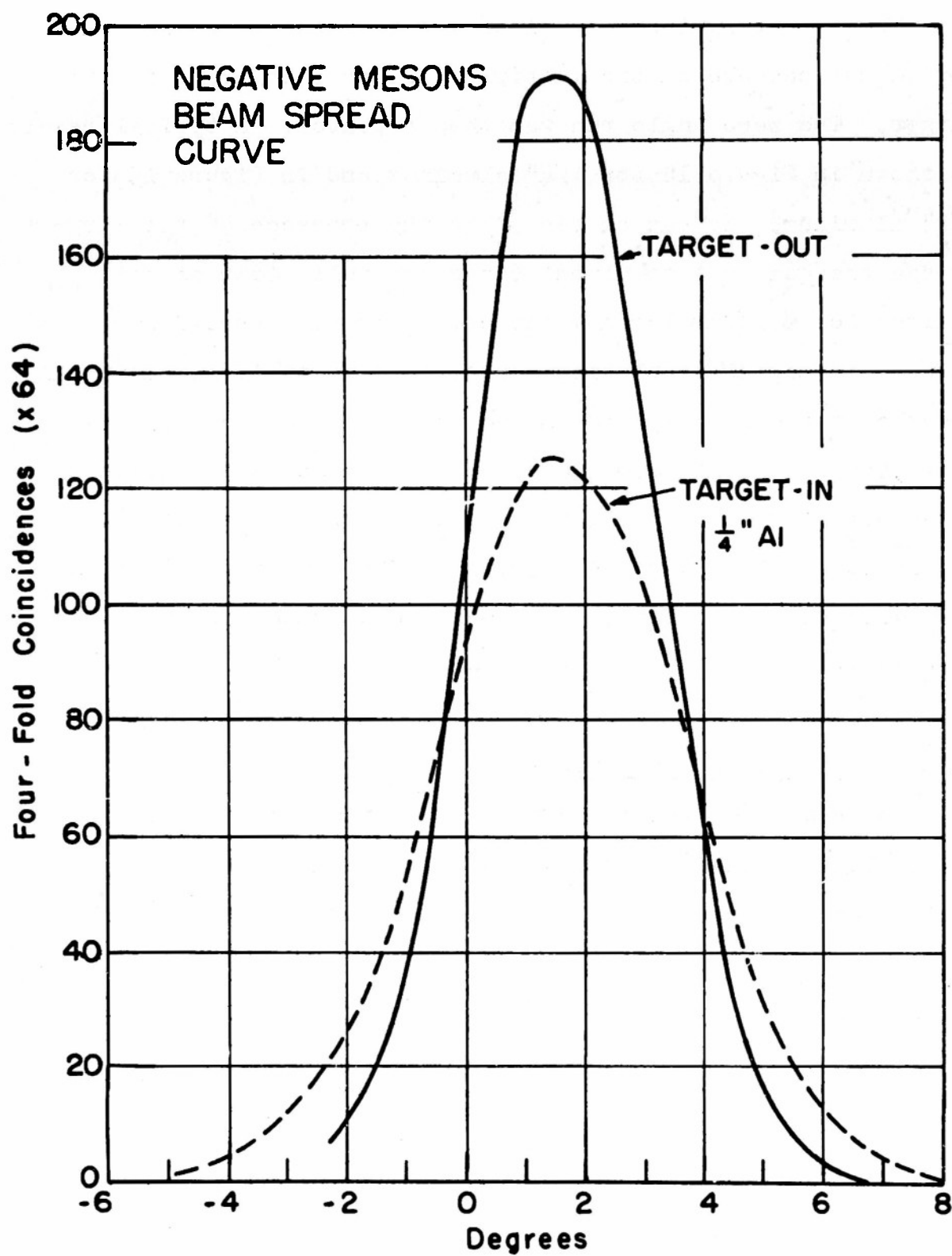


Figure 14

When the target was in place the incident beam was further spread out because of the multiple Coulomb scattering in the target. The zero angle run was then repeated. A typical result is shown in Figure 14 for 1/4" aluminum and in Figure 15 for 1/2" aluminum. It can be seen that the presence of the target spread the beam out to almost 6 degrees full width at half maximum for a 1/2" aluminum target. This beam spread curve can be used in making resolution corrections as it is an empirical measure of the beam spread including Coulomb effects, π -meson decay, and incident beam width. While most of the runs were taken with 1/2" target thickness, some data points (with poorer statistics) were taken with a 1/4" target in an attempt to reduce the beam width. The corresponding beam spread curves with a 1/4" target are shown in Figure 14.

IV. RESULTS

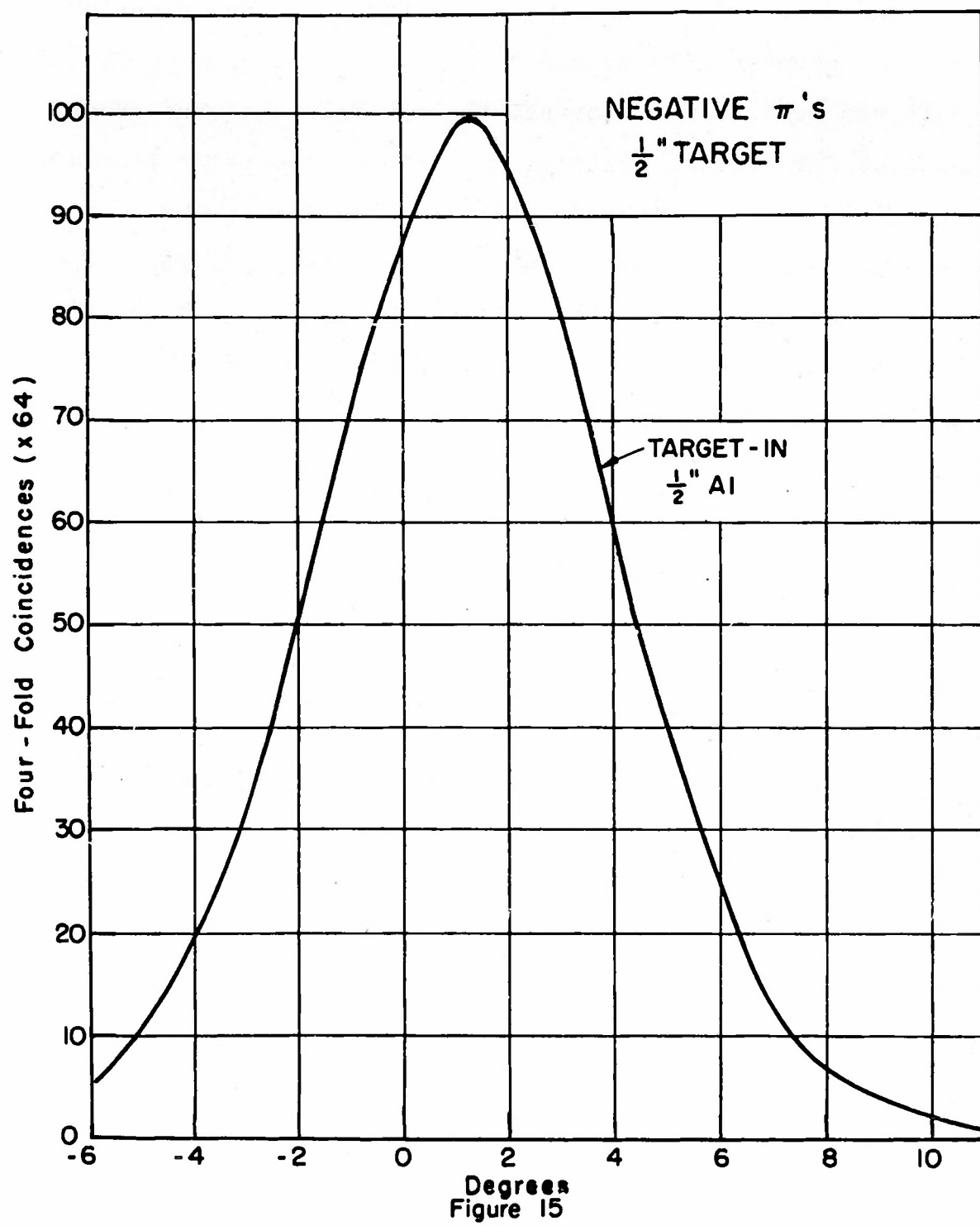
A. Calculation of Cross Sections

The cross section is defined as the number of interactions per nucleus in the target divided by the number of incident particles per unit area. The differential cross section in the laboratory is defined as

$$\frac{d\sigma}{d\Omega} = \frac{E}{\pi N \Delta w}$$

where E equals the number of events scattered at an angle θ

n equals the number of scattering centers per unit area and is given by Avogadro's number times the density in gms./cc times the thickness of the target in cm., divided by the gm. atomic weight of the target -



N equals the number of incident particles -

Δw equals the solid angle subtended by the detecting counter telescope.

It was necessary to correct the raw values of the above quantities for Coulomb scattering; nuclear absorption in the copper absorber and in the crystals; resolution of the scalars; for the angle of the target with the main beam; and for electronic efficiency as discussed below. Figure 16 and Table 2 compare the corrected results for negative and positive mesons on 1/2" aluminum. The errors shown are the standard deviations of the number of counts as it is believed that the statistical errors overshadow the systematic ones. The angular resolution varied from point to point as we moved the detecting telescope in from over 40" at the small angles down to a minimum of about 10" at some of the backward angles for which there were very low counting rates. Thus our last crystal subtended scattering angles of ± 1.5 degrees up to ± 6 degrees. This angular width was superimposed on the intrinsic beam spread with the target in place (as shown in Figure 14). The intrinsic beam width was due to the spread of the primary beam and, in addition, to the multiple Coulomb scattering in the target. Thus the Coulomb scattering increased the full width at half maximum from three to six degrees with a half inch aluminum target.

In order to check the Coulomb interference region of the scattering of the positive and negative mesons, it was thought desirable to reduce the incoming beam width and keep the detecting telescope further out from the target. Hence runs were

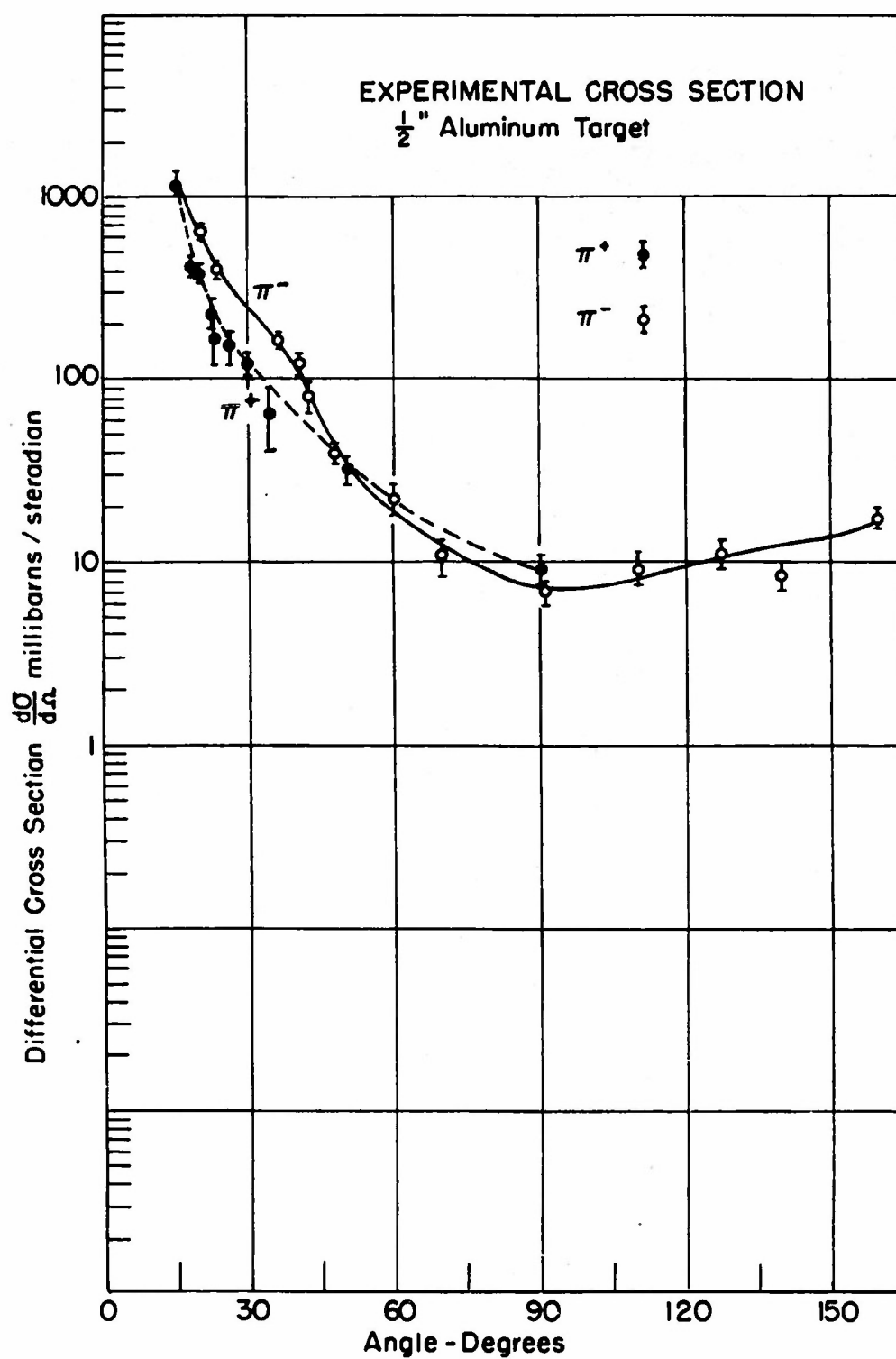


Figure 16

Table 2. Experimental results, $\frac{d\sigma}{d\Omega}$ for $1/2''$ Al. Target

π^-		π^+	
Angle o's	$\frac{d\sigma}{d\Omega}$ millibarns per steradian	Angle o's	$\frac{d\sigma}{d\Omega}$ millibarns per steradian
15 \pm 3.8	1367 \pm 65*	14 7/8 \pm 3.8	1058 \pm 96*
20 1/4 \pm 4.1	652 \pm 32	18 \pm 3.8	405 \pm 46
25 \pm 4.2	387 \pm 25	20 1/8 \pm 4.3	397 \pm 44
35 1/2 \pm 4.4	161 \pm 10	22 5/8 \pm 4.0	234 \pm 33
40 5/8 \pm 4.8	125 \pm 17.5	23 1/16 \pm 3.8	158 \pm 32
42 5/8 \pm 4.7	79.5 \pm 13.1	25 7/8 \pm 3.8	151 \pm 27
47 1/2 \pm 5.2	39.1 \pm 3.6	29 5/8 \pm 5.0	123 \pm 17
59 3/4 \pm 5.9	22.2 \pm 3.6	33 1/4 \pm 4.2	63.8 \pm 26
69 1/4 \pm 5.6	10.7 \pm 2.5	50 \pm 5.9	31.6 \pm 5.7
90 3/4 \pm 7.3	6.9 \pm 1.0	89 7/8 \pm 7.5	9.3 \pm 1.8
110 1/4 \pm 6.8	9.0 \pm 1.9		
127 1/2 \pm 6.6	11.0 \pm 1.9		
140 \pm 7.3	8.5 \pm 1.5		
159 \pm 6.4	17.3 \pm 2.0		

+ values on the cross sections are the statistical errors. The + values on the angle are the square root of the sum of the square of the half width of the incident beam angular distribution and the square of the angle subtended by X_4 .

* 15° values are not as trustworthy as values for greater angles as discussed in text.

made with a $1/4$ " aluminum target with the detecting telescope held at a distance of 40" from the target, for the 15 to 35 degree region. These results are listed in Table 3 and are plotted in Figure 17. With this target the full width at half maximum of the incident beam was $4\frac{1}{2}$ degrees and the detecting telescope subtended an angle of 1.9 degrees.

For both targets used, points were taken down to ten degrees. Points below 15 degrees are not plotted, however, as they are not considered reliable because of the large corrections (which radically vary with small changes in cyclotron operation) that would be necessary. These corrections are due to π - μ decays (which have for our energy π 's cut-off angle in the laboratory of $12\frac{1}{2}$ degrees) resulting from the large number of π -mesons in the main beam. Coulomb scattering corrections and the presence of main beam particles at low angles preclude the use of points below 15 degrees. Similarly, the 15 degree point may be considered less reliable than those at higher angles.

B. Corrections

The principle corrections were made to allow for the following:

(1) The counting of particles was not 100 percent. efficient, since many peaked very fast coincidence circuits were used. The efficiency is about 90 percent that a meson that traverses counters 1, 2, 3, and 4 will give a four-fold coincidence if it gives a 1,2 coincidence. Thus the observed 1,2,3,4

Table 3. Experimental results, $\frac{d\sigma}{d\Omega}$ for $1/4''$ Al. Target

π^-		π^+	
Angle °'s	$\frac{d\sigma}{d\Omega}$ millibarns per steradian	Angle °'s	$\frac{d\sigma}{d\Omega}$ millibarns per steradian
14 $3/4 \pm 3.1$	$1726 \pm 166^*$	14 $5/8 \pm 3.1$	$766 \pm 111^*$
17 $3/4 \pm 3.1$	687 ± 64.6	17 $5/8 \pm 3.1$	279 ± 56
20 $3/4 \pm 3.1$	521 ± 52	20 $11/16 \pm 3.1$	248 ± 47
23 $3/4 \pm 3.1$	441 ± 48	23 $5/8 \pm 3.1$	175 ± 46
26 $3/4 \pm 3.1$	328 ± 57.4	29 $7/8 \pm 3.1$	160 ± 45.5
29 $3/4 \pm 3.1$	241 ± 48.1		
33 $3/4 \pm 3.1$	124 ± 35.6		

* 15° values are not as reliable as those
for higher angles as discussed in text.

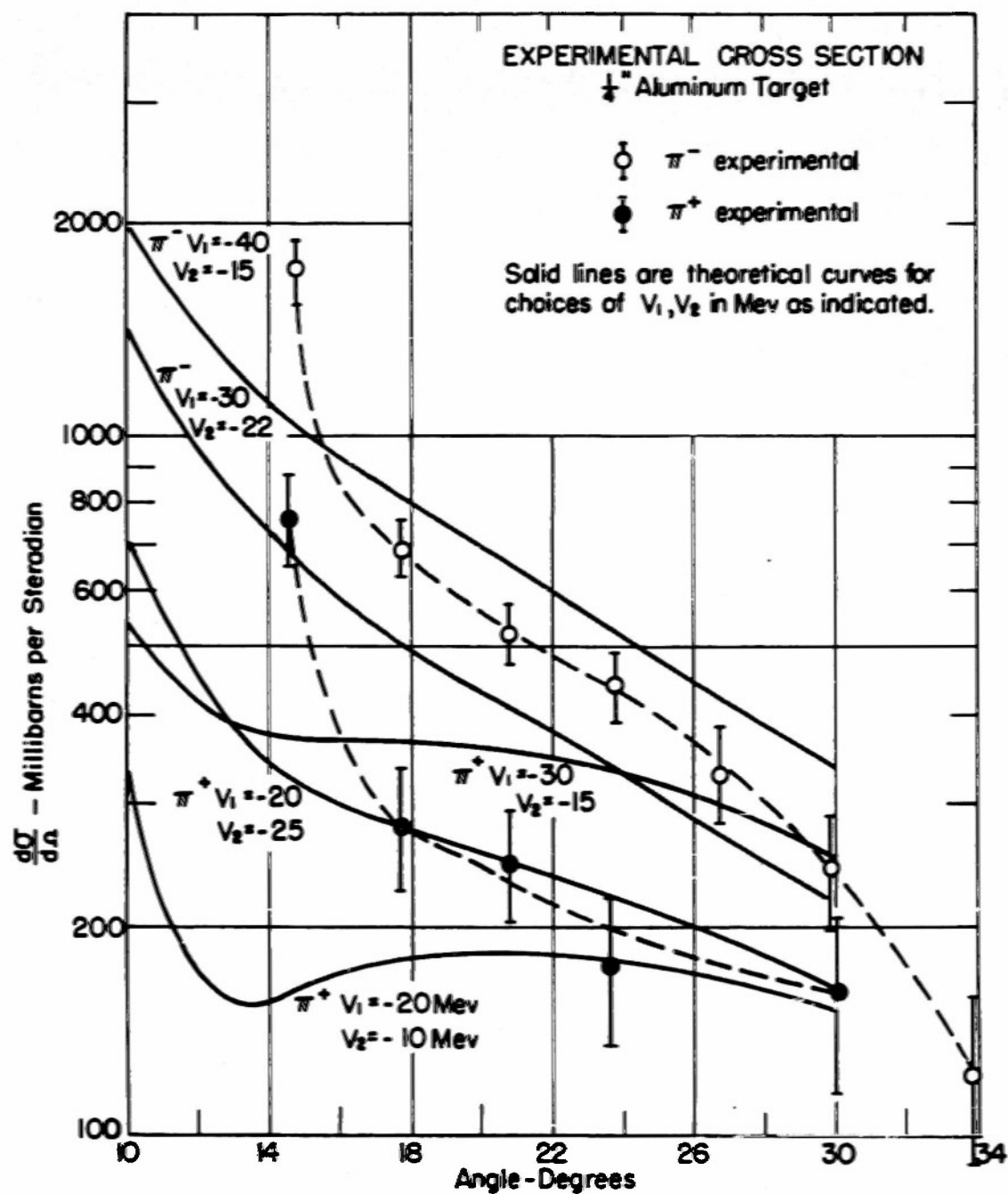


Figure 17

counting rates must be increased by about 10 percent, as discussed on pages 22 and 27.

(2) The scattered count used in calculating cross sections was the difference between the scatterer in and scatterer out count for $3/4$ " and 1" copper absorber respectively, between counters 3 and 4. Range curves taken of the scattered particles, at not too small angles, showed that there were essentially no scattered particles able to traverse $1\ 1/2$ " copper (see Table 1). Thus, of the total number of particles traversing counters 1 and 2, only that fraction of the particles which can traverse 1" copper absorber, but not traverse $1\ 1/2$ " copper absorber, should be included. Since the μ -mesons present were mainly of the same momentum as the π -mesons, their mean range was $1\ 3/4$ " copper. (The electrons had even greater ranges and are discussed separately later.) Thus an empirical check is obtained of the fraction of the 1-2 counts which should be considered valid "effective" incident π meson flux by taking a range curve in the forward direction of the 1, 2, 3, 4 rate for a fixed number of 1-2's against copper absorber thickness. If the relative 1, 2, 3, 4 rate for no absorber is taken as unity, then the difference in 1, 2, 3, 4 rate for 1" copper and for $1\ 1/2$ " copper gives the fraction f of the 1, 2 count which should be considered effective incident "correct range" π -meson flux. Note that this automatically takes account of shorter range particles in the incident beam due to absorption, inelastic scattering, and

large angle coherent scattering in the copper absorber used between counters 3 and 4 when measuring the scattered intensity. The value of f differed slightly for different runs, but was equal to about .69 for the π^+ runs and .5 for the π^- runs.

(3) The next correction is due to the net effective angular resolution function in the experiment, including contributions due to multiple scattering in the target. The net total resolution function, including multiple scattering angular smearing, is measured directly by measuring the angular spread of the beam (quadruple counting rate vs 3-4 telescope angle) in the forward direction with the sample in the beam (Figure 15). We need merely note that any larger angle single scattering event is superimposed on this distribution since the relative probability of all other smearing effects is not changed by the presence or absence of the large angle single scattering. Thus at angles appreciably larger than the measured main angular spread of the incident beam (after traversing the sample) the experimentally observed scattering distribution may be regarded as the true single scattering distribution viewed with a net experimental angular resolution function measured in the manner described above. This net angular resolution, which is directly measured experimentally, includes such effects as the angular spread of the beam on leaving counter 2; the widths of the counters; multiple scattering in the sample and counter 2; π - μ decay of the π -mesons after scattering in the sample (the decay μ -meson must be able

to traverse the copper absorber between 3 and 4 to register, so a modified π - μ angular decay function applies).

The net angular resolution function has the usual effects in distorting the "true" $d\sigma/d\Omega$ curve. If a Taylor series expansion of $d\sigma/d\Omega = g(\theta)$ is made about $\theta=\theta_1$

$$g(\theta_1 + x) = g(\theta_1) + g'(\theta_1)x + \frac{g''(\theta_1)}{2!} x^2 \dots$$

then a symmetric resolution function will give a measured $g(\theta_1)$, denoted $G(\theta_1)$, which does not depend on terms containing odd powers of x , but only on $g(\theta_1)$, and the x^2 , x^4 , etc. terms. If $g(\theta)$ has a sharp dip at θ_1 , averaging over a region about $\theta=\theta_1$ will broaden the dip and make it shallower. If $g(\theta)$ is concave upwards at $\theta=\theta_1$, $G(\theta_1)$ will be larger than $g(\theta_1)$. Since the true curves are probably concave upwards (on a linear plot) over most of their range, $G(\theta_1)$ will usually be a little larger than $g(\theta_1)$. The curvature increases rapidly at smaller angles and the correction also increases rapidly. For the π^+ scattering curve in the region of the interference dip between nuclear and Coulomb effects (near 20 degrees) the correction may be particularly large. We present the results without correcting for this effect, however, since the magnitude of the correction is quite sensitive to the assumed shape of $G(\theta)$. By assuming a hypothetical $G(\theta)$ given by the upper curve shown in Figure 18, and making the necessary resolution correction, we obtained for $g(\theta)$ the lower curve in Figure 18.

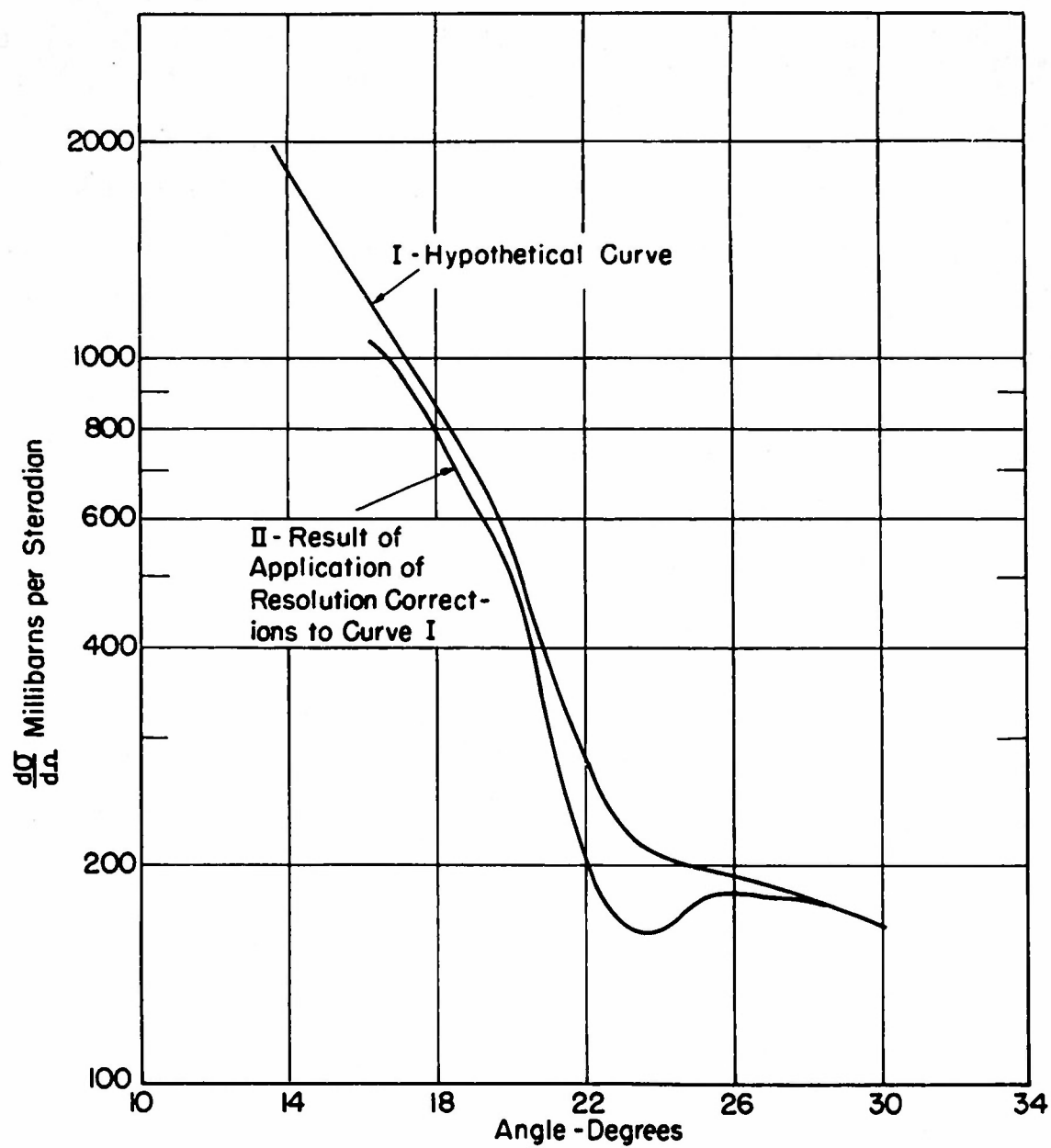


Figure 18

V. DISCUSSION

A. "Optical Model"

An attempt was made to match the experimental results using an "optical model". The term "optical model" is often employed to designate the particular approximation method (of solving the more general "optical model" problem) which was employed by Fernbach, Serber, and Taylor¹¹ (F. S. T.). By "optical model" we here mean that, in the most general sense, the wave equation to be solved for an incident plane wave plus outgoing scattered wave can be represented by a wave equation:

$$\nabla^2 \psi + k^2 \psi = 0$$

where $k(\vec{r})$ is complex and varies with position. We emphasize this distinction so the approximations involved in assuming that the actual scattering can be given, in principle, by a solution of such a wave equation with a properly chosen $k(\vec{r})$ will be separated conceptually from the consequences of further approximations made in the solution of the problem. Such further assumptions could include (1) the assumption of a uniform nuclear model, i.e. a constant nuclear density within a sphere of radius R , and zero density outside; (2) the assumption of a particular value for R such as $R = 1.4 A^{1/3} \times 10^{-13}$ cm.; (3) the approximation of using constant complex k "inside the nucleus", i.e. for $r < R$, and using the k appropriate for a Coulomb field for $r > R$; (4) then, finally, one may use various approximate methods of solving the resulting

wave equation, such as the F. S. T. method, or by use of a Born approximation, etc.

In the case of aluminum, the above choice of R gives $k_0 r = 3.6$, where $k_0 = k(\infty)$. Thus the nuclear size is the order of a wave length rather than large as compared to a wave length. Assumptions (2) and (3), although useful for making the problem definite and not overly difficult of solution, are probably poor approximations to the true situation. Since we have no trustworthy method for estimating the additional distorting effects which are introduced by the approximation methods (4) above, we decided to carry through exact phase shift calculations of the definite model resulting from approximations (1), (2), (3) above. These calculations were carried through for 16 different choices of complex $k = k_1 + ik_2$ for $R = 1.416 \text{ A}^{1/3} \times 10^{-13} \text{ cm.}$, for both π^+ and π^- mesons. k_1 and k_2 were related to an assumed complex potential $V_1 + iV_2$ using the Klein Gordon equation

$$(E-V)^2 = \mu^2 c^4 + \hbar^2 c^2 k^2$$

where μ = meson rest mass and E = meson total energy = $\mu c^2 +$ kinetic energy at large distances. The term quadratic in V was ignored for $r \gg R$ so that tabulated Coulomb wave functions could be used. Values of V_1 , V_2 , k_1 , and k_2 used for $r \leq R$ are listed in Table 4. The results of these calculations are shown in Part 2. A brief comparison of the experimental and calculated curves shows that:

(a) The calculated curves all show strong diffraction minima in the region of 60 degrees to 75 degrees. The experimental

Table 4. List of Parameters for Cases Studied

Case #	V_1 Mev	V_2 Mev	k_1 $\times 10^{12}$	k_2 $\times 10^{12}$	$\lambda = mfp$ $\times 10^{-13}$
1	-30	-15	10.40	0.920	5.5
2	-20	-10	9.77	0.627	8.0
3	-20	- 5	9.77	0.313	16.0
4	-20	- 1	9.77	0.0627	70.0
5	-10	-10	9.14	0.642	7.8
6	-5.8	0	8.86	0	-
7	0	-20	8.52	1.317	3.8
8	0	-10	8.49	0.661	7.6
9	0	- 5	8.48	0.330	15.2
10	+20	-10	7.12	0.714	7.0
11	-20	-25	9.81	1.56	3.21
12	-20	-35	9.85	2.18	2.29
13	-30	-22	10.41	1.35	3.70
14	-30	-30	10.44	1.83	2.73
15	-40	-15	11.00	0.904	5.53
16	-40	-30	11.04	1.80	2.78

curves appear to be much too smooth in this region to be consistent with this feature of the theoretical curves. The experimental angular resolution in this angular region was \pm about 7 degrees, which will reduce the effect of a sharp dip considerably, but dips as strong as the theoretical ones should still show up strongly in the experimental curves. Considering the statistical uncertainty in the measured cross sections and the spacing of the points, however, it cannot be said that much less pronounced dips are certainly absent. The absence of strong diffraction dips is in agreement with the present interpretation of electron scattering results of Hofstadter, et al.¹² and is expected for a non-uniform nuclear model where the nuclear density is higher in the center and tails off gradually in an extended surface region. One expects minima to reappear when probe particles are used which have a much shorter mean free path for incoherent processes in nuclear matter. Thus fast protons of 20-100 Mev would be expected to show minima, and π -mesons should show minima for larger nuclei, where the outer regions can be more effective in shielding the central regions. Schiff¹³ has investigated various nuclear distribution shapes in Born approximation to see how gradual a drop-off is needed to remove the minima. The arguments are as follows. If $f_a(\theta)$ is the basic scattering amplitude for a point nucleus, then $f_a(\theta)f_b(\theta)$ is the Born approximation scattering amplitude from an extended nucleus, where for a spherically symmetric distribution $p(r)$ of nuclear density

$$f_b(\theta) = \int_0^\infty n^2 p(n) \left(\frac{\sin qn}{qn} \right) dn$$

where

$$q = 2k \sin \frac{\theta}{2}$$

is proportional to the momentum change in scattering, and we have the integral of $\rho(r)$ normalized to unity over the nuclear volume. If $x = qr$, then

$$f_b = \frac{1}{q^3} \int_0^{\infty} x \rho\left(\frac{x}{q}\right) \sin x \, dx$$

If we plot $\sin x$ against x , and superimpose a plot of $x \rho\left(\frac{x}{q}\right)$, we can see how the integrand will vary with x . For a uniform nucleus $\rho\left(\frac{x}{q}\right)$ is constant for $x \leq qR$, and zero for $x > qR$. This is shown in Figure 19 for several choices of increasing q . Note that for small q (case 1) $x\rho$ has its entire weighting for $\sin x$ positive so the integrand is always positive. For larger q (case 3) part of $x\rho$ comes in the negative half cycle of $\sin x$, and the integrand is large and negative near the cut-off value $x_1 = qR$. The net amplitude from the integral will thus change sign for some value of x_1 between π and 2π and again for x_1 between 2π and 3π . The diffraction minima occur when the integral passes through zero. For the uniform nucleus the condition is $\tan x_1 = x_1$ which has roots for $x_1 = 4.49, 7.73$, etc. In order to avoid having the integral change sign, the nuclear density ρ must decrease gradually for large r so the contribution from the regions $x_1 = \pi$ to 2π , etc., of negative integrand can never exceed the contribution from the regions $x_1 = 0$ to π , etc. of positive integrand. Results of Hofstadter et al.¹² from electron scattering suggest that this may be the actual case, although the conclusions are not certain.¹⁴ The early interpretation of Hofstadter's results was

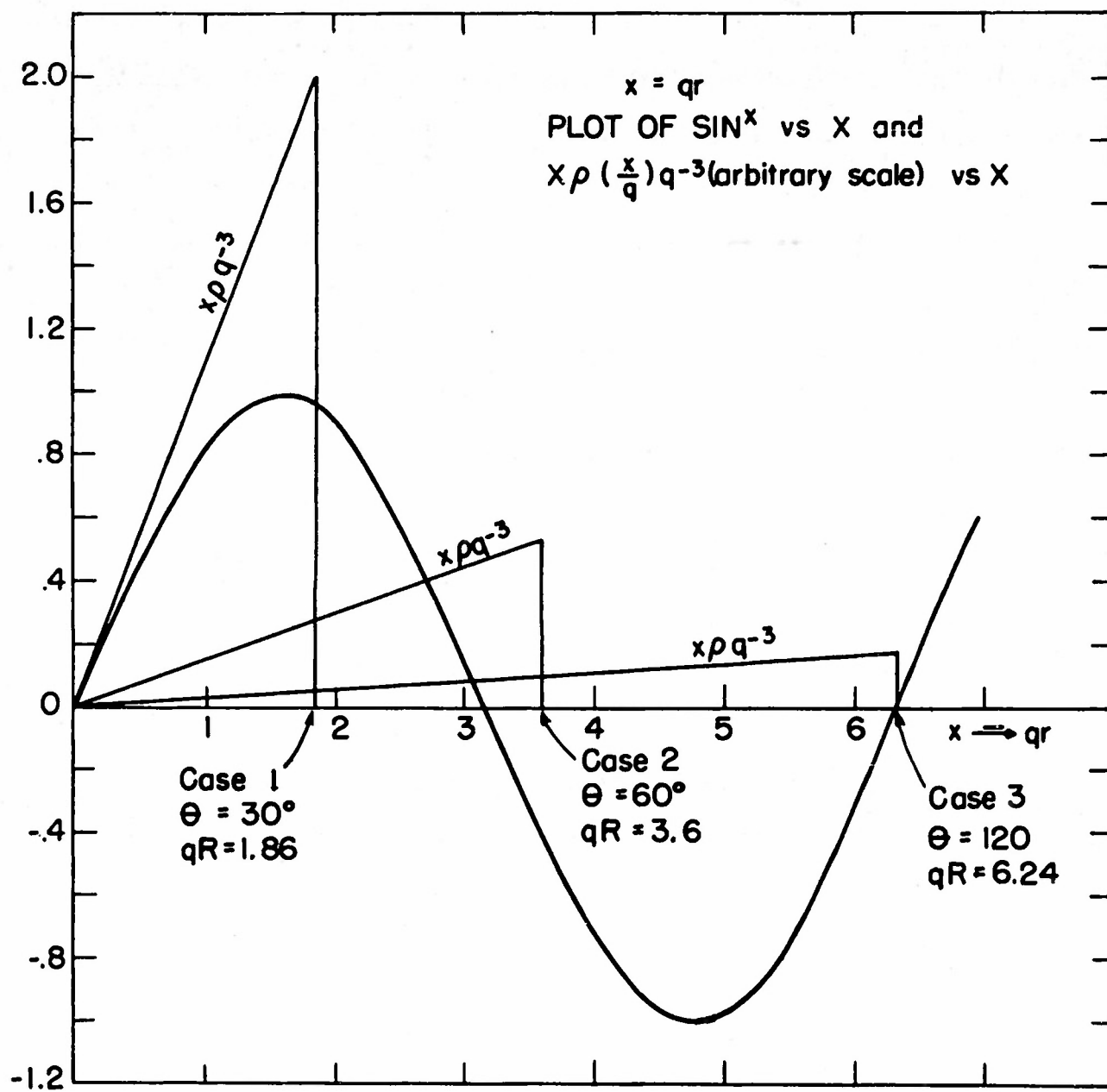


Figure 19

based on a Born approximation analysis and favored a proton density which decreased exponentially with distance from the center of the nucleus. Yennie et al have performed exact phase shift calculations for a uniform nuclear model using a range of Z values. They find that the diffraction minima are similar to the Born results for low Z but are almost completely removed for high Z . At the time this paper was written, their favored interpretation¹⁸ for $Z \sim 80$ favors a uniform nuclear model with a tail. The electron scattering for lower Z should be more sensitive to these matters.

We note that there is no attenuation shielding of the central region by the outer regions in the case of electrons. As the mean free path, λ_a , for absorption (incoherent processes) in nuclear matter is gradually decreased, the inner region of the nucleus will be more and more shielded by the outer regions, and will have correspondingly less effect on the scattering. In a rough way, we may treat this by saying that $p(r)$ in the expression for $f_b(\theta)$ should be reduced in amplitude progressively for decreasing r by the shielding effect of the nuclear matter at larger radii. In the limit the effective $p(r)$ differs from zero only near the outer edge of the nuclear distribution, say near r_m . In this limiting case f_b changes sign when $x_m = kr_m$ passes through π . This node at $x_m = \pi$ when compared with the unshielded uniform nucleus value $x_1 = 4.49$, shows that one effect of the shielding is to move the minima to smaller angles and make the nucleus appear effectively larger according to an interpretation which neglects shielding effects.

In Part 2 the selected values of λ_a were all too large to have much effect on the angle of the minima, but it was shown that fair agreement with the position of the minima using the phase shift analysis was obtained if the Born analysis used $q = 2k_1 \sin \frac{\theta}{2}$, with the value k_1 of the real part of the inside k , in place of the outside k_0 .

B. Comparison of Experimental and Calculated Curves

(1) Comparing the calculated π^+ and π^- curves in Part 2, it is seen that the π^+ and π^- curves for a corresponding set of inside nuclear potentials are nearly identical for $\theta = 30^\circ$ to 50° . (By "corresponding" potentials is meant $V_1 = -30$ Mev, for π^- and $V_1 = -20$ Mev, for π^+ , for example, where a 10 Mev difference in inside Coulomb potential is taken into account.) For $\theta < 30^\circ$ the π^+ curves show a destructive interference between Coulomb and nuclear effects, while the π^- curves have a less obvious constructive interference effect. The principle difference between the calculated curves and the experimental curves in this region is that the experimental curves place the π^+ and π^- interference separation at appreciably larger angles than do the theoretical curves. Thus the experimental separation extends from 15° to 45° , while the theoretical curves place the separation at about one-half or two-thirds of this angular region. Thus no good quantitative match can be made with the π^+ dip using any of the theoretical curves. For this reason, the best choice of V for the fit is made using the π^- curves. A detailed comparison of the experimental and theoretical π^- curves shows that a fairly good quantitative

fit can be obtained over the angular region $20^\circ - 45^\circ$ using $V_1 = -30$ Mev or $V_1 = -40$ Mev with the choice of V_2 relatively unimportant.

If one observes that the experimental π^+ and π^- curves match well for $\theta > 45^\circ$ the difference at smaller angles may be interpreted as a shift in the angular position of the interference minimum relative to those of the theoretical curves. The π^+ curve could then be said to roughly match the choice $V_1 = -20$ Mev or -30 Mev. Increasing V_2 tends to damp the amount of the dip in the calculated π^+ curves near 15 degrees and one might hope to select a favored value of V_2 on the basis of this damping. This selection is rendered quite difficult, however, in view of the great difference in position of the interference in the experimental and theoretical curves. The experimental curves of Figure 17 for the $1/4$ " aluminum sample have much better angular resolution than those of Figure 16 in the region below 30 degrees, and a much better match with the theoretical curves is possible. In making the comparison, however, we note that all of the experimental points should be lowered somewhat. In particular, those at 15 degrees are probably much too high due to contributions from still smaller angles because of the resolution width. The theoretical curves are shown corresponding to $(V_1, V_2) = (-30, -22)$ and $(-40, -15)$ for π^- , and $(-20, -10)$, $(-20, -25)$, and $(-30, -15)$ for π^+ . Comparison shows that $V_1 = -30$ to -34 (Mev) is required for the π^- curve. The π^+ curve cannot be matched perfectly due to the fact that the theoretical curves maintain low cross sections

to much lower angles than the experimental curve. Reference to Figure 17 and Figures 23 and 24, and noting something like the "area" of the dip, as well as the match for $\theta = 18^\circ$, suggests again the $V_1 = -20$ Mev is best. The theoretical curve for $V_2 = -25$ Mev seems overdamped and that for $V_2 = -10$ Mev seems underdamped, so a value for V_2 between -10 Mev and -25 Mev seems best.

(2) It is of interest that the experimental scattering cross section, in addition to showing no nuclear size diffraction minima, maintains a fairly high value near 90 degrees, and actually rises some in the backward direction. The optical model phase shift and Born approximation calculations both give a steady decrease in $\frac{d\sigma}{d\Omega}$ between interference minima. We note that a Born approximation calculation of the optical model is equivalent to assuming isotropic scattering from each element of nuclear matter, so the net $f(\theta)$ due to the nuclear effects alone has just the shape of the nuclear distribution form factor $f_b(\theta)$. Another approach would be to use the $f_a(\theta)$ indicated by the meson-nucleon ($\pi^+ + p$ and $\pi^- + p$) coherent scattering. The experimental curves of $\frac{d\sigma}{d\Omega}$ for $\pi^+ + p$ are peaked in the backward direction and the value at 180 degrees is a rapidly increasing function of the relative energy. We note that, for the backward scattering of a meson by a nucleon in the nucleus to be elastic and coherent with respect to the nucleus as a whole, the nucleon must, after absorbing the full momentum transfer, still be in the same quantum state. The fact that this becomes increasingly difficult as θ is increased

is just reflected in the decrease in the calculated coherent form factor and hence is automatically taken into account if $\frac{d\sigma}{d\Omega}$ for the elementary scattering is nearly independent of the energy of the relative motion. The collisions which contribute mainly to the coherent back scattering correspond to selecting Fourier momentum components from the bound nucleon wave function which are directed towards the meson initially, and which are directed away from the meson after the collision. Since the nucleon wave function is not changed for coherent scattering, over-all energy and momentum balance is made, noting that the nucleus absorbs the recoil as a unit. The feature to notice is that the main contribution to the coherent back scattering comes from meson-nucleon collisions where the relative motion energy is much larger than if the nucleon were stationary. Thus backward meson-nucleon $\frac{d\sigma}{d\Omega}$ curves for 110 Mev or 135 Mev may be more suitable to use than those for 80 Mev. However, there is a factor of 3 to 5 increase in $\frac{d\sigma}{d\Omega}$ at 180 degrees in going from 78 Mev to the higher energies. This is capable of giving a qualitative explanation of the rise in $\frac{d\sigma}{d\Omega}$ at larger angles, but it should be emphasized that this explanation lies outside of the concept of an optical model, i.e., of the use of a wave equation with a complex $k(\vec{r})$. It does point a direction in which one might modify the optical model results by taking account of the angular dependence $f_a(\theta)$ of the elementary nucleon scattering process. Multiple scattering effects will probably tend to make some $f_a(\theta)$ intermediate between that for the elementary processes, and an isotropic distribution

corresponding to $f(0)$ be the effective $f_a(\theta)$.

The value of the potential V in nuclear matter can be related to the scattering amplitudes in the forward direction of the elastic scattering of pions on protons. Suppose particles with propagation constant k are incident on a slab of material with N scattering centers per unit volume.

The effect of the scattering centers may be considered equivalent to the presence of a potential V inside the medium and a propagation constant $k_1 = k_0 + k^1$ for the particles inside the medium. Consideration of the resulting wave function for elastically scattered particles in the forward direction after traversal of the medium leads to the result:

$$k_1^2 = k^2 + 4 N f(0)$$

where $f(0)$ is the real part of the coherent scattering amplitude in the forward direction of the incident particle from one scattering center. Taking the Klein-Gordon equation for the particle inside and outside the medium,

$$(E-V)^2 = E_0^2 + \hbar^2 c^2 k_1^2$$

$$k^2 = E_0^2 + \hbar^2 c^2 k^2$$

and combining with the above equation for k_1 , we get

$$V = \frac{4\pi N \hbar^2 c^2 f(0)}{V - 2E}$$

In the case of meson scattering in nuclei we have not one type of scattering center but two, viz., neutrons and protons. The scattering of π^- and π^+ mesons off protons has been measured by Fermi et al.¹⁵ Bodansky et al.¹⁶ and using a

charge independent isotopic spin formalism (which is equivalent to assuming that, except for Coulomb effects, the scattering amplitude of π^- mesons on neutrons equals the scattering amplitude of π^+ mesons on protons) Fermi calculates the phase shifts from which the scattering amplitude for elastic scattering in the forward direction may be derived.

Suppose π mesons are incident on the nucleus. Then we can calculate $f(0)$ for the π^- on the protons. Since there are neutrons present also, we need $f(0)$ for π^- on neutrons. But we assume this equals the amplitudes from π^+ scattering from protons. Hence we can consider in aluminum the elementary scattering centers, N per unit volume, to be neutron proton pairs with a scattering amplitude equal to the sum of the scattering amplitude for π^- on p and π^+ on p . Transforming the scattering amplitude to their values in the laboratory system and evaluating V at 65, 120, and 135 Mev using the real part of the scattering amplitude to calculate the real part of the well yields the curve shown in Figure 20. It is not completely clear what energy should be used in evaluating V . In the meson-nuclear scattering experiments the laboratory energy is used and there is no net momentum transfer for forward scattering. For a bound nucleon, there are several possible complicating effects of the binding. The fact that the nucleons are moving would be unimportant if the basic scattering amplitudes were slowly varying with respect to the meson energy in a system where the nucleon is at rest. This is not true, how-

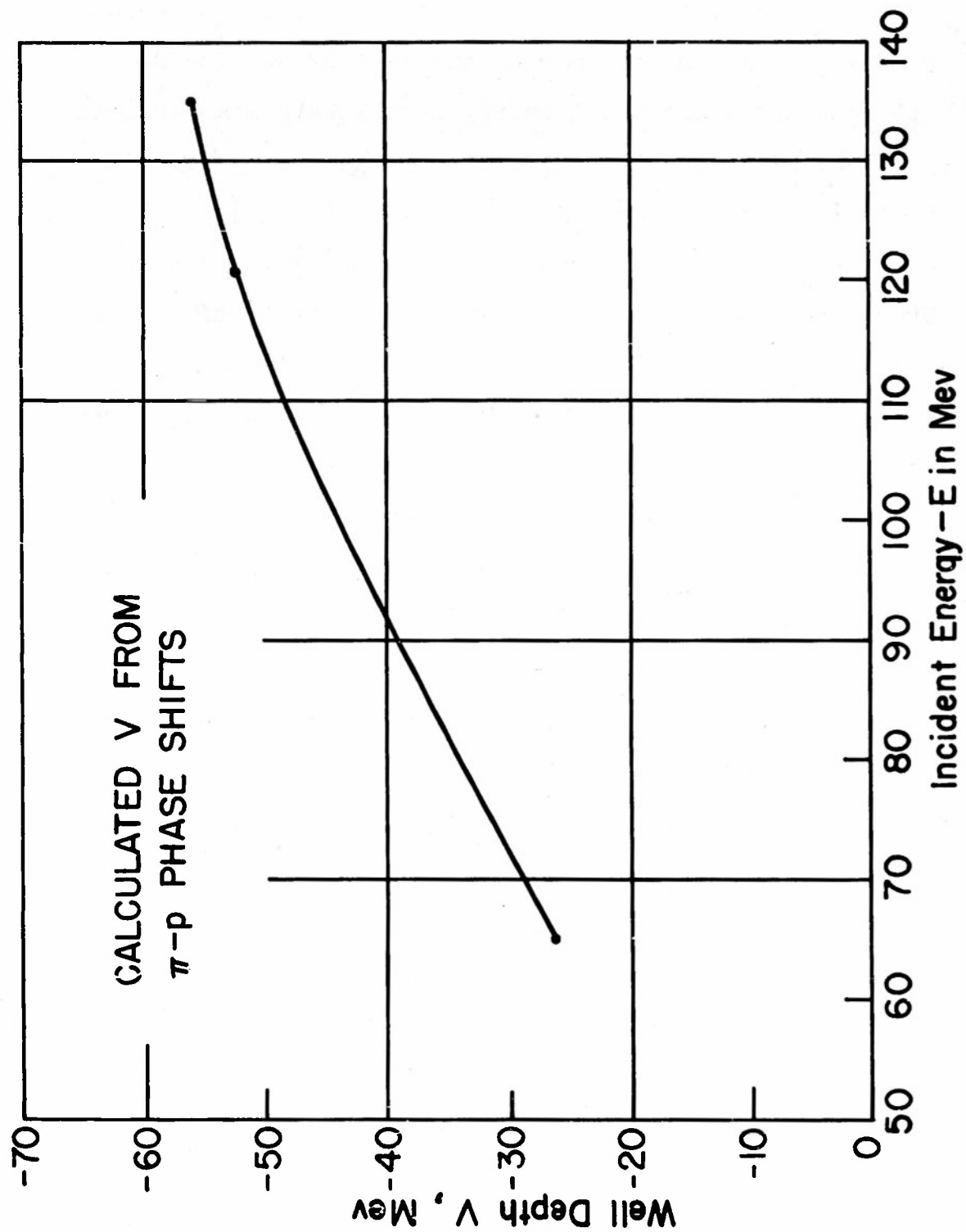


Figure 20

ever, and the nucleon momentum distribution should be considered. For a nucleon moving toward or away from the meson with 20 Mev kinetic energy ($\beta_n \sim .2$ and $\gamma_n \sim 1.02$) an incident meson of momentum P and total energy E will have momentum and energy P' and E' in the Lorentz system where the nucleon is at rest, where $cp' = \gamma_n(cp \pm \beta_n E)$ and $E' = \gamma_n(E \pm \beta_n cp)$. In this case, $\gamma_n B_n E \sim 40$ Mev. Thus some sort of weighted average of V over a region 40 Mev to 120 Mev is required. Since the curve of V vs E is roughly linear, this correction should be relatively small and an effective E of 80 or 90 Mev is probably reasonable. The kinetic energy inside the nucleus probably should be increased by the amount of the effective change in potential energy on entering the nucleus, which would favor a value of 20 to 30 Mev higher. If this is done, values of V_1 45 Mev are obtained.

A second unknown effect of the binding is the possibility of changing the effective reduced mass of the meson-nucleon system and thus appreciably changing the elementary scattering strength. This effect is almost always ignored and the conceptual features of the possible effect are often confused with an effective reduced mass effect on the amount of phase space available for scattering. To clarify the concept, at least, let us consider the scattering of slow neutrons by protons bound in a chemical lattice. For the singlet interaction, the relative wave function ψ for a square well potential behaves as $\sin Kr$ inside the range of the potential and does not reach 90 degrees of phase, so the scattering length is negative. In considering the scattering of bound protons,

it is assumed that there is no change, due to the binding, in the behavior of the relative wave function for $R \sim 10^{-12}$, e.g. If, however, the proton were bound by a spring of such stiffness that a motion of 10^{-13} cm. gave a ΔV of $\sim 10^7 \text{ e.v.}$, there would be a significant increase in the reduced mass of the relative motion, and the value of K inside the range of the force would be correspondingly increased. This could lead to a bound singlet state of the deuteron, and to a positive scattering amplitude. For atoms in a chemical lattice, the ΔV is $\sim 1 \text{ e.v.}$ for $\sim 10^{-9}$ cm. motion, so such effects are negligible. For nucleons in nuclear matter, however, it is not clear that such effects could not occur. If they did occur, the net effect might still be small unless a near resonance condition existed, as for the singlet system. It is not yet clear whether meson-nucleon interactions should be considered as having resonances, or whether the concept of an effective interaction potential defining the scattering is appropriate. It is appropriate to note that such effects are not easily excluded on general grounds and should be remembered as an interesting possibility.

Referring to Figure 20, it is seen that the value of V for $E = 80 \text{ Mev}$ is 34 Mev , which is only approximately in agreement with the value selected previously in matching the theoretical and experimental scattering curves.

Inside the nucleus we have a complex propagation constant, $k_1 = K_1 + iK_2$. The wave function inside the nucleus is pro-

portional to $e^{ik_1 r}$ so that the complex propagation constant introduces an attenuation of the incident wave function proportional to $e^{-K_2 r}$. The beam intensity is proportional to the wave function squared so that the beam will be attenuated by a factor $e^{-2K_2 r}$ corresponding to a mean free path for absorption $\lambda_2 = \frac{1}{2K_2}$. A table of λ 's for each of the cases calculated in Part 2 is shown in Table 4 together with the absorption cross sections calculated using the phase shift analysis. The calculated absorption cross section as a function of the mean free path for absorption is plotted in Figure 21. The calculated points are shown as dots and some of the curves drawn for different values of V_1 have been extrapolated in the region of long mean free path. If we choose, as above, the value $V_1 = 30$ Mev for π^- mesons and $V_1 = 20$ Mev for π^+ mesons, by comparing with measured absorption cross sections¹⁷ (which may have to be corrected for large angle elastic scattering) we can choose a mean free path λ_a . By considering the published absorption cross sections, and correcting for large angle elastic scattering where necessary, we choose a best present value of 530 millibarns for the absorption cross section of π^- on aluminum, and we choose a 10 percent smaller value, or 480 millibarns for the π^+ value. The upper solid horizontal line in Figure 21 is drawn at the π^- value, the lower at the π^+ value. The mean free path for absorption for both negative and positive mesons is then seen to be about 5×10^{-13} cm. Note that a 10 percent change in the absorption cross section would change the mean free path by a bit over

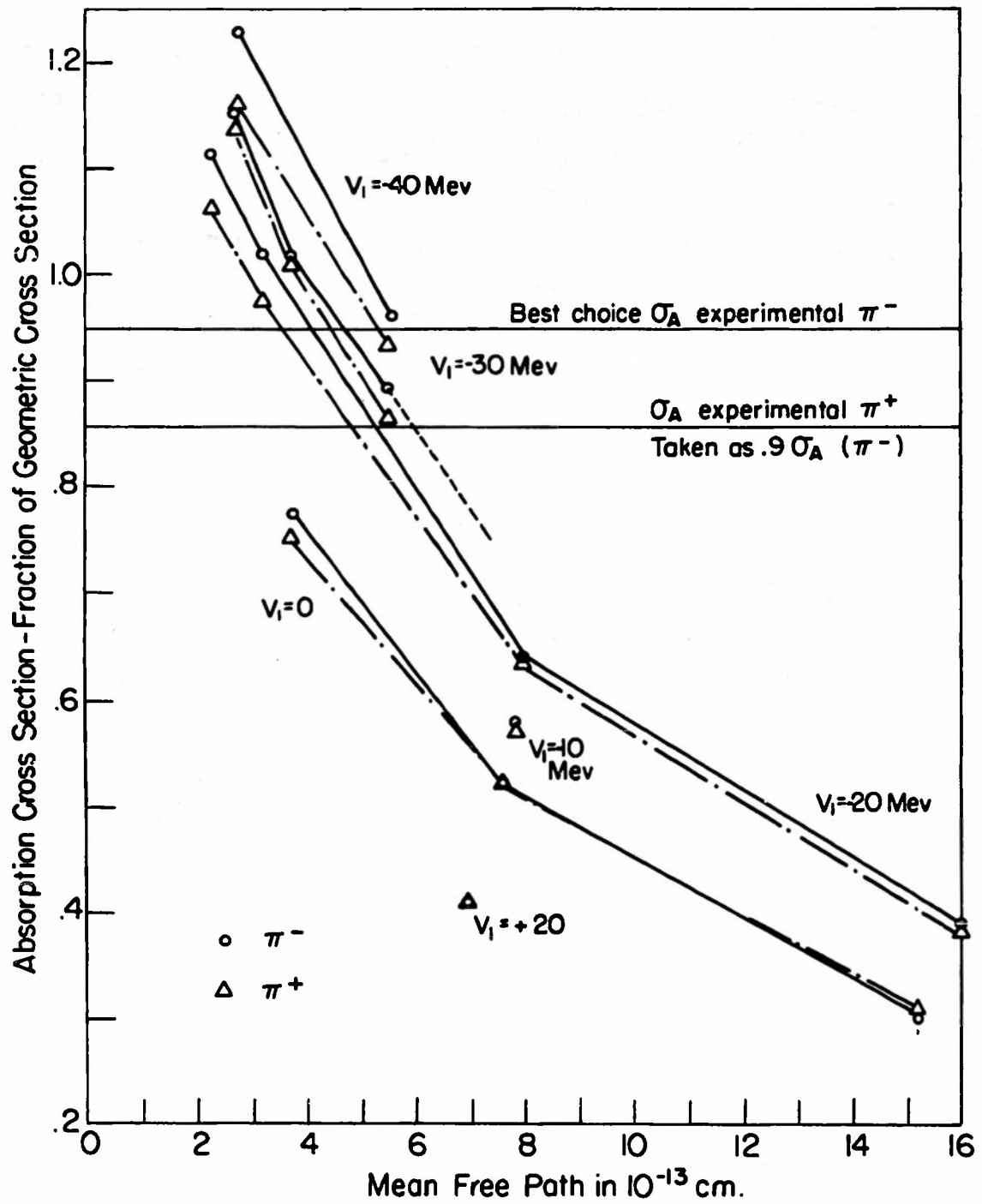


Figure 21

1×10^{-13} cm. It should be kept in mind that the mean free path calculated by this technique is of course only as good as approximations 1 - 3 above. Thus, for example, if the nuclear radius were smaller, then the measured absorption cross sections would be closer to geometric cross section and yield a smaller mean free path. Above, by matching the theoretical curves to the experimental curves in the region of small angles we saw that a value for V_2 equal to or less than 25 Mev (corresponding to $\lambda_a = 3.2 \times 10^{-13}$ cm) would fit the data but that a value of $V_2 = 10$ Mev (corresponding to $\lambda_a = 8 \times 10^{-13}$ cm) was definitely too low. This second method of determination of the mean free path thus indicates a value of λ_a between about 3×10^{-13} cm and 6×10^{-13} .

λ_a can also be estimated from the elementary pion nucleon scattering data in two different ways. First, we can calculate the imaginary part of the potential inside the nucleus, V_2 , exactly as we did the real part, V_1 , on page 57 by using the imaginary part of the forward scattering amplitude. This results in values for V_2 of -10 Mev and -37 Mev at incident π energies of 65 Mev and 120 Mev. Then at 80 Mev incident energy we would have $V = (37 + i18)$ Mev while at 100 Mev incident energy $V = (43 + i27.5)$ Mev. These correspond to about a mean free path of 4.6×10^{-13} cm. and 3×10^{-13} cm. respectively (see Table 4). These values would be lowered if effects due to absorption, i.e., disappearance of the meson, are included.

We can also consider the absorption coefficient as in

F. S. T.:

$$K = \frac{1}{\lambda_a} = \frac{3A\sigma}{4\pi R^3}$$

That is, the absorption coefficient in nuclear matter equals the particle density times the cross section for scattering of the π meson by a particle in the nucleus. This calculation gives a mean free path at 65, 80, and 120 Mev of 5.5×10^{-13} cm., 4.2×10^{-13} cm., and 1.9×10^{-13} cm. respectively. Hence at 80 and 100 Mev incident energy we would obtain mean free paths of 4.2×10^{-13} cm. and about 3×10^{-13} cm. However, the cross section for inelastic processes for bound nucleons in a nucleus will be smaller than the total cross section for free nucleons due to the Pauli exclusion principle requirement that the final nucleon state be previously empty. Thus these last values should be somewhat increased. A best speculation as to the true mean free path might be taken as 4×10^{-13} cm. for all the above calculations with the particular choice of nuclear model and nuclear size.

PART IICalculations of the Expected Elastic Scattering of π Mesonsby Nuclei

Recently the present author and others have undertaken an experimental study of the elastic scattering of π^+ and π^- mesons by nuclei. At present, the main investigations have used aluminum and lithium as the sample materials, and 80 and 130 Mev mesons. The experimental studies were undertaken with considerably greater angular resolution and statistical accuracy than earlier measurements of this type^{1,3,4}. Since measurements of this type can, in principle, yield considerable valuable information on the interaction of pions with nuclear matter, we believed that it was important to compare the experimental results with as exact theoretical predictions as would be feasible. This has led us to an examination of the methods currently favored for the calculation of such scattering. We have also carried through an extensive program of calculations of the scattering expected on the basis of an "optical model" using an exact phase shift analysis for various complex indices of refraction inside the nucleus, and using Coulomb wave functions outside the nucleus. These calculations, involving many computer hours, provide numerous test cases to compare with the results of approximate methods usually employed for this purpose. Several significant features of disagreement were found between the results of our exact calculations and the usual approximate methods which we believe should be emphasized as giving important limitations

on the applicability of the approximate analysis. These matters are discussed in some detail in the following sections.

A second general method of approach to the elastic scattering of fast particles by nuclei is based on the Born approximation, either directly or through the use of various modifications which are intended to include effects which are present in the scattering, but are not readily incorporated in the usual first order Born approximation treatment. As is discussed in more detail below, the formulae resulting from this second approach include many features not present in the optical model approach, but which we believe should be present to some extent in a more exact theory of elastic scattering. Similarly, the concepts of a change in phase relations due to the real part of the index of refraction inside the nucleus differing from the outside value, and the concepts of extinction effects due to a non-infinite mean free path for absorption (non-coherent) processes in nuclear matter are special features of the optical model which are absent from the simple Born approximation analysis, but would be expected to be present to some extent in a more exact theory. We have tested various recipes for altering the usual Born approximation formulae to consider these latter effects and, by treating cases which were also treated exactly by the phase shift analysis, are able to make detailed comparison with the exact results from the optical model phase

shift analysis. These calculations and comparisons are presented in detail in the following sections. We shall not, in this paper, be mainly concerned with the fundamental theory²⁰ used to establish the approximate validity of the differential equation which forms the basis of the optical model. Rather we shall emphasize the comparison of the predictions of the various methods of analysis discussed above using what may be considered a semi-empirical approach.

The Optical Model

The introduction of the use of an optical model to the investigation of the elastic nuclear scattering of fast particles was mainly due to Fernbach, Serber, and Taylor.¹¹ They showed that fast neutron elastic, interaction, and total cross sections when analyzed on this basis seemed to provide an excellent basis for interpretation of the experimental results. In carrying through their derivation of actual final formulae for comparison with experiment, however, they made two important simplifications which are themselves not implied by the concept "optical model", but which facilitated the analysis. These were: (1) A "uniform" nuclear model was assumed as has been customary in most treatments of nuclear processes. This considers a spherical nucleus of radius R_0 having constant nuclear density inside and zero density outside. (2) An approximate method was used to solve for diffraction effects, similar in philosophy to the usual approximate methods of dealing with interference and diffraction effects in physical optics, as opposed to exact solutions in terms of

differential equations and boundary conditions. By adopting this approximate method, they were able to explore the general behavior of the theoretical predictions over an extended range of the free parameters to an extent that would require a prohibitively large program of calculations by the exact phase shift method. Thus they were able to present an excellent preliminary survey of the subject which could gradually be improved by testing it against exact calculations for selected sets of parameters.

As a result of the general excellence of their paper, however, there has developed some confusion as to what one means by the term "optical model". The authors find that many of the physicists with whom they have discussed the matter have considered (1) and (2) above as implied features of the "optical model". However, recent experimental studies of μ mesonic x-ray transitions,²¹ and the recent studies of the elastic nuclear scattering of fast electrons,¹² at Stanford in particular, indicate that the nucleus has a considerably higher density of nuclear matter near the center than previously believed to be the case, with a gradual dropping off of the density in the outer regions (fuzzy edge). Since the basic "optical model" differential equations are capable of exact solution by a phase shift analysis of the various angular momentum components, the method need not, in principle or fact, limit itself to the approximate method of Fernbach, Serber, and Taylor.

We define the "optical model" as follows: The particle being scattered is represented at a large distance in terms

of a plane wave and an outgoing radial wave from the scatterer, which we take as centered at the origin of coordinates. (When a Coulomb field is present, the plane wave is modified in the usual way.) At all points the wave equation for the particle can be represented as

$$\nabla^2 \psi + (k_1 + ik_2)^2 \psi = 0 \quad (1)$$

where k_1 and k_2 are real functions. In a region of zero potential energy $k_1 = k_0$ and $k_2 = 0$, so

$$K_1 + ik_2 = nk_0 \quad (2)$$

introduces a complex index of refraction n . If absorption (incoherent) processes do not occur at r , and the momentum is real (positive kinetic energy), then $k_2 = 0$, and k_1 differs from k_0 due to a change in momentum (scalar value) from its value at large distances. When absorption (incoherent) processes occur at r , k_2 is positive and is the mean free path for absorption (of intensity rather than amplitude). When r represents a classically disallowed point (negative kinetic energy or imaginary momentum) the situation becomes more complex. When the non-relativistic Schrodinger equation is used, k_1 and k_2 are related to the real and imaginary parts ($V_1 + iV_2$) of the potential at r and to the energy E .

$$\hbar^2(k_1 + ik_2)^2/2m = (E - V_1 - iV_2) \quad (3)$$

If the Klein-Gordon equation is used, then

$$c^2 \hbar^2(k_1 + ik_2)^2 = (E - V_1 - iV_2)^2 - (mc^2)^2 \quad (4)$$

where m is the rest mass and E the total energy. We have used (4) for relating k_1 and k_2 to a $(V_1 + iV_2)$ for nuclear matter in treating the π meson scattering. We normally consider situations where the scattering system is very massive relative to the incident particle and can thus consider laboratory and center of mass coordinates as equivalent. Elastic coherent scattering requires that there be no change in the internal wave function of the scatterer.

In the phase shift analysis, Ψ is expanded in spherical coordinates yielding separate radial equations for each angular momentum term. If Ψ_l corresponds to the part of $r\Psi$ for orbital angular momentum l , and if we neglect spin effects, the equation for Ψ_l is

$$\Psi_l'' + \left[(k_1 + i k_2)^2 - \frac{l(l+1)}{r^2} \right] \Psi_l = 0 \quad (5)$$

with the boundary condition $\Psi_l = 0$ at $r = 0$, and Ψ_l and Ψ_l' continue at boundaries.

In the case of no Coulomb potential, this solution at large distances behaves as $\sin(k_0 r - \frac{\pi}{2} + \delta_l)$ and the scattering amplitude is then

$$f(\theta) = \frac{1}{k_0} \sum_{l=0}^{\infty} (2l+1) e^{i\delta_l} \sin \delta_l P_l(\cos \theta) \quad (6)$$

In the case where there is absorption, δ_l will be complex and the total non-coherent cross-section is

$$\sigma_c = \frac{\pi}{k_0^2} \sum_{l=0}^{\infty} (2l+1) [1 - |e^{2i\delta_l}|] \quad (7)$$

When a Coulomb term is present outside the nucleus,

there is Coulomb scattering modified by the nuclear interaction. The analysis is similar in the relativistic and non-relativistic cases if (a) terms quadratic in V are neglected in (4) for the region outside the nucleus, (b) if E/c^2 is used in place of the rest mass m for the outside Coulomb wave functions. The theory in this case can be found in Schiff.²² His equation 20.24 and 20.10 give:

$$f(\theta) = f_c(\theta) + \frac{1}{k_0} \sum_{l=0}^{\infty} (2l+1) e^{i(2\eta_l + \delta_l)} \sin \delta_l P_l(\cos \theta) \quad (8)$$

$$f_c(\theta) = \frac{-\alpha}{2k_0 \sin \frac{2\theta}{2}} e^{-i\alpha \log \sin^2 \frac{\theta}{2}} e^{2i\eta_0} \quad (9)$$

$$\text{where } e^{2i\eta_l} = \frac{\Gamma(1+l+i\alpha)}{\Gamma(1+l-i\alpha)} \quad \text{and } \alpha = \frac{Z_1 Z_2 e^2}{\hbar v}$$

$Z_1 Z_2 e^2/r$ is the Coulomb potential and v is the velocity of the particle. For a point Coulomb field, the ϕ_l behave at large r as $\sin(k_0 r - \frac{l\pi}{2} - \alpha \log 2k_0 r + \eta_l)$ showing the logarithmic variation of the phase shift at large r due to the $1/r$ type potential. When the extended actual nucleus is considered, an extra phase shift δ_l is added at large r .

To actually carry out the calculation of the δ_l values, the model of a uniform density nucleus was used with a constant complex potential $V_1 + iV_2$ inside. The logarithmic derivatives of the inside and outside solutions were matched at $r = R_0$. The inside radial solutions are of the form $\sqrt{z} J_{l+k}(z)$ where $\sqrt{z} J_{-1/2}(z) = \cos z$, $\sqrt{z} J_{1/2}(z) = \sin z$, and functions for higher l , and the derivatives of the functions are obtained from the recursion formulae for Bessel functions

$$\psi_{2+1} = \frac{(2\ell+1)}{2} \psi_2 - \psi_{2-1} \quad \text{and} \quad \psi_2' = \psi_{2-1} - \frac{\ell}{2} \psi_2 \quad . \quad \text{Here } Z = (\ell_1 + i\ell_2)\eta$$

and $(k_1 + ik_2)R = \mu + iv$, where we use $\mu_0 = k_0 R_0 = 3.600$ for aluminum and 79 Mev π mesons ($k_0 = 8.5 \dots \times 10^{12}/\text{cm}$ and $R_0 = 4.2 \times 10^{-13} \text{cm}$. The momentum was 170 Mev/c.). The regular and irregular Coulomb wave functions were taken from the tables of Bloch, Hull, Broyles, Bouricius, Freeman, and Breit,²³ and the tables of Coulomb wave functions prepared by the National Bureau of Standards.²⁴ The method of using these tables is not completely straightforward, and it has been outlined in the appendix for reference.

Two methods were used by Fernbach, Serber, and Taylor. In the one usually employed for comparison with experiment, the wave front is considered to pass through the nucleus without disturbing initial ray directions, and the relative phase and amplitudes of points on a wave front are considered after traversing the nucleus. All parts not in the geometric shadow of the nucleus have the same amplitude and phase. A point on a part of the surface for which the ray traversed nuclear matter has an additional phase $\int (k_1 - k_0) ds$, and is attenuated by a factor $\exp - \int k_2 ds$ in amplitude. (Note: Our k_2 is half of their K , which refers to intensity attenuation.) The general diffraction formula is now used and the problem treated as the linear combination of a case where the amplitude and phase on the wave front are the same in the geometric shadow as elsewhere, (giving no scattering) plus the case where the amplitude is zero outside the shadow, and equal to the (phase) vector change in amplitude due to the nucleus inside the shadow. The scattered radiation pattern

is then that due to a flat circular area and depends only on $kR_0 \sin \theta$. In particular, it is symmetric about 90 degrees. The absorption asymptotically approaches πR_0^2 as $K \rightarrow \infty$.

It is evident that the above angular pattern for the scattering can only be valid at small angles since symmetry about 90 degrees requires that all odd angular momentum terms be zero in (6). Also the Born approximation calculation, which should become exact in the limit of weak interactions, depends on the vector change in momentum in scattering, $q = 2k_0 \sin \theta/2$. Thus an improvement might be expected in their scattering formula, by replacing $\sin \theta$ with $(2 \sin \theta/2)$. They mention another formula, (9), which is based on a WKB phase shift analysis and involves a series in $P(\cos \theta)$. This would be expected to extrapolate better to large angles. The errors in this method were also discussed by Pasternack and Snyder.²⁵

Recently their approximate expression for σ_a in terms of λ_a has been used^{5,7} in the analysis of meson scattering to obtain an estimate of the mean free path for absorption of π mesons in nuclear matter from the experimental σ_a . Comparison of the approximate formula for σ_a with the results of our exact calculations shows good agreement for small $\sigma_a/\pi R_0^2$, but serious disagreement for larger K , since the exact calculation allows σ_a to exceed πR_0^2 for relatively small values of KR_0 . The results are compared in Tables 5 and 6. The discrepancy may be considered as due to the small number of λ values required. In F. S. T. a summation

Table 5. π Calculated total minus coherent scattering interaction cross sections.

Case Number	σ_r in millibarns					$\sum_{\lambda=0}^{\lambda=5} \sigma_r, \lambda$ mbs.	Fernbach, Serber, Taylor	
	$\lambda=0$	$\lambda=1$	$\lambda=2$	$\lambda=3$	$\lambda=4$	$\lambda=5$	σ	σ modified
1	35.4	93.0	184.6	152.1	33.5	3.8	348.7	474.2
2	27.3	82.5	144.0	88.6	18.7	2.1	276.2	342.5
3	17.0	51.3	90.0	48.6	9.6	1.1	164.6	204.1
4	4.1	12.4	22.0	10.5	1.9	0.2	38.4	47.6
5	26	89.8	125.6	68.5	5.8	2.5	280.7	314.4
6	0	0	0	0	0	0	-	-
7	36.8	121.9	156.5	95.4	24.5	1.5	414.9	427.3
8	27.5	92.5	104.8	54.4	13.8	3.0	285.9	285.9
9	17.3	59.1	61.2	26.7	6.7	1.0	171.6	171.3
10	34.4	78.9	69.2	35.4	7.4		300.5	231.1
11	39.0	119.4	205.9	162.9	43.8		443.1	549.4
12	41.0	125.1	213.6	186.1	57.2		489.3	611.6
13	39.7	108.4	207.4	186.7	47.4		418.8	569.6
14	41.6	117.2	217.0	208.7	60.6		476.2	635.4
15	37.6	86.6	180.5	193.0	42.0		345.5	497.5
16	43.0	112.4	214.0	242.9	73.2		464.9	688.1
$(2\lambda+1)\pi^2$	43.7	131.1	218.5	305.9	393.3	480.7		1092.5

Table 6. π^+ Calculated Total Minus Coherent Scattering Interaction Cross Sections

Case Number	millibarns				
	$l=0$	$l=1$	$l=2$	$l=3$	$l=4$
	$\sum_{l=0}^4 \sigma_{r,l}$				
1	41.3	88.8	189.7	142.7	24.6
2	28.0	79.2	152.1	81.0	13.7
3	17.1	48.8	96.7	44.2	7.0
4	4.2	11.7	24.1	9.5	1.4
5	26.1	88.4	132.9	61.5	11.6
6	0	0	0	0	0
7	36.2	122.6	160.9	85.3	18.1
8	26.8	93.7	109.8	48.3	14.3
9	16.7	60.2	64.8	25.4	4.9
10	33.5	82.8	70.6	31.0	5.4
11	39.0	116.5	210.0	149.9	32.4
12	40.8	122.7	214.9	171.2	42.6
13	40.0	104.5	210.6	175.0	35.0
14	41.7	138.5	218.0	195.1	45.0
15	41.6	82.3	181.7	186.3	30.8
16	43.1	108.7	212.6	231.0	54.5
$(2l+1)\pi k^2$	43.7	131.1	218.5	305.9	393.3
					1092.5

over l values is replaced by an integral, and this approximation fails when only the first few l values are involved in the series.

In our phase shift calculations $k_0 R_0 = 3.600$, so it would be customary to neglect terms for $l \geq 4$. To be certain that no errors were involved, however, we calculated terms through $l = 5$, and it was evident from the results that contributions from $l \geq 6$ would really be negligible. The calculated angular distribution of the cross section has been calculated for the 16 choices of complex potential each for π^+ and π^- listed in Table 4. Tables of values of the amplitude coefficients K , L , N , and M for selected angles (see equation A-8) are given in Tables 7, 8 and 9 from which all of these curves can be calculated. Tables 10 and 11 also yield the amplitudes and $d\sigma/d\Omega$ for the cases considered. It was found to be quite useful to make vector plots of $f = \frac{p + iq}{2 ik_0}$ vs. θ of the type shown in Figures 31 to 35 to interpolate values of $d\sigma/d\Omega$ between the values calculated. This was particularly true in the region of the diffraction minima, where the exact angle of the minimum, and the minimum cross-section, could be readily found. Also, it served as a check on the overall calculations since the resulting curves behaved in a regular fashion when no errors were made. If an occasional point seemed to be out of line with the general curve, an extra check was initiated and the error found and corrected. The results for a number of cases are shown in Figures 22 to 30.

Table 7. Coulomb Amplitude Functions

$$2 k f_c = K + i L (\pi^-)$$

$$= -K + i L (\pi^+)$$

θ	K	L
10	14.59880	-7.29940
15	6.80188	-2.58873
20	3.93068	-1.18705
25	2.57326	-0.62465
30	1.81676	-0.35639
45	0.84267	-0.081702
60	0.49575	-0.015044
65	0.42950	-0.0053511
70	0.34647	+0.0049134
75	0.33449	+0.0061893
90	0.24763	+0.013789
105	0.19632	+0.016565
120	0.16440	+0.017475
135	0.14420	+0.017681
150	0.13173	+0.017623
160	0.12664	+0.017567
170	0.12371	+0.017518

Table 8.

π^- Case #	M_0	M_1	M_2	M_3	M_4	M_5
1	-.72656	-.76711	-.75199	-.24288	-.02347	-.001423
2	-.44433	-.50867	-.43375	-.11583	-.01207	-.000612
3	-.29901	-.35472	-.27262	-.040287	-.00072	.000009
4	-.15192	-.21006	-.11196	.025729	.00925	.001422
5	-.36112	-.43603	-.32596	-.10360	-.01697	-.002794
6	-.007780	-.010772	.001115	.0019382	.0004	.000014
7	-.61674	-.76707	-.53778	-.19197	-.0344	-.001751
8	-.44046	-.52704	-.33356	-.11028	-.02119	-.004097
9	-.29609	-.35427	-.20746	-.064656	-.01186	-.001765
10	-1.01514	-1.05142	-.50212	-.14008	-.02221	.0007
11	-.68033	-.81185	-.73411	-.29035	-.04728	
12	-.74356	-.93249	-.85531	-.36903	-.06857	
13	-.77567	-.85425	-.84071	-.32983	-.04356	
14	-.80357	-.93067	-.91667	-.40166	-.06414	
15	-.97512	-.95117	-1.01039	-.36320	-.02522	
16	-.91551	-1.01162	-1.05860	-.50147	-.07367	
	N_0	N_1	N_2	N_3	N_4	N_5
1	.20641	.59353	.55265	.31449	.06316	.006497
2	.13043	.47182	.44814	.19875	.03645	.00384
3	.22362	.55120	.53752	.20488	.03298	.002915
4	.30967	.64347	.62254	.20642	.03189	.003703
5	-.13324	.15773	.15702	.068508	.01248	.000163
6	-.32894	-.07486	.00479	.006033	.00099	.000025
7	-.27639	-.03191	-.079293	-.026205	-.00066	-.000061
8	-.40183	-.17088	-.10515	-.030896	-.00526	-.001568
9	-.4907	-.26828	-.13685	-.038615	-.0067	-.001476
10	-.6012	-.52587	-.45183	-.16809	-.02908	.001542
11	-.03504	.34101	.23501	.13343	.03676	
12	-.099055	.30878	.13684	.078631	.03203	
13	.075173	.49615	.40859	.25292	.06200	
14	-.026921	.42371	.28518	.18386	.05761	
15	.23176	.68575	.64214	.45737	.09549	
16	-.033214	.48254	.34225	.25158	.08400	

Table 9.

π^+ Case #	M_0	M_1	M_2	M_3	M_4	M_5
1	-1.09558	-1.28571	-1.11599	-.38645	-.048827	-.004288
2	-.87256	-1.05011	-.82857	-.22728	-.029413	-.002642
3	-.85368	-1.03291	-.79879	-.17851	-.021612	-.001915
4	-.83281	-1.03263	-.76579	-.13349	-.015749	-.001693
5	-.60587	-.75596	-.51728	-.14135	-.020033	-.001789
6	-.24532	-.33858	-.16643	-.03383	-.005032	-.000496
7	-.63958	-.78109	-.47062	-.1437	-.022713	-.001216
8	-.42912	-.52998	-.31196	-.08687	-.013316	-.001497
9	-.28694	-.35218	-.19940	-.05212	-.007636	-.00053
10	-.59985	-.53006	-.16055	-.02498	-.00174	-.000955
11	-.87103	-1.11045	-.84705	-.30728	-.048577	
12	-.85553	-1.15259	-.84593	-.32618	-.057776	
13	-1.01653	-1.25724	-1.05309	-.40905	-.059173	
14	-.94899	-1.24289	-1.00118	-.41493	-.068242	
15	-1.26260	-1.45887	-1.34489	-.56226	-.065686	
16	-1.00817	-1.33499	-1.13286	-.52725	-.086683	
	N_0	N_1	N_2	N_3	N_4	N_5
1	.55139	.38243	.10681	.15569	.033977	.00323
2	.74101	.52150	.30489	.1519	.02524	.002474
3	.90917	.68619	.49876	.2009	.02903	.002375
4	1.0793	.84864	.69311	.24044	.033403	.003414
5	.64692	.41321	.20121	.07009	.00993	-.000197
6	.80857	.6499	.36292	.08996	.012569	.001124
7	.36009	.034412	-.12642	-.04605	-.005902	.000228
8	.42869	.15842	.01678	-.0003	-.01652	-.001584
9	.49120	.25317	.09475	.02147	.002308	-.000393
10	-.14183	-.49612	-.35173	-.10752	-.014814	.002118
11	.44776	.20759	-.077116	.00078	.007765	
12	.35934	.092952	-.23510	-.08540	-.005543	
13	.43399	.26032	-.054216	.05832	.023384	
14	.35192	.15947	-.19104	-.03480	.010689	
15	.36007	.29028	-.051193	.18241	.050711	
16	.25634	.12906	-.26859	-.05261	.020486	

Table 10. Differential Cross Section for π^- Mesons on Aluminum

calculated from phase shift analysis.

Case # θ deg:	1	2	3	4	5	6	7	8
10	1645.	1389.	1541.	1722.	950.	876.	650.	609.
15	721.	489.	535.	609.	244.	161.	177.	104.
20	464.	275.	291.	329.	115.	46.1	116.	46.8
25	323.	179.	184.	207.	69.9	16.3	91.5	34.3
30	222.	120.	121.	135.	45.9	6.45	71.0	27.2
45	46.8	27.2	27.6	31.2	11.2	.433	21.7	9.60
60	1.26	1.45	1.81	2.37	.898	.0042	2.22	1.33
65	.36	—	—	.564	—	.0034	.628	—
70	2.02	—	—	.540	—	.0282	.204	—
75	3.81	1.06	2.23	1.09	.159	.0226	.474	.022
90	5.68	2.49	2.48	2.83	.702	.0299	1.34	.358
105	2.33	1.49	1.64	2.04	.555	.0168	1.00	.415
120	.15	.32	.436	.640	.207	.0055	.470	.240
135	.27	.0055	.0088	.0696	.0395	.00089	.271	.106
150	1.17	.19	.164	.240	.024	.000016	.254	.066
160	1.72	.37	.354	.486	.0367	.00009	.262	.0620
170	2.09	.50	.502	.683	.0458	.00023	.267	.0619

Table 10. (Continued)

Case # θ deg:	9	10	11	12	13	14	15	16
10	599.	282.	1111.	1016.	1435.	1275.	1980.	1475.
15	75.2	83.3	445.	452.	647.	601.	1005.	771.
20	18.8	112.0	292.	323.	433.	421.	690.	554.
25	11.1	120.8	211.	242.	308.	307.	492.	404.
30	9.54	110.3	149.	174.	215.	216.	339.	280.
45	4.49	48.0	33.5	37.7	44.1	42.9	66.1	49.8
60	.830	11.0	.948	.984	.590	.318	1.46	.0038
65	.319	—	—	.611	—	.640	—	—
70	.094	—	—	2.01	—	2.94	—	—
75	.0034	2.21	2.28	3.75	4.36	5.20	9.25	8.95
90	.119	1.68	3.57	4.61	5.55	5.80	9.57	7.93
105	.185	1.33	1.56	1.79	1.89	1.77	2.63	1.63
120	.129	.952	.319	.538	.122	.265	.050	.258
135	.0645	.802	.314	.742	.468	.805	1.24	1.54
150	.0339	.752	.615	1.04	1.21	1.38	3.21	2.25
160	.0262	.743	.746	1.03	1.50	1.48	4.23	2.18
170	.0231	.746	.810	1.07	1.63	1.45	4.87	1.98

Table 11. Differential cross section for π^+ mesons on aluminum, calculated from phase shift analysis.

θ deg:	Case #							
	1	2	3	4	5	6	7	8
10	547.	344.	220.	126.	442.4	397.5	793.	692.2
15	374.	164.	125.	114.	86.6	12.9	178.	129.5
20	361.	183.	175.	189.	71.2	4.26	129.	54.4
25	325.	176.	182.	202.	69.6	15.4	123.	39.4
30	249.	152.3	164.	189.	74.0	25.2	66.5	25.4
45	69.5	50.6	57.4	67.9	24.3	13.0	23.2	10.2
60	3.51	4.88	6.71	8.47	3.50	2.90	3.58	1.97
65	.090	—	—	2.36	—	—	1.50	—
70	.906	—	—	.414	—	—	.767	—
75	3.32	.722	.561	.717	.154	1.19	.855	.228
90	8.06	4.22	4.70	5.73	1.29	.389	1.27	.300
105	4.70	3.53	4.34	5.61	1.44	.74	1.19	.454
120	.798	1.19	1.83	2.36	.738	.580	.672	.332
135	.157	.049	.127	.377	.193	.297	.345	.158
150	1.73	.269	.328	.738	.0312	.122	.191	.081
160	3.06	.720	.923	.165	.0413	.073	.124	.105
170	4.07	1.10	1.46	2.46	.0715	.054	.256	.156

Table 11. (Continued)

Case # θ deg:	9	10	11	12	13	14	15	16
10	643.	446.	702.	853.	702.	764.	774.	1000.
15	87.5	396.	314.	409.	412.	464.	614.	609.
20	22.3	70.6	254.	309.	362.	378.	567.	499.
25	13.3	126.3	210.	242.	303.	303.	474.	395.
30	8.75	80.4	162.	181.	233.	228.	361.	290.
45	4.51	29.6	42.7	47.3	61.2	55.9	88.0	62.9
60	1.06	5.00	3.26	3.39	2.40	2.12	2.16	.893
65	.506	—	—	1.42	—	.675	—	—
70	.234	—	—	2.15	—	2.40	—	—
75	.153	1.13	2.05	3.57	3.90	4.77	8.91	8.31
90	.103	.837	4.58	5.44	7.39	7.28	12.66	9.95
105	.195	.755	2.81	3.04	3.70	3.28	4.26	3.29
120	.161	.886	.841	1.01	.591	.658	.302	.380
135	.093	.496	.236	.813	.412	.791	.984	.142
150	.046	.419	.754	1.22	1.64	1.76	4.76	3.00
160	.029	.627	1.06	1.44	2.46	2.25	7.57	3.61
170	.035	.412	1.28	1.57	3.49	2.52	9.66	3.89

Table 12. Tabulation for π calculations of p, & q, where the scattering amplitude $f(\theta) = \frac{p + iq}{2ik_0}$

Case Angle θ 's	1		2		3		4	
	p	q	p	q	p	q	p	q
10	-1.02	21.7	2.44	19.85	4.38	20.6	6.24	21.4
15	-5.26	13.4	-2.01	11.7	-.195	12.4	1.53	13.1
20	-6.04	9.85	-3.07	8.35	-1.43	9.04	.145	9.74
25	-5.85	7.66	-3.22	6.41	-1.78	7.06	-.397	7.71
30	-5.27	6.00	-3.03	5.03	-1.81	5.62	-.634	6.21
45	-2.82	2.35	-1.79	2.15	-1.26	2.52	-.727	2.91
60	-.589	.126	-.536	.362	-.520	.500	-.483	.670
75	.724	-.755	.282	-.485	.060	-.529	-.142	-.543
90	1.06	-.714	.586	-.612	.366	-.761	.145	-.891
105	.743	-.346	.507	-.415	.406	-.556	.287	-.712
120	.195	-.073	.250	-.175	.264	-.236	.269	-.335
135	-.278	-.032	-.027	-.029	-.048	.016	.140	.021
150	-.557	-.163	-.237	.011	-.156	.151	-.027	.262
160	-.647	-.275	-.327	.0028	-.256	.191	-.123	.353
170	-.687	-.361	-.379	-.011	-.319	.207	-.189	.402

Table 12. (Continued)

Case Angle o's	5		6		7		8	
	p	q	p	q	p	q	p	q
10	3.28	16.2	7.28	14.1	.346	13.7	2.81	12.9
15	-1.21	8.29	2.57	6.32	-3.97	5.92	-1.66	5.22
20	-2.31	5.27	1.16	3.45	-4.85	3.12	-2.73	2.45
25	-2.52	3.71	.599	2.08	-4.80	1.83	-2.90	1.20
30	-2.39	2.74	.329	1.32	-4.37	1.15	-2.74	.575
45	-1.41	1.11	.049	.350	-2.46	.435	-1.66	.011
60	-.438	.259	-.017	.031	-.741	.303	-.619	.010
75	-.163	-.139	-.029	-.075	.268	.254	.034	.072
90	.383	-.236	-.023	-.090	-.598	.167	.308	.091
105	.350	-.192	-.013	-.068	.535	.039	.340	.062
120	.209	-.126	-.005	-.039	.356	-.093	.263	.005
135	.061	-.088	-.0002	-.016	.201	-.194	.167	-.052
150	-.039	-.073	.0018	-.0012	.103	-.250	.105	-.089
160	-.075	-.070	.0023	.0046	.063	-.267	.088	-.101
170	-.092	-.068	.0024	.0077	.039	-.274	.082	-.105

Table 12. (Continued)

Case
Angle O's

	9		10		11		12	
	p	q	p	q	p	q	p	q
10	4.45	12.4	-.276	9.01	-1.50	17.8	-3.16	16.8
15	-.115	4.65	-4.65	1.53	-5.67	9.79	-7.20	8.85
20	-1.32	1.92	-5.61	-.909	-6.36	6.61	-7.72	5.77
25	-1.65	.702	-5.62	-1.77	-6.07	4.88	-7.23	4.16
30	-1.65	.116	-5.28	-1.95	-5.40	3.71	-6.34	3.13
45	-1.09	-.310	-3.54	-1.13	-2.71	1.53	-3.00	1.36
60	-.456	-.178	-1.78	-.020	-.412	.321	-.284	.450
75	-.029	-.012	-.522	.602	.789	-.180	1.04	.053
90	.169	.076	.151	.678	.981	-.251	1.15	-.085
105	.212	.091	.418	.457	.638	-.203	.692	-.185
120	.182	.062	.486	.194	.213	-.216	.220	-.326
135	.134	.022	.481	-.002	-.080	-.290	-.058	-.459
150	.099	-.007	.445	-.135	-.233	-.350	-.187	-.514
160	.085	-.016	.416	-.201	-.286	-.365	-.234	-.508
170	.079	-.020	.393	-.246	-.316	-.365	-.263	-.490

Table 12. (Continued)

Case Angle o's	13		14		15		16	
	p	q	p	q	p	q	p	q
10	-2.45	20.2	-3.68	18.8	-3.81	23.6	-5.42	19.9
15	-6.57	12.0	-7.69	10.7	-7.89	15.1	-9.30	11.6
20	-7.18	8.54	-8.16	7.38	-8.43	11.3	-9.59	8.21
25	-6.81	6.52	-7.62	5.51	-7.97	8.84	-8.84	6.17
30	-6.02	5.04	-6.65	4.21	-7.08	6.90	-7.65	4.70
45	-2.99	1.94	-3.11	1.63	-3.63	2.42	-3.41	1.64
60	- .393	.124	- .215	.213	- .577	-.294	- .029	- .017
75	.974	-.551	1.18	-.302	1.14	-1.16	1.52	- .507
90	1.17	-.489	1.26	-.298	1.45	-.804	1.47	- .358
105	.698	-.239	.681	-.211	.856	-.160	.662	- .179
120	.107	-.147	.085	-.263	.019	+.118	- .098	- .254
135	- .281	-.236	- .255	-.408	- .595	-.059	- .462	- .481
150	- .460	-.367	- .368	-.511	- .859	-.431	- .488	- .640
160	- .502	-.425	- .381	-.529	- .894	-.648	- .426	- .668
170	- .515	-.452	- .380	-.523	- .885	-.767	- .367	- .659

Table 13. Tabulation for π^+ calculations of p & q where
the scattering amplitude $f(\theta) = \frac{p + iq}{2ik_0}$

Case Angle o's	1		2		3		4	
	p	q	p	q	p	q	p	q
10	-5.80	-11.1	-2.32	-9.68	-1.74	-7.76	-1.23	-5.88
15	-9.75	-3.56	-6.83	-2.15	-6.00	.337	-5.54	1.43
20	-10.15	-.990	-7.25	.351	-6.80	2.03	-6.41	3.66
25	-9.68	.031	-7.00	1.29	-6.67	2.80	-6.32	4.27
30	-8.44	.715	-6.35	1.88	-6.08	3.19	-5.85	4.48
45	-4.46	.324	-3.65	1.10	-3.65	1.78	-3.67	2.47
60	-1.005	.0005	-1.14	.309	-1.32	.442	-1.44	.603
75	.975	.067	.455	-.036	+.322	-.241	.177	-.418
90	1.52	.151	1.09	-.184	1.06	-.487	1.01	-.788
105	1.14	.252	1.00	-.079	1.08	-.303	1.46	-.550
120	.461	.132	.586	.0009	.723	-.059	.811	-.145
135	-.098	-.188	.117	-.022	.171	.086	.268	.191
150	-.403	-.579	-.248	-.127	-.287	.109	-.265	.378
160	-.486	-.802	-.406	-.205	-.508	.086	-.537	.431
170	-.517	-.952	-.498	-.264	-.645	.061	-.711	.452

Table 13. (Continued)

Case Angle ϕ 's	5		6		7		8	
	p	q	p	q	p	q	p	q
10	.920	-11.2	5.00	-9.46	1.00	-15.1	3.14	-13.7
15	-3.46	-3.60	.389	-1.89	3.39	-6.31	1.37	-5.95
20	-4.43	-.930	-.879	.673	-4.36	-4.24	-2.50	-3.07
25	-4.47	.202	-1.28	-1.67	-5.28	-2.76	-2.93	-1.66
30	-4.51	.994	-1.37	2.32	-4.11	-1.50	-2.63	-.624
45	-2.52	.810	-1.03	1.64	-2.54	-.490	-1.71	.010
60	-.918	.405	-.518	.754	-1.00	.152	.725	.202
75	.135	.161	-.116	.144	-.007	.496	-.054	.250
90	.606	.070	.140	-.304	.447	.409	.282	.083
105	.637	-.089	.247	-.388	.518	+.270	.358	.053
120	-.455	-.074	.259	-.316	.429	.091	.303	.060
135	.224	-.073	.222	-.190	.311	-.050	.212	.023
150	.037	-.087	.171	-.077	.220	-.080	.136	-.069
160	-.047	-.098	.143	-.022	.180	-.057	.103	-.140
170	-.097	-.106	.124	.011	.156	-.223	.084	-.194

Table 13. (Continued)

Case Angle o's	9		10		11		12	
	p	q	p	q	p	q	p	q
10	4.62	-12.8	4.19	-10.5	-3.23	-13.8	-3.52	-15.7
15	.041	-5.02	-.891	-10.6	-7.34	-6.05	-7.60	-7.74
20	-1.19	-2.24	-1.70	-4.18	-7.94	-3.19	-8.17	-4.71
25	-1.70	-.969	-1.78	-5.76	-7.55	-1.82	-7.73	-3.13
30	-1.59	-.021	-2.18	-4.29	-6.76	-1.07	-6.89	-2.15
45	-1.11	.271	-1.80	-2.30	-3.64	-.080	-3.66	-.454
60	-.497	.244	-1.20	.034	-.925	.289	-.891	.426
75	-.062	.200	-.650	.176	.632	.437	.664	.766
90	.172	.014	-.218	.440	1.07	.419	1.05	.681
105	.235	-.035	.057	.463	.862	.256	.868	.347
120	.209	-.052	.207	-.461	.492	.002	.536	-.045
135	.154	-.055	.278	.256	.205	-.261	.322	-.361
150	.103	-.051	.312	.152	.038	-.464	.207	-.556
160	.078	-.047	.327	.272	-.028	-.552	.160	-.625
170	.062	-.079	.336	.074	-.066	.603	.129	-.160

Sheet 4 of 4

Table 13. (Continued)

Case Angle o's	13		14		15		16	
	p	q	p	q	p	q	p	q
10	-5.52	-13.1	-5.27	-14.8	-8.78	-12.1	-7.09	-15.4
15	-9.47	-5.38	-9.22	-6.98	-12.5	-4.49	-10.9	-7.55
20	-9.87	-2.62	-9.62	-4.04	-12.6	-1.91	-11.1	-4.58
25	-9.23	-1.37	-8.98	-2.59	-11.6	-8.58	-10.2	-3.09
30	-8.16	- .738	-7.91	-1.72	-10.2	- .437	-8.88	-2.18
45	-4.20	- .082	-3.99	-3.87	-5.02	- .342	-4.21	- .658
60	- .822	.123	- .724	.294	- .702	- .359	- .451	+ .230
75	1.02	.299	.993	.621	1.56	.375	1.37	.712
90	1.40	.401	1.31	.618	1.86	.412	1.52	.749
105	.983	.315	.909	.343	1.10	.150	.889	.395
120	.411	.031	.430	- .067	.198	.219	.296	- .148
135	.026	- .343	.154	- .452	- .322	-4.24	.054	- .637
150	- .144	- .671	.063	- .710	- .428	-1.09	- .083	- .926
160	- .180	- .822	.049	- .804	- .376	-1.43	.151	-1.01
170	.194	- .910	.047	- .851	- .311	-1.64	.205	-1.04

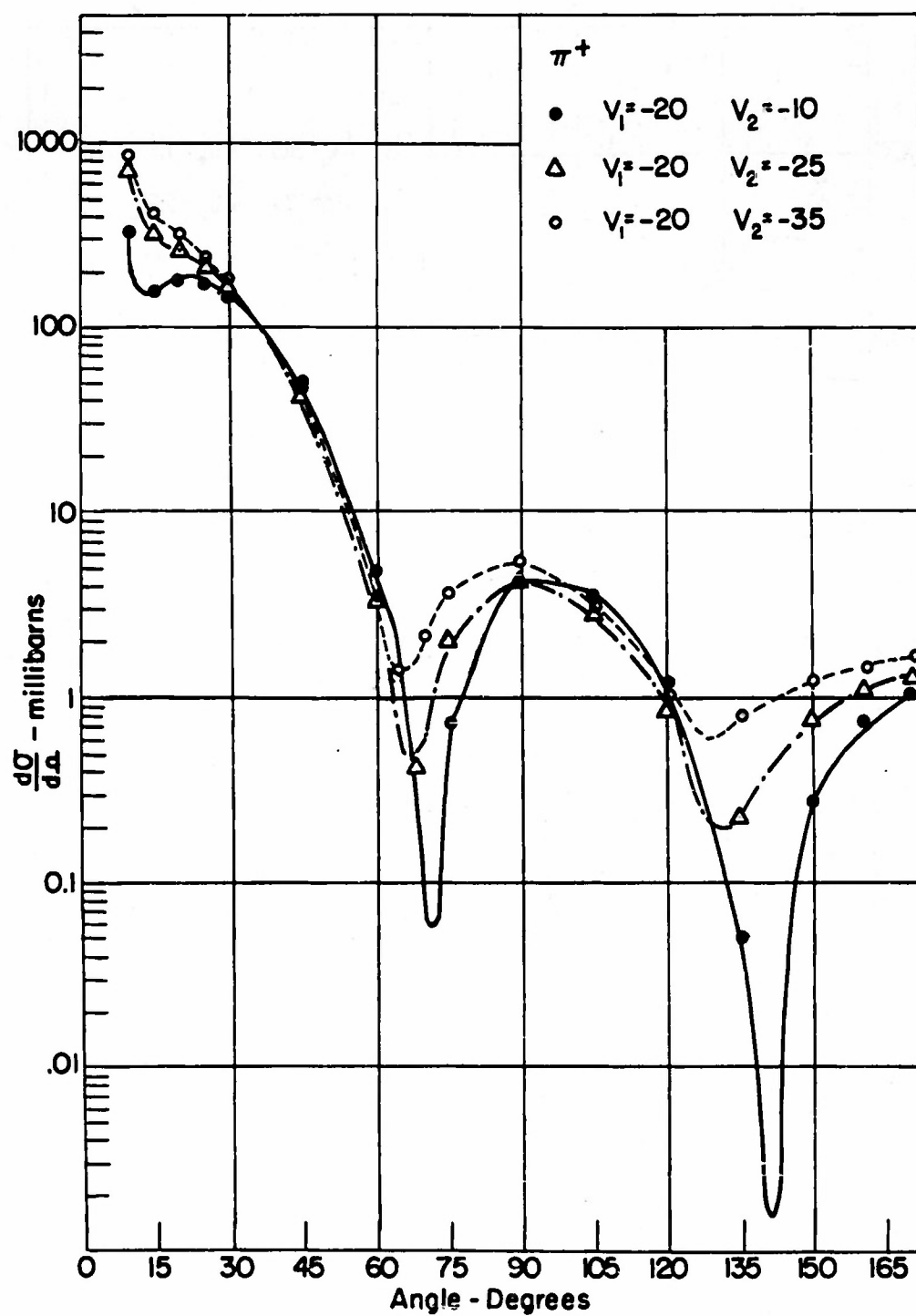


Figure 22

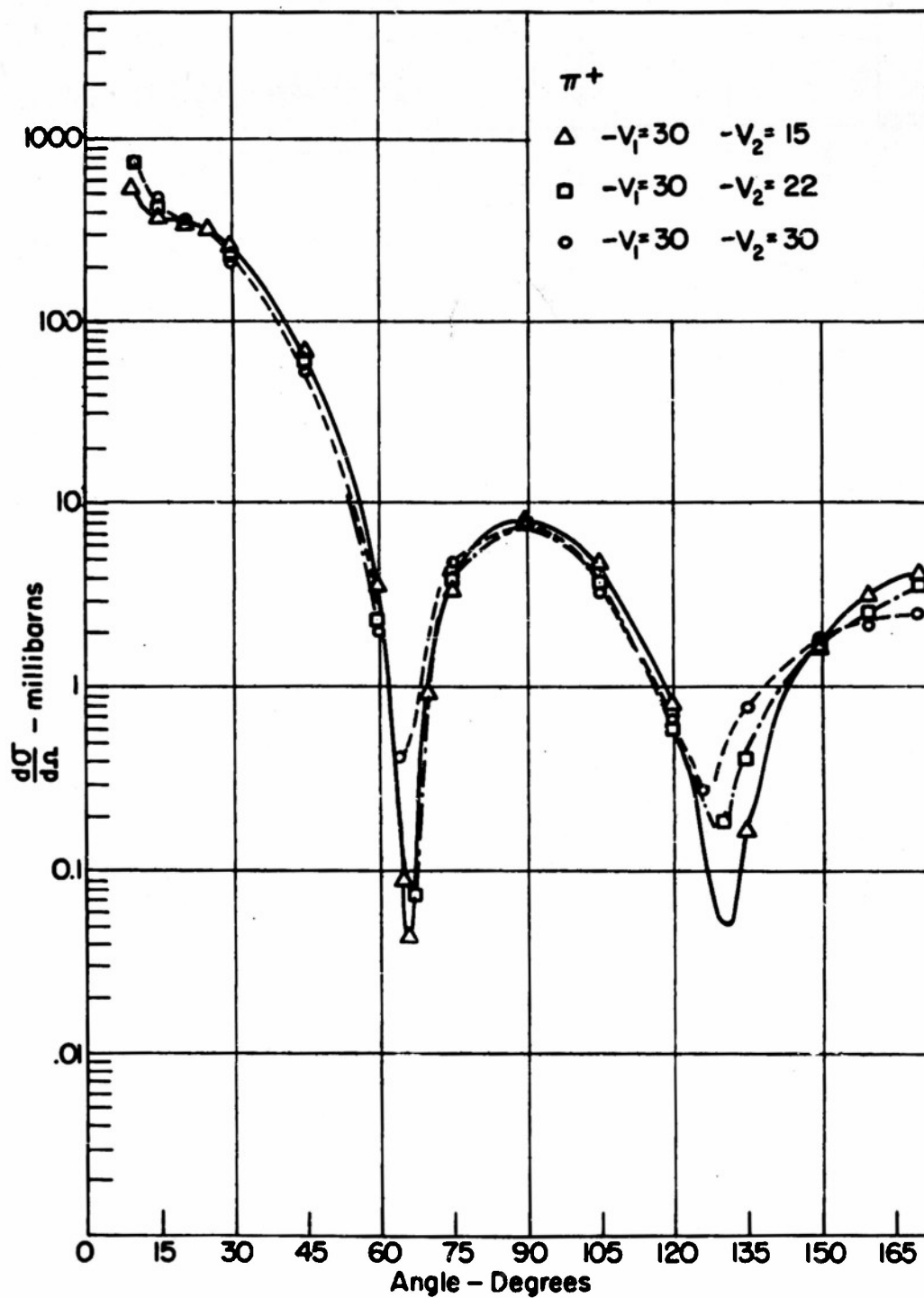


Figure 23

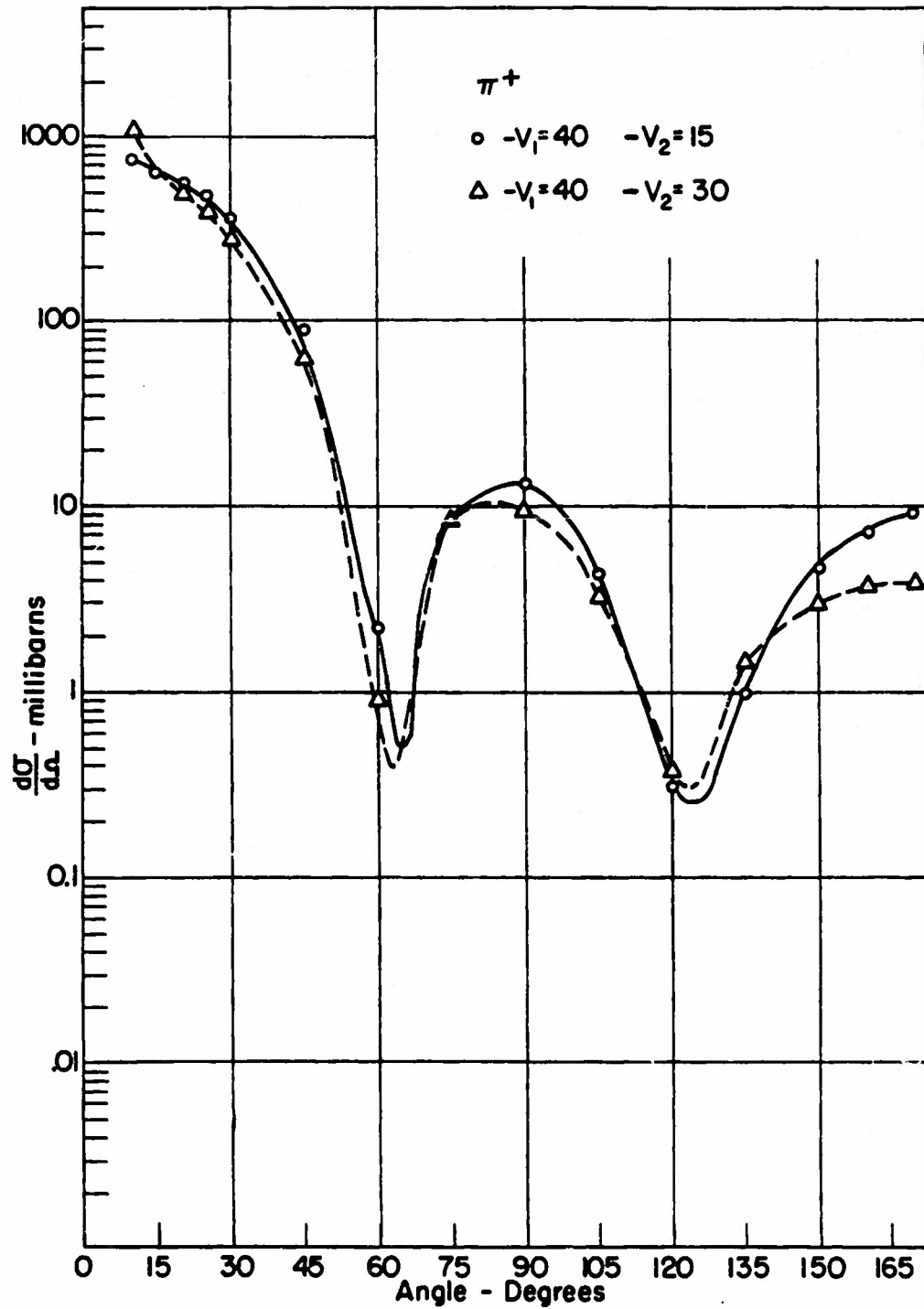


Figure 24

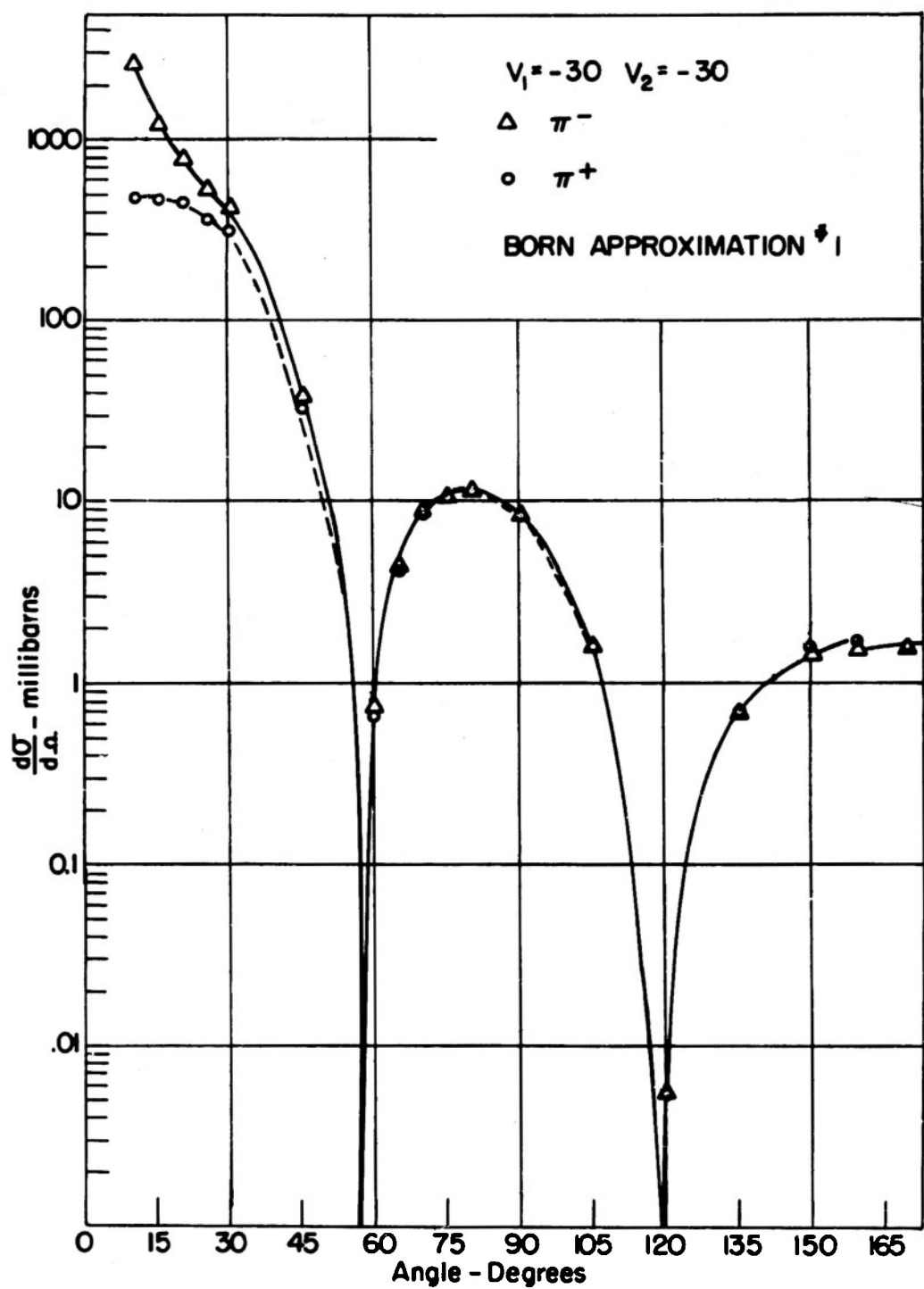


Figure 25

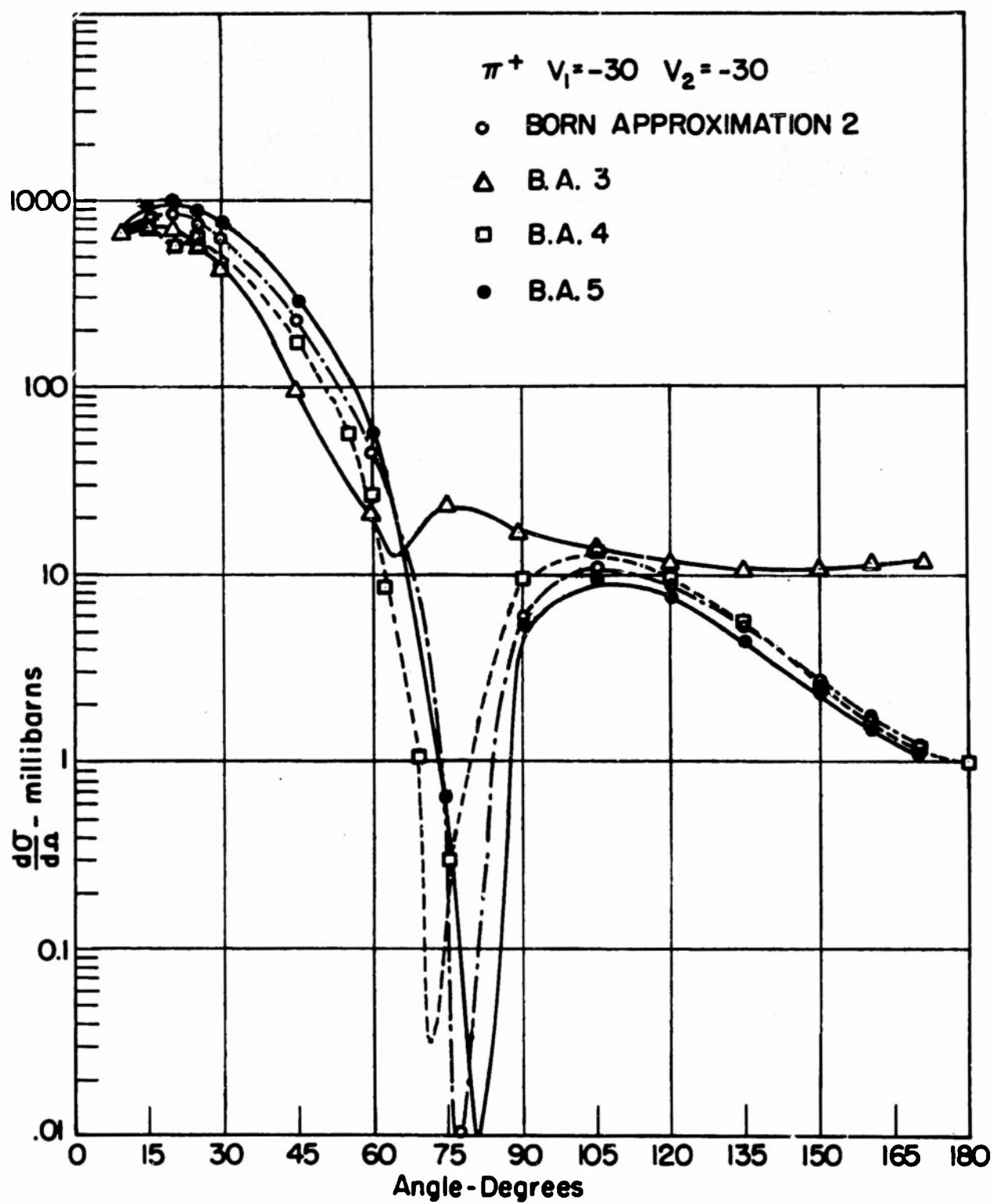


Figure 26

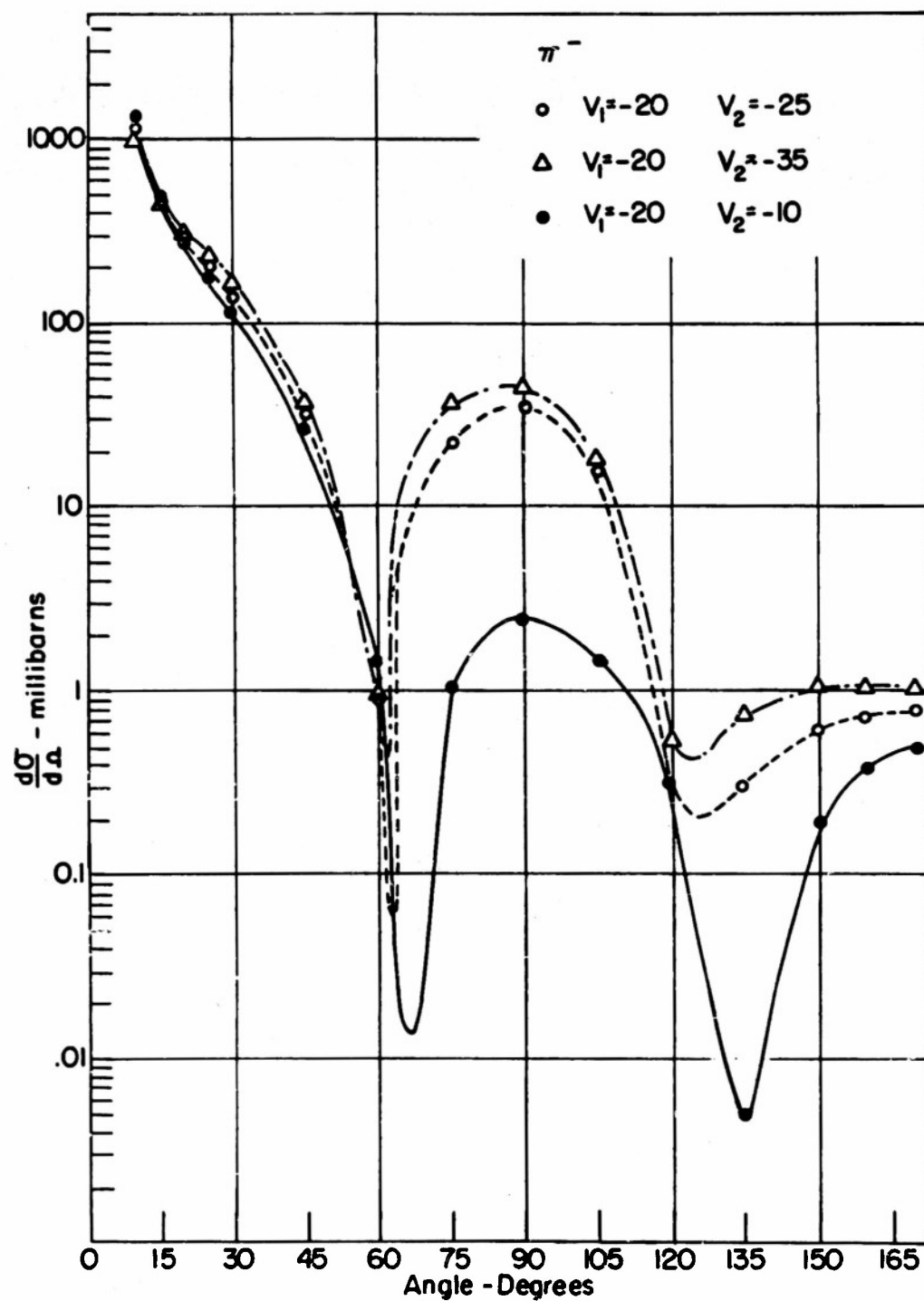


Figure 27

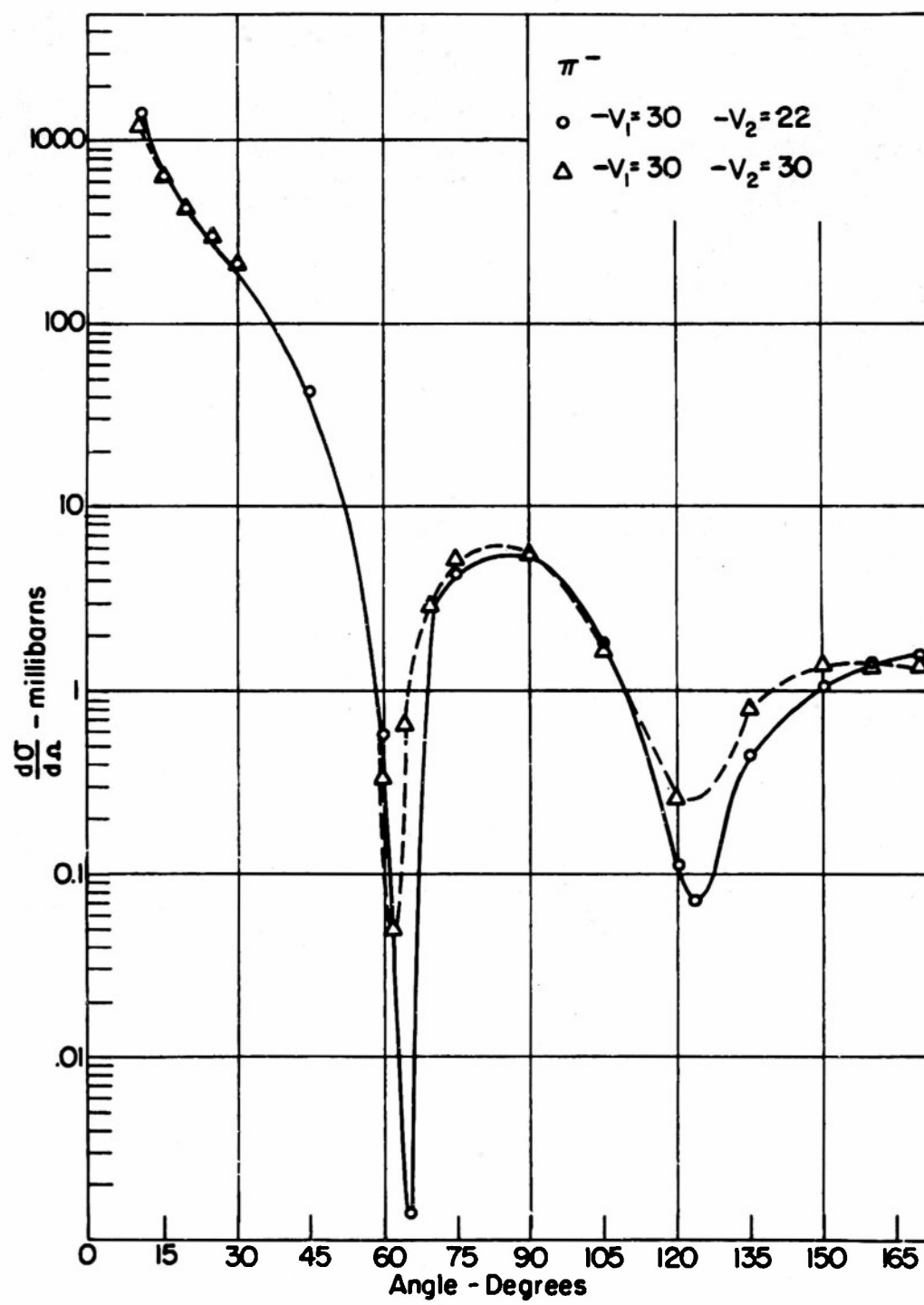


Figure 28

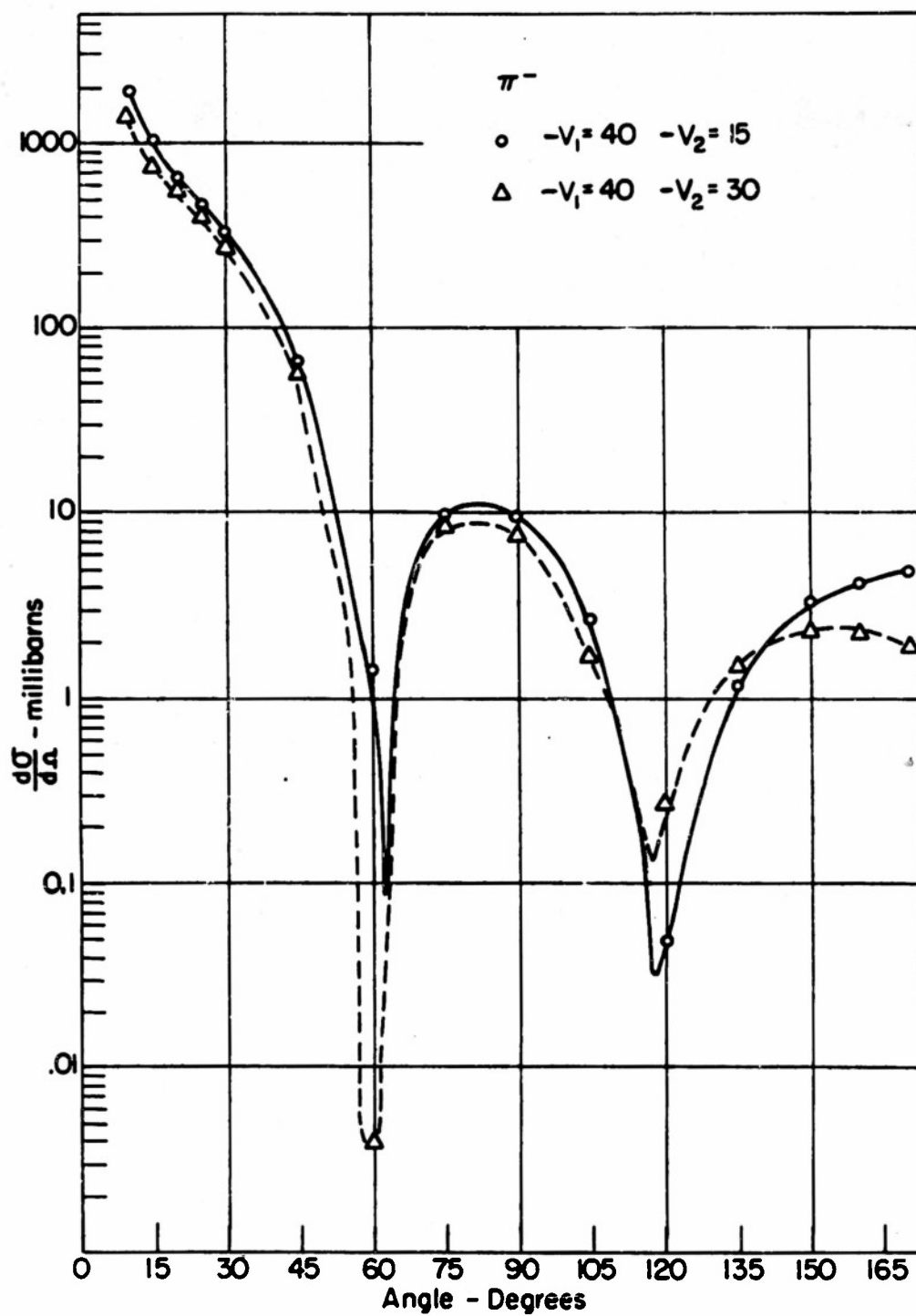


Figure 29

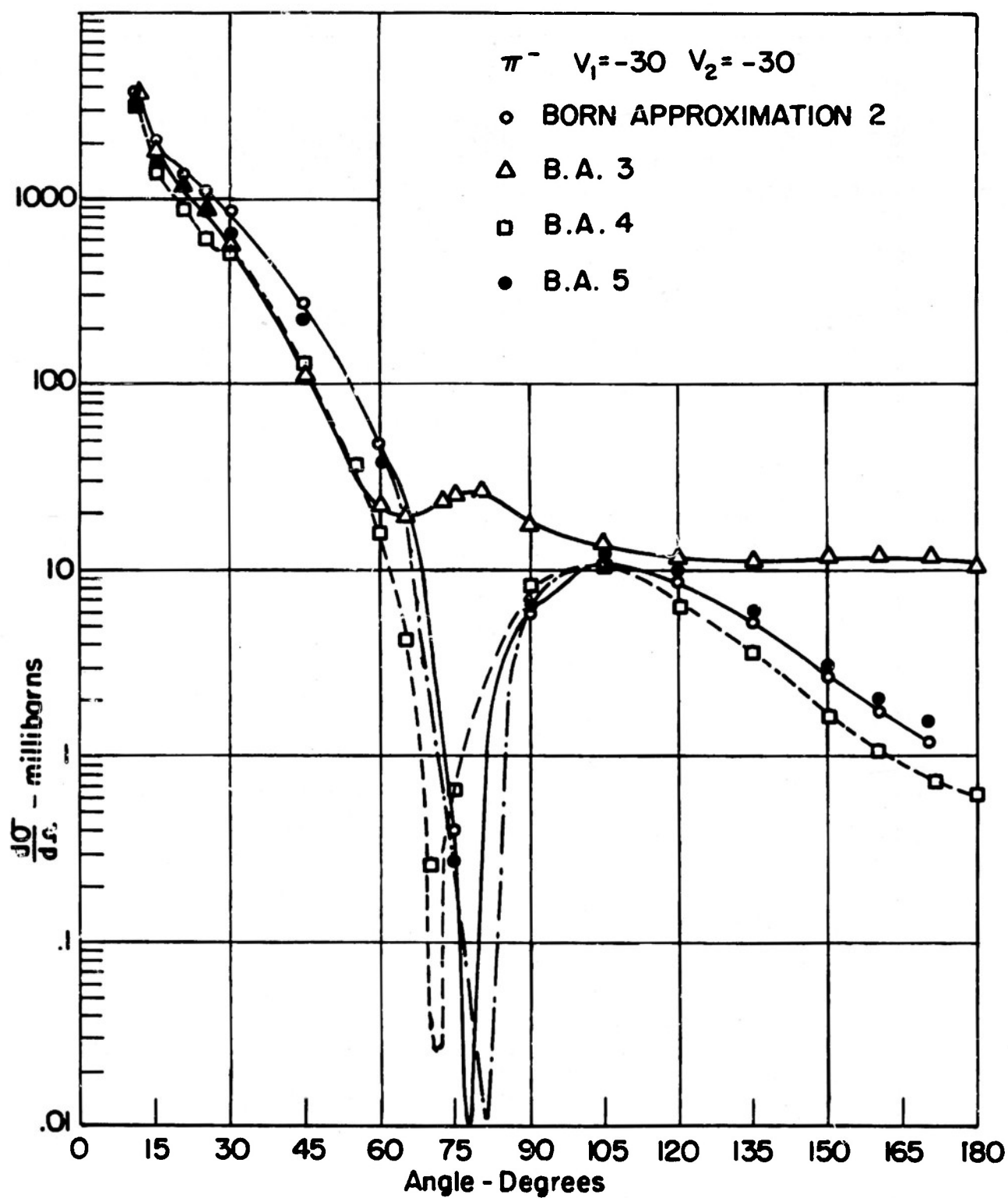


Figure 30

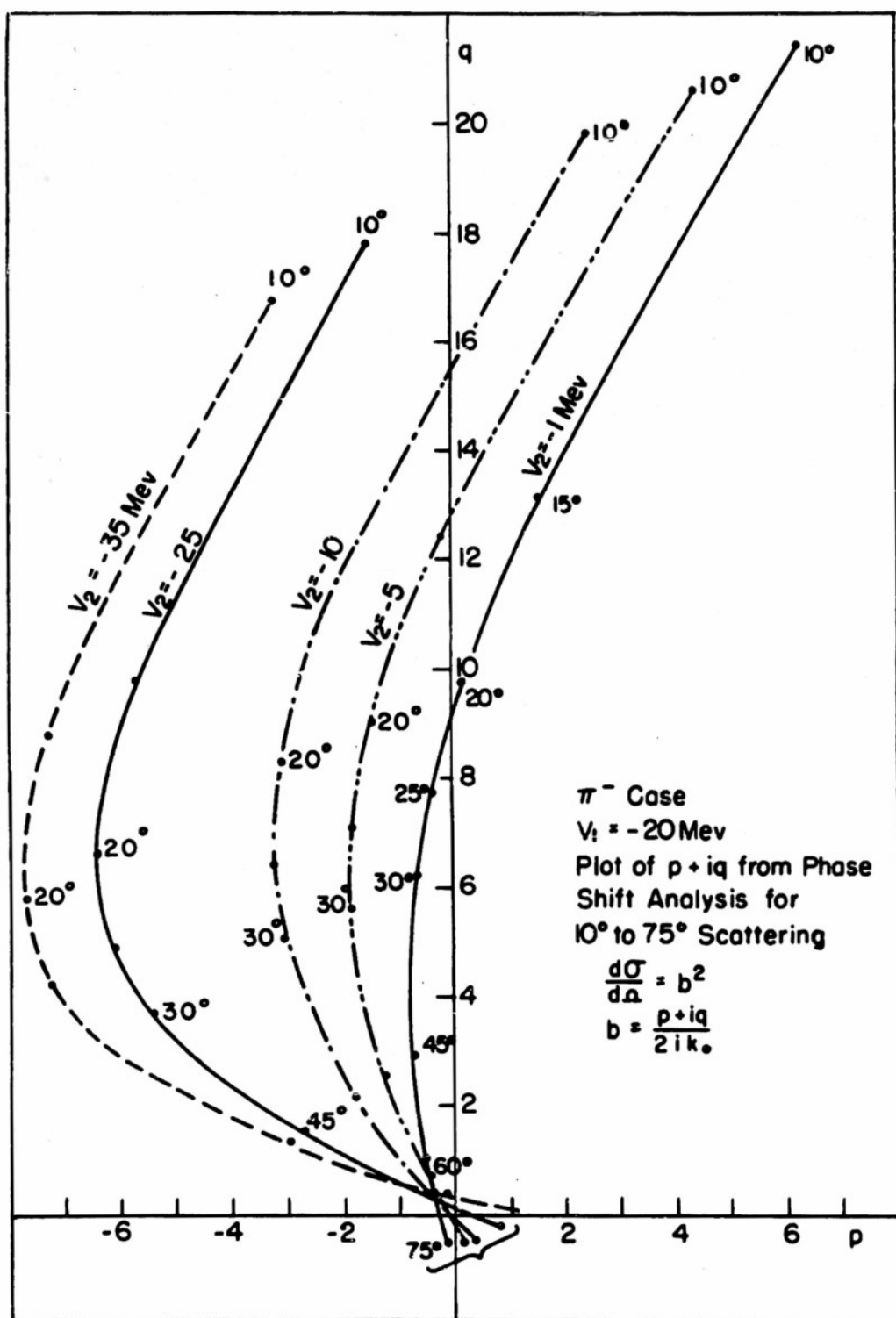


Figure 31

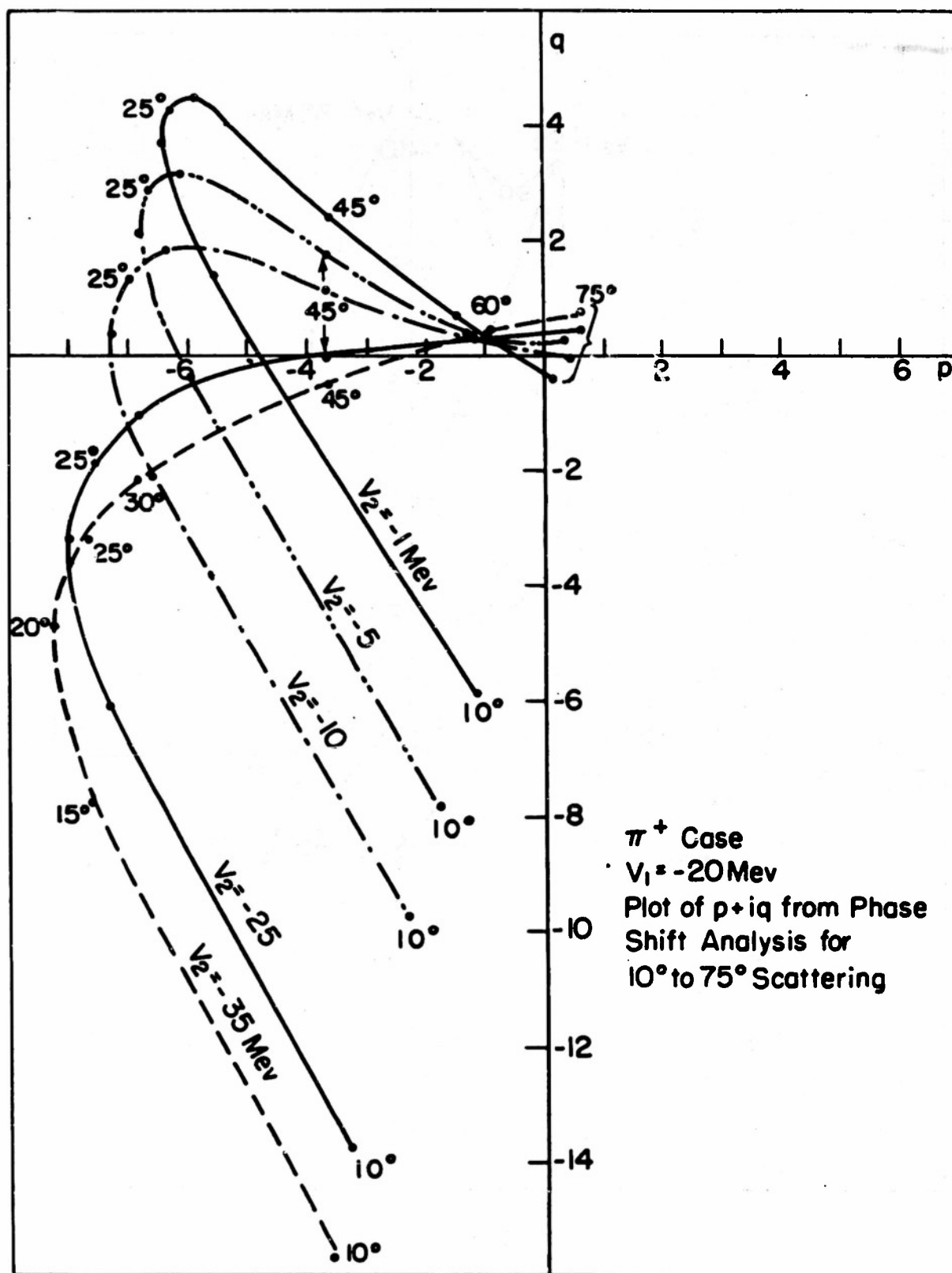


Figure 32

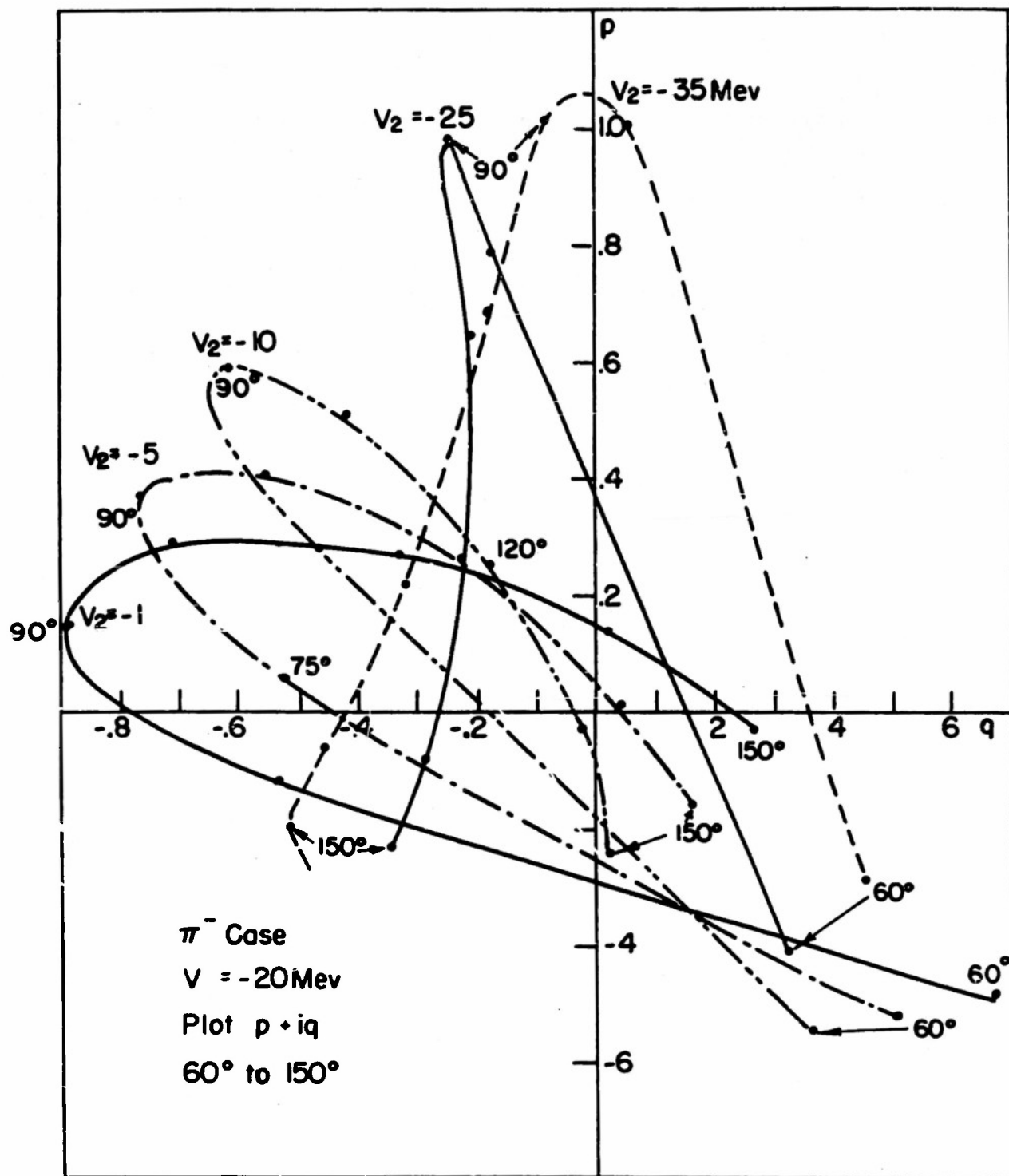


Figure 33

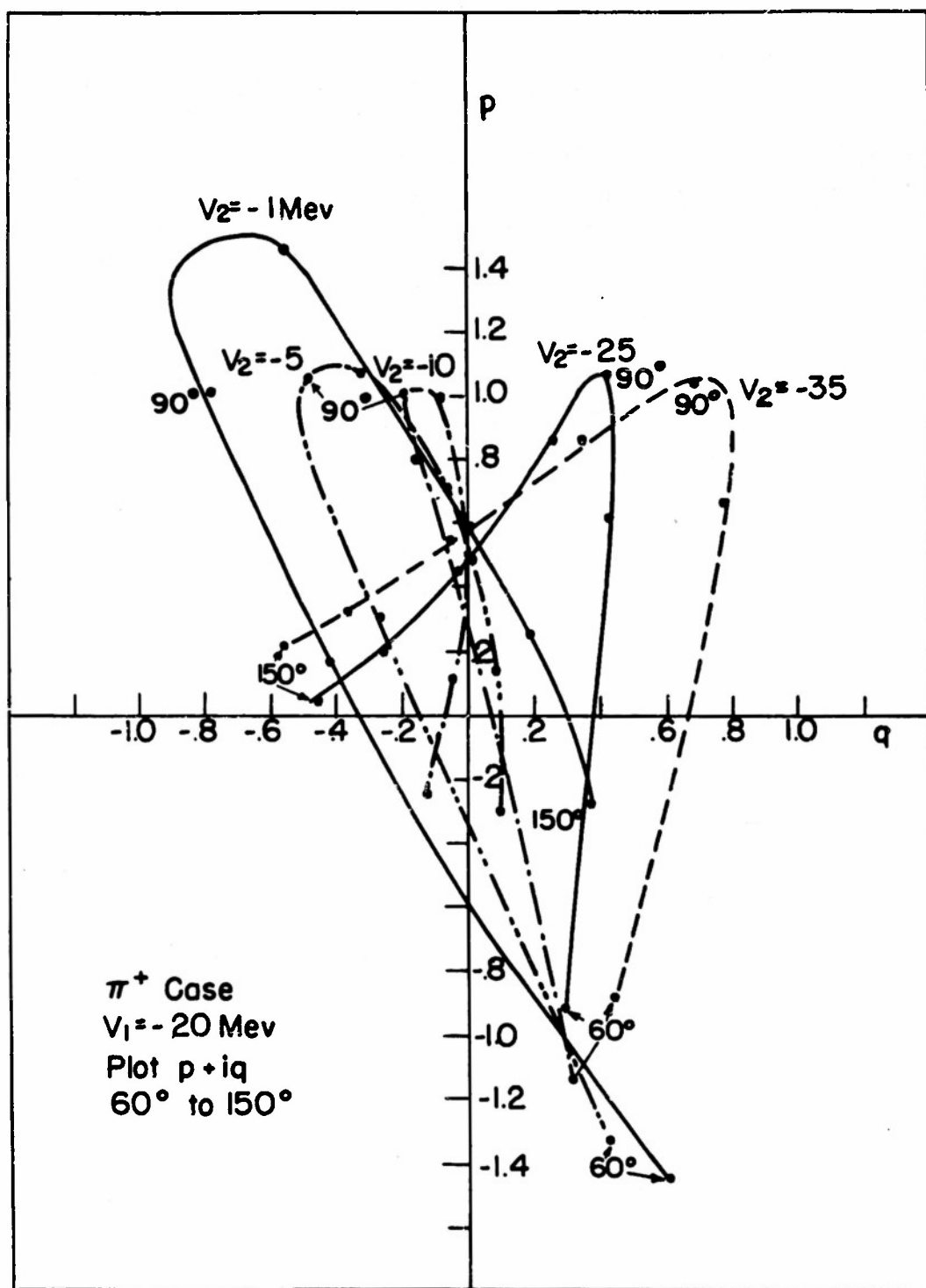


Figure 34

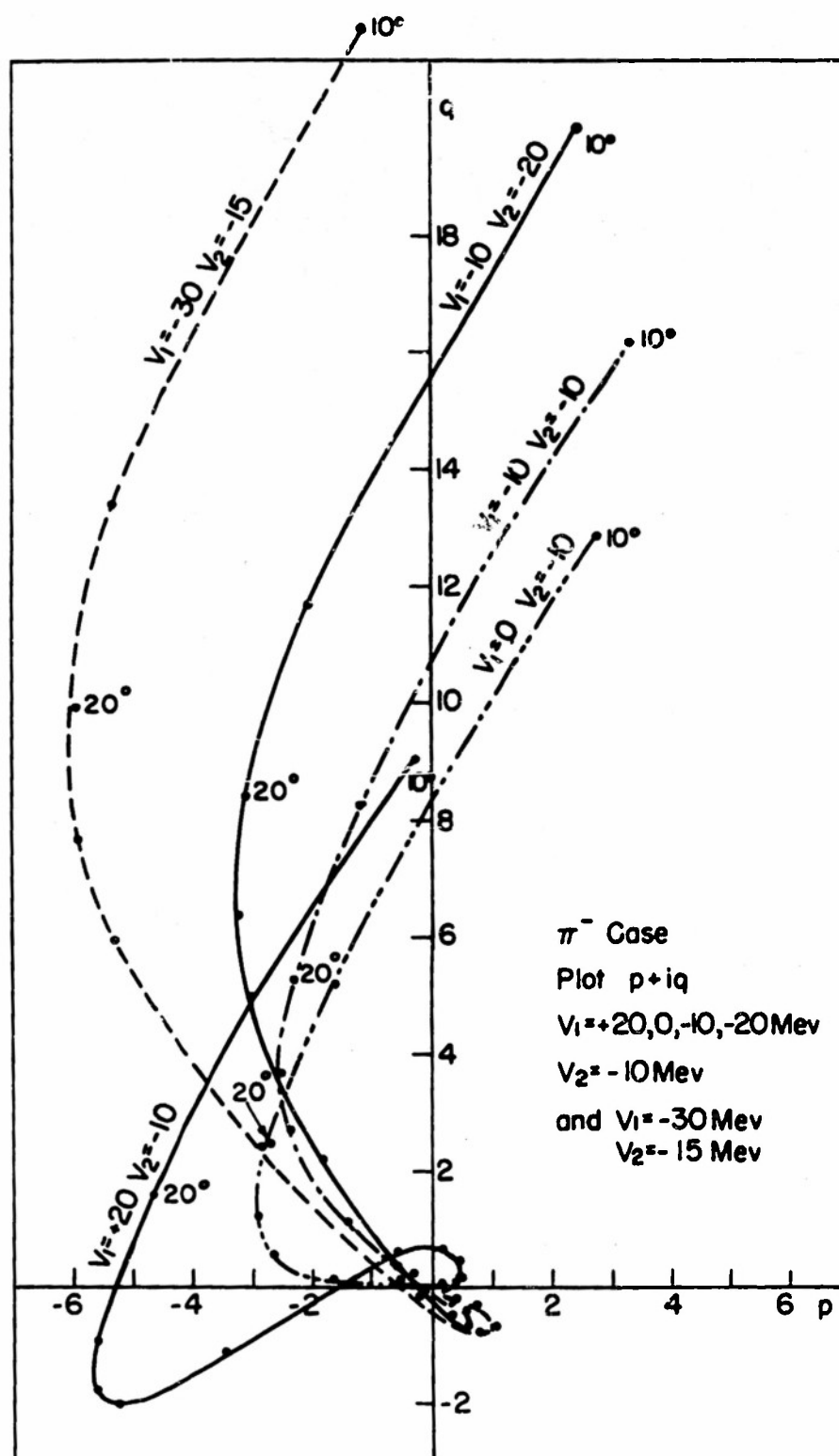


Figure 35

For comparison we also carried through a number of Born approximation type calculations, using various modifications of the usual Born approximation procedure to try to obtain a better agreement with various features of the phase shift calculation results. The various procedures are listed Born approximation 1 to 5, and are discussed below.

Born Approximation 1 (modified)

We use $f_a(\theta)$ for a point nucleus

$$f_a(\theta) = -\frac{2m}{\hbar^2} \left\{ \frac{1}{2} \frac{e^2}{q_0^2} + \frac{1}{3} R_0^2 (V_1 + iV_2) \right\} \quad (10)$$

For $f_B(\theta)$, the nuclear distribution form factor, use $q_1 = 2k_1 \sin \theta/2$ rather than $q_0 = 2k_0 \sin \theta/2$. Here k_0 and $k = k_1 + ik_2$ are the values of k at $r = \infty$, and inside the nucleus respectively. The use of k_1 rather than k_0 in $f_B(\theta)$ brings the diffraction minima to about the same angle as the phase shift calculation.

Also in f_B , we weight interior regions of the nucleus less than the surface by a factor $e^{-k_2(R_0-r)}$ to try to take account of the attenuation effects. Thus

$$f_B = \frac{3}{R_0^3} \int_0^{R_0} r^2 \left(\frac{\sin q_1 r}{q_1 r} \right) e^{-k_2(R_0-r)} dr \quad (11)$$

Born Approximation 2 (standard)

Here we use equation 10 for $f_a(\theta)$ and use the regular Born approximation also for $f_B(\theta)$. Thus, this is the true first Born Approximation.

$$f_B = \frac{3}{R_0^3} \int_0^{R_0} r^2 \left(\frac{\sin q_0 r}{q_0 r} \right) dr \quad (12)$$

Born Approximation 3 (modified)

Here use equation 10 for $f_a(\theta)$ and use $q = 2(k_1 + ik_2)$ $\sin \theta/2$ for $f_B(\theta)$, thus q is complex.

$$f_B = \frac{3}{R_0^3} \int_0^{R_0} r^2 \left(\frac{\sin q r}{q r} \right) dr \quad (13)$$

Born Approximation 4 (modified)

Here we do not separate $f(\theta)$ into a product of f_a and f_B , since the Coulomb contribution outside from the central protons is not attenuated, even if their short range force effect is attenuated.

$$(a) \quad f = f_1 + f_0 \text{ due to } r < R_0 \text{ and } r > R_0 \quad (14)$$

$$(b) \quad f_1 = -\frac{2m}{\hbar^2} \int_0^{R_0} r^2 \left(\frac{\sin q_0 r}{q_0 r} \right) (V_1 + iV_2) e^{-k_2(R_0-r)} dr$$

$$(c) \quad f_0 = -\frac{2m}{\hbar^2} \int_{R_0}^{\infty} \left(\frac{\sin q_0 r}{q_0 r} \right) \frac{Z_1 Z_2 e^2}{r} dr$$

Born Approximation 5 (modified)

Here we used the same technique as in approximation 4, but without the attenuation. This differs from the true Born approximation (number 2) in that the potential is taken as constant for $r < R_0$, while in number 2, the true inside Coulomb potential also appears. Thus this approximation matches the phase shift calculations in holding V fixed for $r < R_0$.

The results of the calculations are partly available from inspection of the Figures 25, 26 and 30. In general, the separation into $f_a f_B$ always gave a true zero at the interference minima except in approximation 3, when a complex q

was used. When the outside q_0 was used, the diffraction minima occurred at angles independent of the choice of V_1 and V_2 , while the phase shift calculations gave minima at angles that decreased as V_1 became more negative.. The angles of the minima were well matched by the Born approximation calculation using q_1 rather than q_0 for f_B .

Approximation 3 represented one attempt to obtain the proper damping of the diffraction minima. The calculations showed considerable over damping in this case. Approximation 4 and 5 also should not have true zeros, but they were much less damped than the phase shift calculations results.

Appendix Outline of the Procedure for Making the Phase Shift
Calculations

Equation 5 can be written for $r > R_0$,

$$(A-1) \quad \frac{d^2 \psi_l}{dz^2} + \left[1 - \frac{2}{Z} - \frac{l(l+1)}{Z^2} \right] \psi_l = 0$$

$$\text{For } Z = kr \text{ and } \alpha = \frac{Z_1 Z_2 e^2}{\hbar v}$$

The solutions of this equation are given by the hypergeometric function. The solution regular at $r = 0$ is denoted $F_l(\alpha, Z)$, and the irregular solution is denoted by $G_l(\alpha, Z)$. These solutions are tabulated by Breit et al.²³ (called A), and in "Tables of Coulomb Functions" published by the National Bureau of Standards²³ (called B). The functions are normalized such that they have asymptotic forms for large z .

$$(a) \quad F_l(\alpha, Z) \rightarrow \sin \left[Z - \alpha \ln 2Z - \frac{l\pi}{2} + \eta_l \right]$$

(A-2)

$$(b) \quad G_l(\alpha, Z) \rightarrow \cos \left[Z - \alpha \ln 2Z - \frac{l\pi}{2} + \eta_l \right]$$

where $\eta_l = \text{Arg } \Gamma(l + 1 + i\alpha)$.

For a pure Coulomb field (non-relativistic) only F_l can appear to satisfy the boundary condition at $r = 0$. For our problem of matching inside and outside solutions at $r = R$, we use a linear combination of F_l and G_l which leaves the incoming radial wave the same as for F_l alone. This requires that

$$(A-3) \quad \psi_l = e^{i\delta_l} [F_l \cos \delta_l + G_l \sin \delta_l], \text{ or}$$

$$\psi_l = F_l + [G_l + iF_l] e^{i\delta_l} \sin \delta_l$$

where δ_1 = additional nuclear phase shift so

$$(A-4) \quad \varphi_1 \rightarrow \sin \left[Z - \alpha \ln 2Z - \frac{\pi}{2} + \eta_1 + \delta_1 \right]$$

as $Z \rightarrow \infty$. Matching logarithmic derivatives of the inside and outside solutions at $r = R_0$ gives

$$(A-5) \quad (k_1 + ik_2) \frac{\varphi_1'(Z)}{\varphi_1(Z)}_{\text{inside}} = k_0 \frac{\varphi_1'(Z)}{\varphi_1(Z)}_{\text{outside}}$$

The inside solutions are of the form

$$(a) \quad \varphi_1(Z) = \sqrt{Z} J_{1/2}(Z), \text{ where}$$

$$(b) \quad \sqrt{Z} J_{-1/2}(Z) = \cos Z$$

(A-6)

$$(c) \quad \sqrt{Z} J_{1/2}(Z) = \sin Z \text{ and}$$

$$(d) \quad \varphi_{l+1} = \frac{(2l+1)}{Z} \varphi_l - \varphi_{l-1}$$

$$(e) \quad \varphi_l' = \varphi_{l-1} - \frac{l}{Z} \varphi_l$$

$$Z = (k_1 + ik_2) r \text{ and}$$

$$(k_1 + ik_2) R_0 = \mu + i\nu$$

The left side of equation A-5 is evaluated numerically for $l = 0$ to 5 from the above formulae. To evaluate the right side of equation A-5, we proceed as follows:

$$(A-7) \quad k_0 \frac{\varphi_1'}{\varphi_1} = k_0 \left[\frac{F_1' + (G_1' + iF_1') e^{i\delta_1} \sin \delta_1}{F_1 + (G_1 + iF_1) e^{i\delta_1} \sin \delta_1} \right]$$

Solving for δ_1 and substituting in equation 8 can be written

$$(A-8) \quad 2 \ln \zeta(\theta) = K(\theta) + iL(\theta) + \sum_l (N - iM)(2l+1) P_l(\cos \theta)$$

where K, L, N, M are real. Here K and L are the real and imaginary parts of $f_c(\theta)$, for which η_0 must be obtained.

Tables of η_0 vs. α are given in reference B (note the differences of notation as shown in Table 14.). Values of K and L for selected angles are given in Table 7. Solving for N and M reduces to evaluating F_l , F'_l , G_l , G'_l at the surface.

To evaluate F_l and G_l we follow the procedure of Reference B where

$$(a) \quad F_l = C_l(\alpha) Z^{l+1} \bar{\Phi}_l(\alpha, Z) \text{ where} \\ (A-9)$$

$$(b) \quad C_l(\alpha) = \frac{(l^2 + \alpha^2)^{1/2}}{l(2l+1)} C_{l-1}(\alpha)$$

Tables of $C_l(\alpha)$ for positive α are given in Reference B. For negative α

$$(A-10) \quad C_l(-\alpha) = e^{\pi\alpha} C_l(\alpha)$$

The functions $\bar{\Phi}_l$ are directly tabulated in Reference B. Interpolation procedures are given to obtain accurate values of $\bar{\Phi}_l$ for values of α and Z between those tabulated.

$$(A-11) \quad \bar{\Phi}_l(\alpha \pm h, Z) = \bar{\Phi}_l(\alpha, Z) \pm h [\tau \bar{\Phi}_l(\alpha, Z)] + h^2 [\tau^2 \bar{\Phi}_l(\alpha, Z)] + \dots$$

where tables of $\tau^n \bar{\Phi}_l(\alpha, Z)$ are given for $n = 1, 2, 3, \dots$

F'_l is given by

$$(a) \quad l F'_l = (l^2 + \alpha^2)^{1/2} F_{l-1} - \left(\frac{l^2}{2} + \alpha\right) F_l \\ (A-12) \quad \text{For } l \neq 0. \text{ For } l=0, \text{ we must use} \\ (b) \quad (l+1) F'_l = \left[\frac{(l+1)^2}{2} + \alpha\right] F_l - \left[(l+1)^2 + \alpha^2\right]^{1/2} F_{l+1}$$

Table 14. Comparison of Notation

Quantity	This paper	Schiff, (Ref. 22)	NBS & Breit (Ref. 23)
----------	------------	-------------------	--------------------------

kr

Z

-

 ρ

Additional
Nuclear Phase
Shift.

 δ_2 δ_1

K

$$\frac{Z_1 Z_2 e^2}{h\nu}$$

 α α η Arg $\Gamma(l+1+ia)$ η_2 η_1 σ_1

To determine G_ℓ we use the relation

$$(A-13) \quad G_\ell = \frac{\ell(\ell^2 + \alpha^2)^{-\gamma_\ell}}{F_{\ell-1}} + \frac{F_\ell G_{\ell-1}}{F_{\ell-1}}$$

This requires knowing G_1 or G_0 . It turns out to be easier to obtain G_1 from

$$(A-14) \quad G_1 = A_1 \cos \varphi_1$$

Reference A gives Tables of A_1 and φ_1 (Tables 31 and 36) in terms of α and Z .

To obtain G'_ℓ , we use the Wronskian relation to solve for G'_ℓ in terms of other quantities

$$(A-15) \quad F'_\ell G_\ell - F_\ell G'_\ell = 1$$

We are now in a position to evaluate the right side of equation A-7 in terms of $e^{i\delta_\ell} \sin \zeta_\ell$, which is required in equation 8. Actually we found it easier to solve for $e^{2i\delta_\ell}$ which is simply related to $e^{i\delta_\ell} \sin \delta_\ell$. We also require the η_ℓ values which are readily obtained from η_0 by noting that

$$\Gamma(1+\ell+i\alpha) = (\ell+i\alpha) \Gamma(\ell+i\alpha)$$

so

$$(A-16) \quad \eta_\ell = \eta_{\ell-1} + \tan^{-1}\left(\frac{\alpha}{\ell}\right)$$

Tables of N and M for selected α for our cases are given in Tables 8 and 9.

Table 15. Coherent scattering amplitudes from elementary pion nuclear interactions, as a function of angle, compared to forward scattering amplitude at 80 Mev. (80 Mev values calculated by interpolating published values. See references 15,16.)

E = 80 Mev $\pi^+ + p$	$\frac{f(45^\circ)E}{f(0)_{80}}$	$\frac{f(90^\circ)E}{f(0)_{80}}$	$\frac{f(135^\circ)E}{f(0)_{80}}$	$\frac{f(180^\circ)E}{f(0)_{80}}$
$\pi^+ + p$.55	-.55	-1.64	-2.10
$\pi^+ + p$.81	.36	-.10	-.28
$(\pi^+ + p) + (\pi^- + p)$.65	-.21	-1.06	-1.41
E = 120 Mev $\pi^+ + p$	1.13	-.71	-2.55	-3.31
$\pi^+ + p$	1.13	+.08	-.95	-1.39
$(\pi^+ + p) + (\pi^- + p)$	1.13	-.47	-1.95	-2.58

FOOTNOTES

1. Byfield, Kessler, and Lederman, Phys. Rev. 86, 17 (1952).
2. D. C. Peaslee, Phys. Rev. 87, 862 (1952)
3. Kessler and Lederman, Phys. Rev. (In press).
4. A. M. Shapiro, Phys. Rev. 84, 1063 (1951).
5. H. A. Bethe and R. R. Wilson, Phys. Rev. 83, 690 (1951).
6. J. F. Tracy, Phys. Rev. 91, 960 (1953).
7. Fowler, Fowler, Shutt, Thorndike, and Whittamore, Phys. Rev. 91, 135 (1953).
8. Isaacs, Sachs, and Steinberger, Phys. Rev. 85, 718 (1952).
9. Multiple scattering in the copper increases the energy by another Mev. See Mather and Segre, Phys. Rev. 84, 191 (1951).
10. G. Bernardini and F. Levy, Phys. Rev., 84, 610 (1951).
11. Fernbach, Serber, and Taylor, Phys. Rev. 75, 1352 (1949).
12. Hofstadter, Fechter, and McIntyre, Phys. Rev. 92, 978 (1953).
13. Schiff, Phys. Rev. 92, 988 (1953).
14. Yennie, Wilson, and Ravenhall, Phys. Rev. 92, 1325 (1953).
15. See Henley, Ruderman, and Steinberger, Annual Review of Nuclear Science #3 (1953), Table 6, p.14. See also Anderson, Fermi, Martin, and Nagle, Phys. Rev. 91, 155 (1953).
16. Bodansky, Sachs, and Steinberger, Columbia University, Nevis Cyclotron Laboratory Report No. 1.
17. Chedester, Isaacs, Sachs, and Steinberger, Phys. Rev. 82, (1951).
B. Martin, Phys. Rev. 87, 1052 (1952).
D. H. Stork, U. C. R. L. 2288 (1953).
Aarons, Ashkin, Feiner, Gorman, and Smith, Phys. Rev. 90, 342 (1953).
18. R. Hofstadter, Bull. Am. Phys. Soc., 29, No. 1, 02 (1954).
19. Pevsner, Rainwater, Williams, and Lindenbaum, Bull. Am. Phys. Soc., 29, No. 1, KA1 (1954).
Williams, Pevsner, Rainwater, and Lindenbaum, Ibid, KA3
20. Several recent papers have discussed this matter in considerable detail.
21. Fitch and Rainwater, Phys. Rev. 92, 789 (1953).
Cooper and Henley, Phys. Rev. 92, 801 (1953).
22. Schiff, Quantum Mechanics, Section 20. (McGraw Hill, New York).
23. Breit et al, Rev. Mod. Phys. 23, 147 (1951). Also, National Bureau of Standards, Applied Mathematics Series, vol. 17.
24. Pasternack and Snyder, Phys. Rev. 80, 921 (1950).

ACKNOWLEDGEMENTS

The author wishes to acknowledge with thanks the encouragement, guidance, and assistance he received from his thesis advisor, Professor James Rainwater. Further, he wishes to thank Professor Gilberto Bernardini who, while at Nevis, encouraged the author and initiated some of this work. Also the author is grateful for the invaluable help of Drs. Seymour J. Lindenbaum and Ross E. Williams throughout the course of this work. Many others of the Columbia faculty and Nevis staff have provided valuable cooperation and assistance; in particular the author wishes to thank Dr. Val Fitch for many helpful discussions and suggestions.

This research was done at the Nevis Cyclotron Laboratories, Columbia University, and was supported by the joint program of the Office of Naval Research and the Atomic Energy Commission.